# Stable Oxide p-n Heterojunctions –

## NiO-ZnO Based Transistor

Brage Otto Ormann


Thesis for the degree of
Master of Science

Department of Chemistry
Faculty of Mathematics and Natural Science
UNIVERSITY OF OSLO

03 – 08 – 2020

# Preface

*This thesis represents part of the required work for the degree of Master of Science (M.Sc.) at the Department of Chemistry, Faculty of Mathematics and Natural Sciences, University of Oslo. The work was carried out at the Group for Solid State Electrochemistry during the period from August 2018 to August 2020 under the supervision of Professor Truls E. Norby and Professor Lasse Vines.*

*First of all, I would like to thank my main supervisor Professor Truls E. Norby for his guidance, and encouragement and motivation throughout the entire process. I am also grateful to Reshma Madathil, Amir Masoud Dayaghi, and Kevin Gregor Both for their help and support. A big thanks to the whole research group for contributing to a great working environment.*

# Summary

Silicon is the most used material for p-n junctions today, and have been for as long as transistors have been around, because of the outstanding properties it possesses to construct a p-n homojunction. However, silicon p-n homojunction, and homojunction in general, will with time experience interdiffusion at the p-n interface. A possible solution to this is to utilize the great thermal stability of oxides, more accurately, semiconducting oxides that can create thermodynamically stable p-n heterojunction.

In this project, the aim is to understand the workings of a functioning transistor made form a p-n heterojunction of NiO and ZnO. NiO and ZnO are p- and n-type semiconductors, respectively. Their p- and n-type conductivity appears from their defect chemistry – $Ni_{1-x}O$ containing Ni vacancies and electron holes and $Zn_{1+x}O_{1-y}$ being inherently oxygen-deficient compensated by electrons. Dopants, such as lithium and aluminum have been proven to efficiently increase the conductivity of these materials. However, in order to create novel device functionalities in the heterostructure, one needs high-quality films and interfaces with minimal defects, hence the fabrication procedure of these materials is of great importance.

Lithium doped NiO (NiO:Li), ZnO, and aluminum-doped ZnO (ZnO:Al) in powder-form were pressed into pellets and sintered. These sintered pellets were used as target materials in pulsed laser deposition (PLD), in order to fabricate high-quality films of NiO:Li, ZnO:Al, and ZnO. PLD fabrication was a three-step process. Firstly, the bottom layer, acting as the collector, was fabricated followed by a base layer of NiO:Li. The final ZnO:Al layer is the emitter of the BJT, essentially completing the fabrication of a BJT. Alongside the manufacturing of the BJT, individual films of the materials were also fabricated.

As the structural properties of these films are of high impact on the semiconducting behavior of the materials, investigation of the crystal structure, morphology, and the interfaces follows. The individual films were characterized by XRD. For doped and un-doped ZnO, there was observed a high-intensity peak, indicating crystalline film growth strongly oriented along the (002) plane. For NiO:Li, crystalline growth with the strongly preferred direction along the (111) plane was observed. The fabricated BJT was also characterized by XRD. The diffractogram shows these are broader peaks compared to the individual layers, which indicates an increased formation of grain boundaries and defects in the crystal structure. The peak corresponding to the (111) plane of NiO:Li is found to be broad and of low-intensity, indicating low crystalline growth.

Scanning electron microscopy (SEM), was employed for further investigation of the BJT structure. The images show that there is a successful fabrication of a three-layered structure. The films look dense and without any indication of pores or cracks along the cross-section of the BJT. The surface morphology was also investigated. The first layer of ZnO showed the smoothest surface, whereas NiO:Li and ZnO:Al showed slightly more rough surfaces. Energy-dispersive X-ray spectroscopy was used to map the cross-section of the BJT. Further confirming the formation of a three-layered structure as Ni was observed with high-density in-between layers of Zn. Images captured with Transmission electron microscopy show the interface between NiO:Li and ZnO:Al. The layer thickness is found to be varying randomly in

the observed area. However, where the layers seem to have been deposited in a good manner. Here, the interface between the layers is sharp and seems to have good adhesion between them. EDX mapping confirms the elements of Zn, Ni, O, and Al in the sample.

In order to conduct electrical measurements on the constructed BJT. Unfortunately, the construction of an operating BJT had failed, as there was no transistor behavior detected. In an effort to further investigate in the cause for this, electrical measurements on the individual p-n junctions of the transistor were conducted. The emitter-base junction (ZnO:Al-NiO:Li) showed ohmic behavior, which explains the non-characteristic transistor behavior. The possibility if tunneling through the depletion zone, as it is narrow because of the dopants in NiO:Li and ZnO:Al, creating a constant current was discussed a probable cause. An increased surface area at the interface, because of an interfacial composite layer or because of the rough surface of NiO:Li, was also discussed as a suggested reason for the ohmic behavior, but no clear indications of interface defects were found. The collector-base junction, however, showed rectifying behavior, resembling that of a functioning diode. This junction showed resemblance in that of a Zener diode, which is also affected by a thin depletion layer as a result of dopants.

From the characterization method used throughout this thesis, it is evident that there has been fabricated a three-layered structure of ZnO-NiO:Li-ZnO:Al of good quality. The junctions appear quite sharp with good adhesion, however, some surface roughness and defects are found. Nevertheless, the good layering and film quality provided by the PLD method strongly suggests this method is a good candidate for obtaining the desired structural properties of the films. Small changes in the parameters of the given deposition can alter the layered material in a preferred manner.

I-V measurements of the fabricated BJT show no tendency toward transistor behavior. The electric measurements revealed that the emitter-base junction had ohmic behavior, explaining the failed transistor behavior. From XRD, SEM, TEM, and EDS, it is hard to detect a certain reason for the ohmic behavior. However, fabrication faults throughout the sample might together explain the unwanted ohmic behavior, as these defects can ruin the properties of a p-n junction. In addition, it was suggested that a high dopant concentration might effectively reduce the depletion region to a degree that would allow for tunneling of electrons across the depletion region, effectively creating the ohmic effect seen. In addition, the surface roughness of the NiO:Li layer can cause a resemblance of a composite interfacial layer, effectively decreasing the resistance across the p-n junction, hence creating an ohmic behavior.

# Contents

# 1 Introduction

In 1947, the American scientists John Bardeen, Walter Brattain, and William Shockley at the Bell laboratories built the first working transistor. This was a great scientific achievement, so great that they were rewarded the Nobel Prize in physics in the year of 1956. One can say that this invention is the building block of today's electronic society, as the transistor is an essential component in all our electronic devices, from the mobile phones in our pockets to the satellites orbiting the earth. Since 1947, the transistor has been improved and modified to fit a great span of applications, and further development and research is a never-ending process. In 1965, Gordon Moore predicted that the number of transistors in an integrated circuit would double about every two years. In Figure 1, one can see how the number of transistors in an integrated circuit has developed over the years [1]. As of today, Gordon Moore's predictions are famously called, Moore's law, as his predictions have suited the actual development.

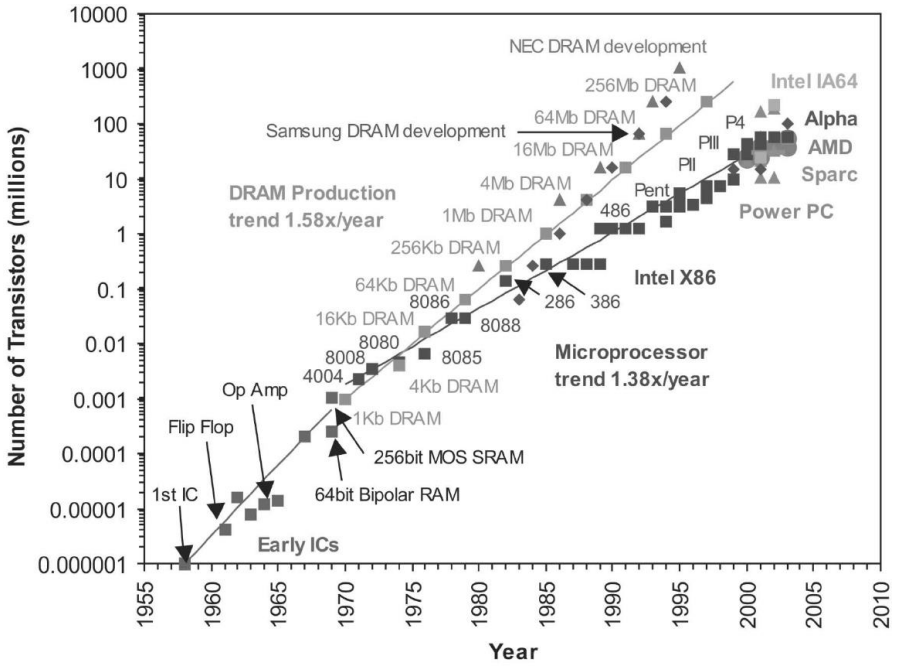


*Figure 1: Evolution of transistor count of CPU/microprocessor and memory ICs [1]*

This development is a combination of advancements in transistor miniaturization, microarchitecture, and the development of design and development tools, amongst many other elements. However, for this progress to continue, advances within all fronts of the industry must develop. Silicon, which is the most frequently used material in transistors and diodes, and have always been, is reaching its limits in some aspects of further development. The search for new semiconducting materials has, therefore become a trending research area over the last decades.

## 1.1 Coexistence in p-n junctions

Solid materials can be divided into three groups based on their energy gap or electronic conductivity; metals, semiconductors, and insulators. Metals, having large valence and conduction band overlap, possesses no band gap and have low electric resistivity. Conversely, semiconductors and insulators possess a bandgap, with insulators having a large bandgap while semiconductors possess intermediate band gaps, thus making insulators insulating, and semiconductors in a state between metals and insulators, a state that may be transformed to conducting or insulating by the introduction of dopants. The bandgap of semiconductors provides a low energetic pathway for electrons to be excited into the conduction band. By introducing small quantities of different elements, one can modulate the electrical, optical, and structural properties of the material. This process is called doping. Usually, the desired effect of doping is to increase the charge carrier concentration, either in the form of electrons or holes, commonly known as n- and p-type doping, respectively. Semiconductors, with the combination of doping, are the foundation of electronic devices, such as diodes, transistors, and solar cells. All the mentioned devices are composed of at least two semiconductors, with each side of the junction doped differently, hence making a p-n junction.

Today's p-n junctions mostly consist of homojunctions of n- and p-type doped silicon. At the interface between the n- and p-type silicon, interdiffusion will occur, as the dopants will easily make their way across the junction because these junctions are metastable. With time, and especially at higher temperatures (e.g. during overheating), the interface will turn un-sharp and eventually ruin the desired properties of the p-n-junction. However, by utilizing two different materials, which are neighbors in a phase diagram and hence in thermodynamical equilibrium, the formation of a heterojunction that is unwilling to react or interdiffuse will take place because of kinetic limitations. Without the limitation of interdiffusion, the interface will be sharp and maintain this form eternally and in high-temperature environments. p-n junctions are the foundation of transistors, which in turn is the building block of logic devices, amplifiers and most of today's electronic devices such as mobile phones and computers. By improving the p-n junctions lifetime and increasing operating temperature, electronic devices will also have an increased lifetime and be more resistant to overheating due to external heat or high currents.

## 1.2 NiO and ZnO

Among the many materials under research, semiconducting oxides are among the most widely studied materials. Within this group, transparent semiconducting oxides are of special interest, as they provide new opportunities for electronic devices. Challenges within this field lie in the understanding of their electronic structure and the physics of charge carriers, amongst other challenges such as magnetic behavior. NiO and ZnO are two transparent

semiconducting oxides that have attracted attention as possible candidates for future electronics.

NiO and ZnO both get their transparency from their large bandgap of 3.7 eV and 3.37 eV, respectively. NiO possesses a p-type conductivity because of nickel vacancies, which is compensated by its main charge carrier, electron holes. ZnO however, possesses an n-type conductivity because of oxygen vacancies and zinc interstitials being the native defects. Together, they can form a p-n junction, which is as mentioned the building block of diodes and transistors. More specifically, they will form a p-n heterojunction, in contrast to the traditional homojunction of silicon.

Structure and composition of these materials are important, as lattice defects and impurities, intentionally or unintentionally introduced, have a great impact on the electronic and structural properties of the materials. Therefore, the manufacturing process and the characterization of the materials is a key factor in understanding their behavior.

## 1.3 Approach and methodology

NiO and ZnO are well-known materials that have been investigated considerably over the years. Their wide-bandgap contributes to their ability to be transparent semiconducting materials, raising interest in using them in transparent electronic devices such as transparent window solar-cells. However, the research on p-n-junctions of NiO and ZnO creating a transistor is lacking. Transistors utilizing other materials in addition to NiO and ZnO have been investigated, but then failing to see the possibilities of a thermodynamically stable heterojunction. This project aims to investigate the properties and performance of a bipolar junction transistor, based on NiO-ZnO heterojunctions. Further, the influence of high-temperature on the performance and properties of the transistor will be investigated. If successful, the results will determine the potential applications for such a transistor. In order to successfully fabricate an operating BJT, the fabrication process is important. The fabrication will greatly affect the material properties of NiO and ZnO, as they are sensitive to structural defects and impurities. Therefore, the fabrication process and the characterization of the outcome is important in understanding the BJT behavior.

Firstly, powder batches of ZnO, aluminum-doped ZnO ($Zn_{0.98}Al_{0.02}O$), and lithium doped NiO ($Ni_{0.98}Li_{0.02}O$) will be pressed into pellets, before sintering. These pellets will be analyzed by X-Ray Diffraction (XRD). The pellets are then to be used as target materials in the manufacturing of a thin film bipolar junction transistor. The deposition of thin films will be achieved by pulsed laser deposition (PLD) upon a c-plane sapphire ($Al_2O_3$) substrate. Scanning electron microscopy (SEM) and transmission electron microscopy (TEM) will provide information on the composition and interface of the deposited p-n junctions, while XRD will provide the crystal structure of the layers. I-V output characteristics of the manufactured BJT will be

measured using simple circuits connected to power sources and multimeters, at different temperatures. Also, conductivity/resistivity measurements of single layers of ZnO, NiO:Li and ZnO:Al will be conducted using a van der Pauw 4-point measurement, in order to confirm semiconducting behavior of the individual films.

# 2 Theory

This chapter introduces the theory and concepts for the research in this thesis. Firstly, an introduction to semiconductors, the concept of doping them, and their bandgap are presented. Hereafter, a review of the defect chemistry of ZnO and NiO is given. Then the p-n-junction is discussed in detail before transitioning on to diodes. Lastly, the workings of a bipolar junction transistor are presented.

## 2.1 Semiconductors

Materials exhibit a wide range of electrical conductivities and can be classified after their ability to conduct electricity. On the highly conducting side are *metals*, with typical conductivity in the order of $10^{7}$ $(\Omega m)^{-1}$, some examples are copper, gold, and aluminum. On the other side of the spectrum, with conductivities in the range of $10^{-10}$ to $10^{-20}$ $(\Omega m)^{-1}$, we have *insulators*, such as plastics and ceramics. Finally, in the middle, we have *semiconductors* with an intermediate conductivity of $10^{-6}$ to $10^{4}$ $(\Omega m)^{-1}$, with silicon being the most used semiconductor as of today. This difference in conductivity is directly connected to the bandgap of the materials, therefore one can also classify metals, semiconductors, and insulators by their bandgap. From Figure 2, one can see that the bandgap goes from non-existing in metals to an intermediate bandgap in semiconductors, and finally, a large bandgap for insulators. The bandgap is equal to the energy required for a valence electron to be excited to the conduction band, where the electron is free to move. Therefore, an increase in the bandgap will decrease electric conductivity, as there will be a lesser concentration of free electrons to create a current.

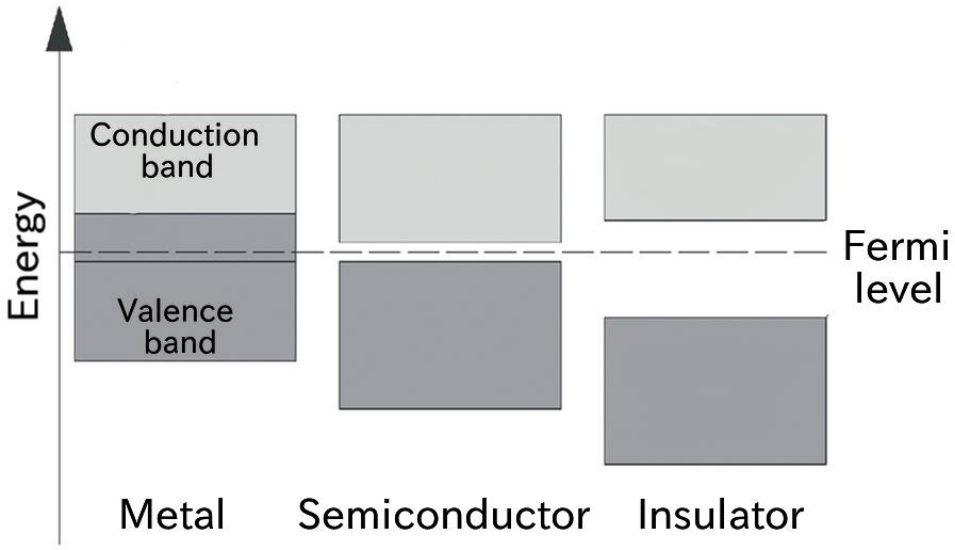


*Figure 2: Metals have overlapping between the conduction band and the valence band. Semiconductors have an intermediate bandgap, with a filled valence band and empty valence band. The insulator has a big bandgap, making it energetically difficult for electrons to transfer to the conduction band.*

Further, a solid can be placed into one of three broad classifications by their atomic arrangement, that is; amorphous, polycrystalline, and crystalline. A crystalline solid consists of periodic and repeated three-dimensional arrangement throughout the specimen. Like the crystalline solid, polycrystalline solids have a periodic and repeated three-dimensional arrangement, however, polycrystalline solids don't have the long-range continuity, but an assembly of many crystalline grains disoriented relative to each other. Finally, when there is no long-range systematic arrangement of atoms represented in the solid, they are determined amorphous. For a semiconductor material to operate at their highest potential, they should be comprised of a high degree of crystallinity and have management over defects and impurities.

### 2.1.1 Doping

By deliberately introducing impurity dopants to the semiconductors lattice, the electric conductivity can be drastically altered, towards metallic or insulating behavior. Impurity concentrations as low as one atom per $10^{12}$ are used to alter semiconductor properties. Dopants are normally introduced to increase the conductivity by introducing excess electrons or holes. When doped with excess electrons, making them the majority charge carrier, the semiconductor is denoted as n-type, whereas if electron holes are the majority charge carrier, the semiconductor is denoted as p-type.

Silicon, having four valence electrons with each of them bonded with one of four adjacent silicon atoms, can be doped to form a P- or N-type semiconductor, depending on the dopant introduced. By doping silicon with atoms from group 15 of the periodic table, such as phosphorus which has five valence electrons, one effectively introduces one free electron as there are only four possible bounds to neighboring silicon atoms. This free electron is loosely bonded to the impurity atom by electrostatic forces, and the energy state of this electron lies in the bandgap, just beneath the conduction band. Introducing enough impurity atoms of phosphorus to the silicon lattice will make electrons the majority charge carrier, hence creating an N-type semiconductor. A simple illustration of phosphorus doping in silicon is shown on the left of Figure 3.

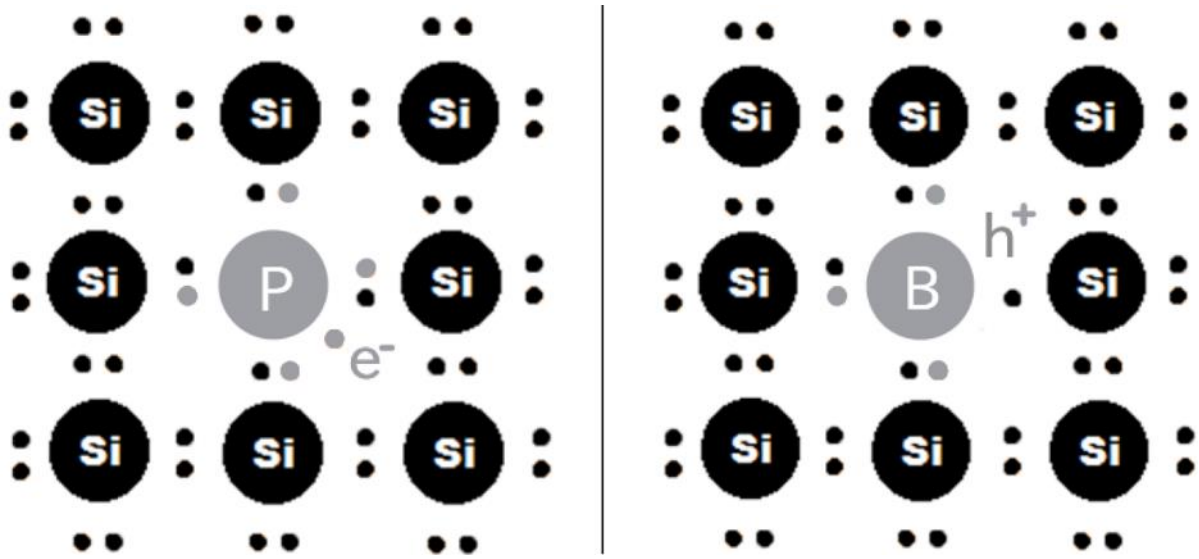


*Figure 3: Left side shows donor doping of phosphorus in silicon, creating n-type conductivity in the silicon. The right side shows the acceptor doping of Boron into Silicon, creating p-type conductivity in the silicon.*

By introducing impurity elements from group 13 of the periodic table to the silicon lattice, a P-type semiconductor can be achieved. Elements from this group, such as boron, have three valence electrons, effectively introducing an electron-hole to the silicon lattice as one of the four bounds is now deficient. This impurity atom, with a lower valence, also introduces an energy level within the bandgap, however, this energy level is now located just above the valence band. The atoms creating n- and p-type semiconductors are determined as donors and acceptors, respectively.

Semiconductors intermediate state of conductivity, along with the sensitivity of altering their electrical conductance with impurity atoms has over the years made them a fundamental necessity in modern information technology. As research continues, new semiconductors proposing new and interesting properties are being found and investigated, such as oxide-based semiconductors. New materials bring new application possibilities and can further improve and develop today's use of semiconductors.

### 2.1.2 Heterojunction band alignment

Most p-n junctions today are an assembly of the same material, with each side of the junction doped differently, and called a homojunction. However, one can also have a junction of two different semiconducting materials, one p-type and one n-type, forming a heterojunction. The basic principles behind a heterojunction are also true for a heterojunction. ZnO and NiO will form a heterojunction, therefore the further focus on heterojunctions.

When combining two different semiconductors, their Fermi levels usually differ, thus multiple band alignments are possible. When two semiconductors form a heterojunction, there are three possible band alignments, commonly called; straddling gap (type I), staggered gap (type II) and broken gap (type III), all shown in Figure 4. In the straddling gap alignment, type I, one of the semiconductors have valence- and conduction-band at energy levels in-between that of the other semiconductor. For the staggered gap alignment, type II, the conduction band and valence band of the two semiconductors are aligned in an alternating manner. For the broken gap alignment, type III, neither the valence- nor conduction-band of the two semiconductors overlap, creating a gap between them. For both type I and type II, there are two possible alignments as the Fermi levels of the two semiconductors can differ with respect to each other.

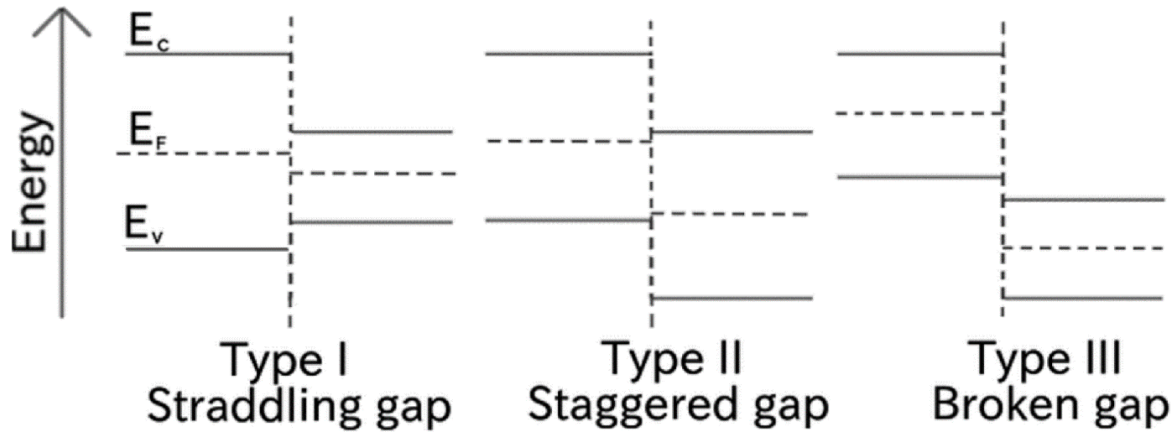


*Figure 4: Simple schematics of the three types of heterojunction band alignments before equilibrating the Fermi energy.*

**Type I**

For type I-1, the Fermi level for the first semiconductor is higher than for the second semiconductor. To align the Fermi levels during junction formation, free electrons will flow from the first semiconductor into the second semiconductor. Therefore, the second semiconductor surface is negatively charged while the first semiconductor is positively charged, creating an internal electric field moving from the first, towards the second semiconductor. When the Fermi levels are aligned, the direction of the internal electric field indicates that electron holes will move from the first semiconductor to the second, and vice versa for the electrons. However, since the conduction band of semiconductor one is more negative than for the second semiconductor, the transfer of electrons over the junction is hindered, causing an accumulation of electrons on the interface of the second semiconductor, while holes can move effortlessly over the junction.

In type I-2, the Fermi level is lower for the first semiconductor, compared with the second semiconductor, creating a reversed situation compared to the former. As the internal electric field is aligned from the second semiconductor towards the first, and the conduction band of the second semiconductor is less negative than the conduction band in the first semiconductor, electrons can now diffuse from the first semiconductor to the second, while electrons holes accumulate at the interface.

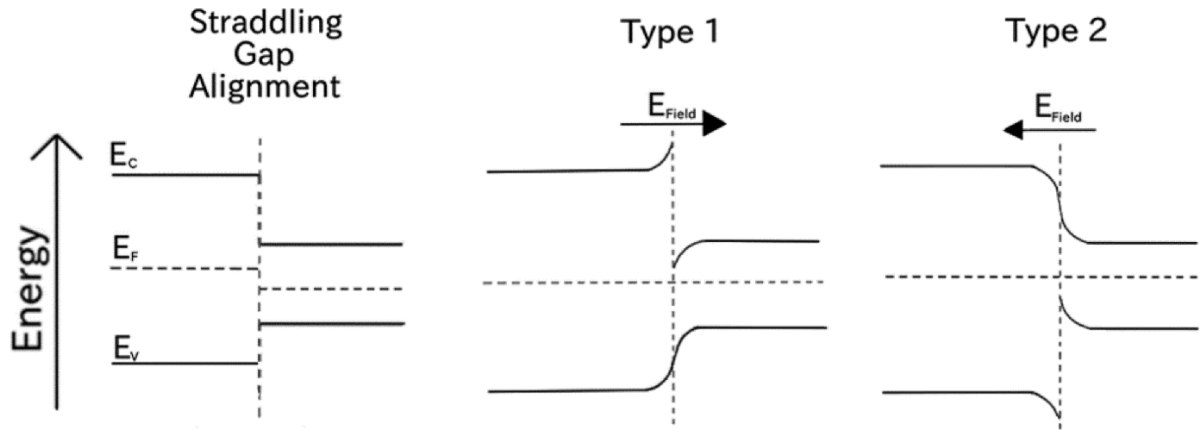


*Figure 5: To the left is a schematic of a straddling gap alignment for type I-1 before equilibrium, where the fermi-level of the left side is higher than for the material on the right side. If the left side semiconductor has a lower Fermi-level than the material at the right side, then there is a type I-2 alignment. The figure in the middle and the figure to the right show, respectively, type I-1 and type I-2 alignment after equilibrium.*

**Type II**

In the case of a staggered gap alignment, type II, the conduction band and valence band are arranged in an alternating manner. In the case where the first semiconductor possesses a higher Fermi level than the second semiconductor, type II-1, the internal electric field will have the same direction as type I-1 alignment. However, the flow of charge carriers is different in this case. Electrons generated in the first semiconductor will flow opposite to the electric field, away from the interface, while electron holes will move towards the interface. The movement of the free charge carriers of the second semiconductor will be the opposite. Consequently, electron holes from the first semiconductor and electrons from the second semiconductor will recombine at the interface.

In the case where the Fermi level of the second semiconductor is higher than the first semiconductor, type II-2, the internal electric field is oriented in the opposite way of type II-1. In this scenario, the conduction band of semiconductor two is less negative than that of semiconductor one, resulting in a flow of electrons across the interface, from semiconductor on towards the second, similar to the movement of electrons in type I-2 band alignment.

However, in opposition to the type I-2 band alignment, electrons holes will in this situation also diffuse across the junction, in the direction of the electric field.

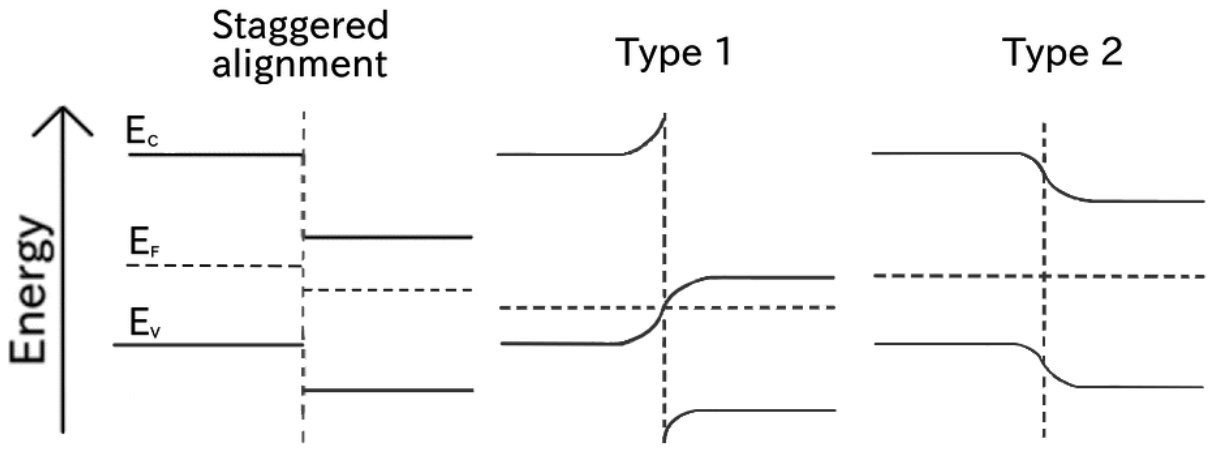


*Figure 6: To the left is a schematic of a staggered gap alignment for type II-1 before equilibrium, where the fermi-level of the left side material is higher than for the material on the right side. If the left side semiconductor has a lower fermi-level than the material at the right side, then there is a type II-2 alignment. The figure in the middle and the figure to the right shows type II-1 and type II-2 alignment after equilibrium, respectively.*

**Type III**

As for the broken gap band alignment, type III, there will not be any diffusion of charge carriers across the interface as the conduction band of the first semiconductor overlaps the valence band of the other semiconductor.

## 2.2 Defect chemistry

Defects play a big role in p-n junctions as they are key to understanding the electric conductivity in the n- and p-type regions. Because of the predominant cation deficiency in $Ni_{1-x}O$ compensated by electron holes, and oxygen deficiency in $ZnO_{1-y}$ compensated by electrons, they have p- and n-type character, respectively. By introducing acceptors and donors, these characters are enhanced, and this can be explained through defect reactions using the Kröger-Vink notation system.

### 2.2.1 NiO

The native defects in NiO are the cation deficiency compensated by electron holes, thus, the dominant free charge carrier is electron holes. The formation of these defects can be explained through:

$$½O_2(g) = v''_{Ni} + O_O^x + 2h^* \quad (1)$$

where $v''_{Ni}$ represents a doubly negatively charged vacancy on a nickel site, $O_O^x$ represents oxygen on an oxygen site, and $h^{\cdot}$ represents electron holes. From this reaction, it is evident that the formation of nickel vacancies and electron holes will increase with partial pressure $pO_2$. The law of mass action leads to the equilibrium constant, $k_1$

$$k_1 = \frac{[v''_{Ni}]p^2}{p_{O_2}^{\frac{1}{2}}} \quad (2)$$

With $p$ and $p_{O_2}$representing the electron-hole concentration and oxygen partial pressure, respectively.

NiO in its pure stoichiometric form is not a great electric conductor, however, by introducing acceptor dopants into the lattice the charge carrier concentration can increase, which will increase the electric conductivity. One candidate as an acceptor dopant is the lower valent lithium ions, $Li^+$, to replace nickel at nickel sites. The formation of a defect can be explained through

$$Li_2O + ½O_2(g) = 2Li'_{Ni} + 2h^* + 2O_O^x \quad (3)$$

Equation 3 shows the formation of electron holes, and as for pure stoichiometric NiO, the formation of electron holes will increase with partial pressure $pO_2$. The electroneutrality can be expressed as

$$2[v''_{Ni}] + [Li'_{Ni}] = p \quad (4)$$

By assuming that the concentration of acceptor defect is constant and predominated the metal vacancy, one can find the $p_{O_2}$ and temperature dependency of the fully ionized metal vacancy with the help of eq. 2, which results in

$$[v_O^{**}] = \frac{k'_{v_O^{**}}(p_{O_2})^{-\frac{1}{2}}}{n^2} = k^0_{v_O^{**}} exp\left(-\frac{\Delta H^0_{v_O^{**}}}{RT}\right)\frac{(p_{O_2})^{-\frac{1}{2}}}{n^2} \quad (5)$$

Here $\Delta H^0_{v_O^{**}}$ is the nickel vacancy defect formation standard enthalpy.

### 2.2.2 ZnO

The native defects in ZnO are oxygen vacancies, these are compensated by electrons which then are the main charge carriers in ZnO. Electrons may also form as compensation to zinc interstitials, the two reactions are as follows, respectively.

$$O_O^x = v_O^{**} + \tfrac{1}{2}O_2(g) + 2e' \quad (6)$$

$$Zn_{Zn}^x + O_O^x = Zn_i^{**} + \tfrac{1}{2}O_2(g) + 2e' \quad (7)$$

where $Zn_{Zn}^x$ represents zinc at a zinc site, $O_O^x$ represents oxygen at an oxygen site, $Zn_i^{**}$ represents a doubly positively charged zinc interstitial, and $e'$ represents a free electron. The law of mass action leads to the two equilibrium constants, $k_1$ and $k_2$, as

$$k_1 = [v_o^{**}]n^2 p_{O_2}^{\frac{1}{2}} \quad (8)$$

$$k_2 = [Zn_i^{**}]n^2 p_{O_2}^{\frac{1}{2}} \quad (9)$$

, with $n$ representing the electron concentration.

Contrary to NiO, ZnO is a relatively good electric conductor in its pure form. However, as for NiO, by introducing dopants to the ZnO lattice, one can increase the charge carrier concentration, thus increase the electric conductivity. As the intrinsic charge carrier concentration in ZnO is electrons, donor dopants are needed to increase the charge carrier concentration. One dopant possibility is higher valent aluminum ions, $Al^{3+}$, replacing zinc at zinc sites in the lattice.

$$Al_2O_3 = 2Al_{Zn}^* + 2O_O^x + \tfrac{1}{2}O_2 + 2e' \quad (10)$$

The electroneutrality can be expressed as

$$2[v_O^{**}] + [Al_{Zn}^*] = n \quad (11)$$

By assuming that the concentration of donor defect is constant and predominated the fully ionized oxygen vacancy, one can find the $p_{O_2}$ and temperature dependency of the fully ionized oxygen vacancy with

$$[v_O^{**}] = \frac{k'_{v_O^{**}}(p_{O_2})^{-\frac{1}{2}}}{n^2} = k^0_{v_O^{**}} exp\left(-\frac{\Delta H^0_{v_O^{**}}}{RT}\right)\frac{(p_{O_2})^{-\frac{1}{2}}}{n^2} \quad (12)$$

### 2.2.3 Electrical conductivity

When a charged particle species, $i$, with the charge $z_i e$, of a material, is exposed to an electric field, $E$, they will be affected by a force proportional to the electric field and the concentration, $c_i$. This will give rise to a partial current density $i_i$,

$$i_i = \sigma_i E = z_i e c_i u_i E \quad (13)$$

where $\sigma_i$ and $u_i$ represent the partial electric conductivity and charge mobility, respectively, of the defects. The total electrical conductivity is given as the sum of the partial conductivities of the charge carriers,

$$\sigma_{tot} = \sum_i \sigma_i \quad (14)$$

These partial conductivities is usually included cations, anions, electrons, and electron holes. However, there is usually one charge carrier that dominates the charge transport. The mobility of these partial conductivities differs, with electrons and electron holes possessing much higher mobility than that of cations and anions.

The electronic conductivity is related to the motion of mobile electrons and electron holes through the material. The contributions to electronic conductivity from electrons or holes are known as *n*- and *p*-type conductivity, respectively. The total electronic conductivity may be expressed in terms of the concentration of the electronic charge carriers, electrons *n* and holes *p* with their corresponding charge mobilities $u_n$ and $u_p$:

$$\sigma_{el} = \sigma_n + \sigma_p = enu_n + epu_p \quad (15)$$

where n and p represent electron and hole concentration, respectively. $u_n$ and $u_p$ represent the electron and hole charge mobility, respectively, and e is the elemental charge.

As electrons or electron holes move through polar compounds, they polarize the neighboring lattice and cause local deformation of the structure (such an electron or electron-hole is termed a polaron). A weak interaction between the electronic defects and the lattice is termed a large polaron and acts much like free electronic carriers. However, for most transition metal oxide semiconductors there is strong electron-phonon coupling, and the electronic defects move by means of small polaron mechanism. At lower temperatures, small polarons may tunnel between localized sites. However, at higher temperatures (> 500 C) the energy levels of the electrons and electron holes are localized on specific atoms, and the electronic defects contribute to the electrical conduction through thermally hoping from a specific crystal site to another. Therefore the mobility of a small polaron can be expressed through,

$$\mu_{n,p}(T) = \frac{\mu_0}{T} \exp\left(-\frac{E_a}{k_B T}\right) \tag{16}$$

where $E_a$ is the activation energy for the hoping, $k_B$ is the Boltzmann constant and T is the temperature.

Diffusion theory can be applied to species that follow an activated hopping mechanism, i.e. ionic conduction, in order to understand the conductivity of a species. The charge carrier mobility and electrical conductivity are related to diffusion and follow the Nernst-Einstein relationship,

$$D_i = u_i \frac{k_B T}{z_i e} = \sigma_i \frac{k_B T}{c_i (z_i e)^2} \tag{17}$$

where $D_i$ is the self-diffusion coefficient, $k_B$ is the Boltzmann constant, T is the absolute temperature in Kelvin.

The self-diffusion coefficient is partially given by its hopping frequency, and this hopping frequency is proportional to the Boltzmann distribution factor, thus the charge carrier mobility, and therefore also the conductivity has Arrhenius types of temperature dependencies,

$$u_i = \frac{u_0}{T} exp \frac{-\Delta H_{mob}}{RT} \tag{18}$$

$$\sigma_i = \frac{\sigma_0}{T} exp \frac{-\Delta H_a}{kT} \quad (19)$$

, $\Delta H_{mob}$ is the charge carriers enthalpy of mobility and $\Delta H_a$ is the activation energy for conduction. $\sigma_0$ is a pre-exponential containing several factors to the diffusing species and the structure it is diffusing through.

When a metal is exposed to a higher temperature, lattice vibrations increases. This effectively reduces the mean free path of the electrons, hence decreasing their mobility and consequently reducing the conductivity with the increase of temperature. However, this is not the case for semiconductors. As the temperature rises, electrons in the valence band will gain energy, and some will gain enough energy to be excited to the conduction band and act as free electrons, hence increasing the charge carrier concentration and consequently increasing the conductivity.

## 2.3 Fick`s laws

Diffusion is the movement of a species from higher concentration towards lower concentration and occurs in gasses, liquids, and solids. In solids, the driving force of diffusion is thermally activated random motion of atoms. However, for a particle or atom to move within the lattice, there must be a defect present to make room for the movement. This causes different types of diffusion mechanisms in solids, such as vacancy and interstitial diffusion. In addition, 1- and 2- dimensional defects such as dislocations and grain boundaries can also contribute to diffusion.

As mentioned, diffusion is the movement of a species from higher concentration towards lower concentration, and Fick's first law relates the diffusive flux to the gradient of the concentration.

$$j = -D \frac{dc}{dx} \quad (20)$$

, here, *j* is the particle flux density, D is the diffusion coefficient, *dc*/*dx* is the concertation gradient in the x-direction. The minus sign indicates that the diffusion flow is in the direction of high to low concentration. Diffusion in most solids is an isotropic process. However, in anisotropic materials, the diffusion process depends on the specific direction. The equation is applicable for isotropic materials, but can in general be used as an approximation for anisotropic materials.

For most diffusion situations, the concentration gradient and flux will vary with time. Hence, because Fick's first law assumes a fixed concentration gradient across the plane where the

flux of particles occurs, this law is not applicable for nonsteady-state situations. That is, when the concentration gradient and diffusion flux will vary through the solid, Fick's first law is not convenient and replaced with Fick's second law

$$\frac{\partial c}{\partial t} = D\frac{\partial^2 c}{\partial x^2} \tag{21}$$

, here, $\partial c/\partial t$ represents the rate of change of concentration in a certain area. As two materials are in contact, such as in a p-n junction, there is initially an abrupt line between the two sides. However, as explained, particles or atoms will move towards the lesser concentration, which in the case of a p-n junction will be across the junction. This process, of which atoms of one material diffuse into another, is called interdiffusion. In a p-n junction, interdiffusion will cause problems, as it can change the intended properties of the junction.

## 2.4 p-n junction

A p-n junction is an interface between two semiconductors, with one of the two possessing n-type conductivity, whereas the other possesses p-type conductivity, forming a single system. Majority carrier holes from the p-type region and majority carrier electrons from the n-type region diffuse across the junction. The diffusion of majority charge carriers leaves behind negatively charged acceptor atoms in the p-type region and positively charged donor atoms in the n-type region, thus inducing an electric field in the direction of n- to p-side. All free charge carriers are now depleted in an area around the junction leaving no free charge carriers to carry current, hence the name *depletion region* for this area. The diffusion process continues until thermal equilibrium is achieved. Thermal equilibrium is achieved when the induced electric field force is equal to the oppositely directed force of the diffusion, the two forces cancel each other. When thermal equilibrium is achieved, the Fermi level is constant through the system. As a consequence of the Fermi level being aligned throughout the system, a band bending of the energy bands through the depletion zone occurs, creating the unique properties of a p-n junction.

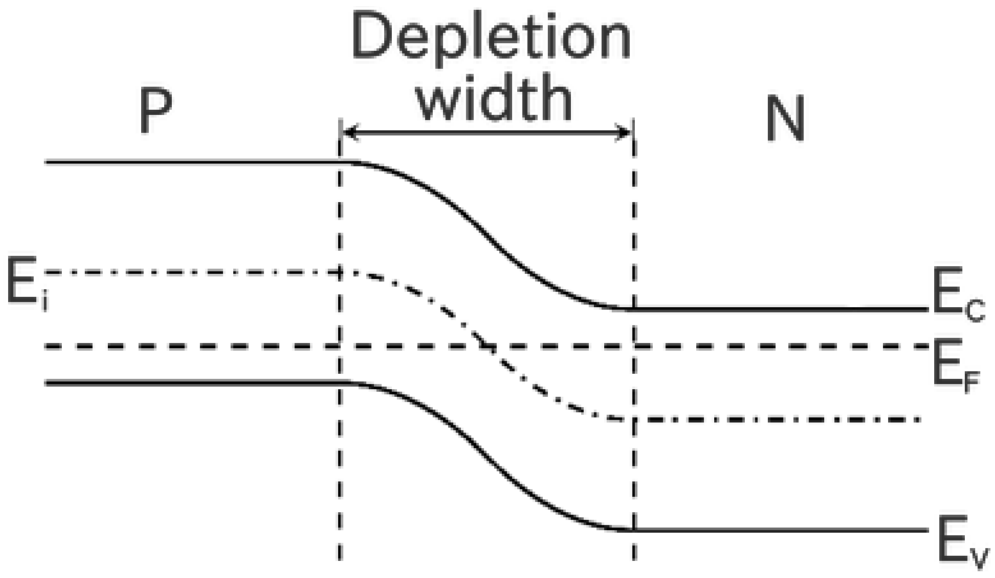


*Figure 7: Band bending occurs when assembling a p-type and n-type semiconductor, resulting in diffusion and drift of electrons and holes until equilibrium is achieved (when the fermi-levels align as shown).*

### 2.4.1 Biasing

In a p-n junction, the depletion region can either be enforced or reduced, by the appliance of external electrical potential. With the junction being forward biased, the depletion region is reduced and current can more easily cross the junction. With reverse biasing, the depletion region is increased, thus making it difficult for the current to flow through the junction. Hence, the p-n junction only possesses a single direction of possible current flow. With no applied bias and the p-n junction in equilibrium, and the Fermi level is constant through the system as shown in Figure 8 of the energy-band diagram of the p-n junction in thermal equilibrium. The electric field in the depletion region creates an electrostatic potential over the junction, called the built-in potential $V_{Bi}$. The built-in potential is equal to the difference in Fermi energy for the P and N side of the junction

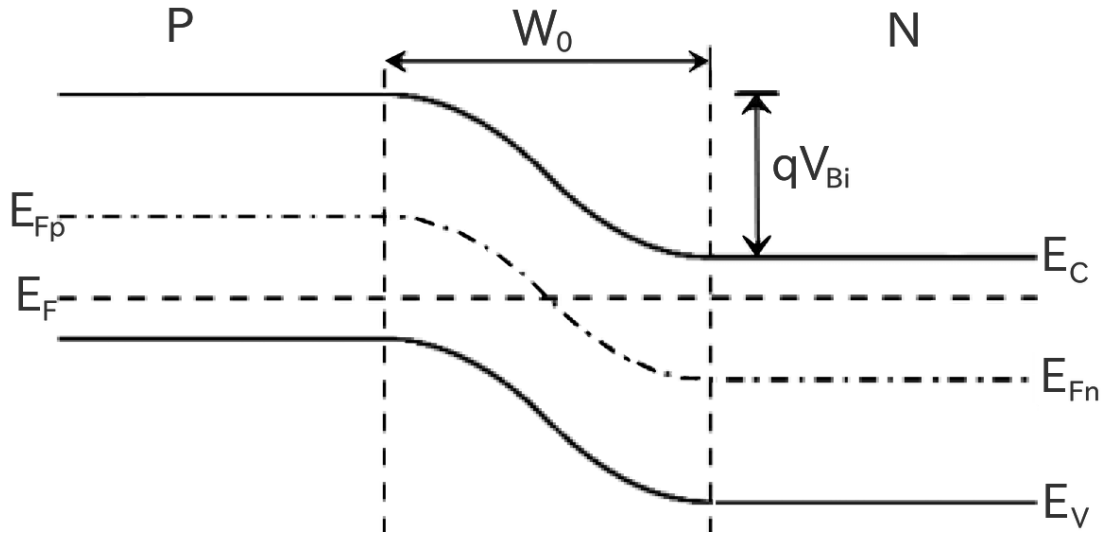


*Figure 8: p-n junction in thermal equilibrium, $E_{Fp}$ and $E_{Fn}$ is the intrinsic Fermi level of the materials on p- and n-side, respectivlely. $qV_{Bi}$* represents the built in potential, and $W_0$ is the depletion zone when no bias is applied.

In Figure 9 the p-n junction is in reverse bias, meaning there is applied potential between the n and p regions with a negative terminal to the p-region and positive terminal to the n-region. The mobile charge carriers will move away from the junction and towards the oppositely charged terminals, creating an increase in the electrostatic potential across the depletion region, resulting in an increase of the depletion region. As an external voltage is applied, equilibrium is no longer achieved, as the Fermi levels are not the same on the p-side and n-side. From equation 10, one can confirm the increase in depletion width by the applied reverse biasing. The built-in potential will be increased from $qV_{Bi}$ to $q(V_{Bi} + V_f)$.

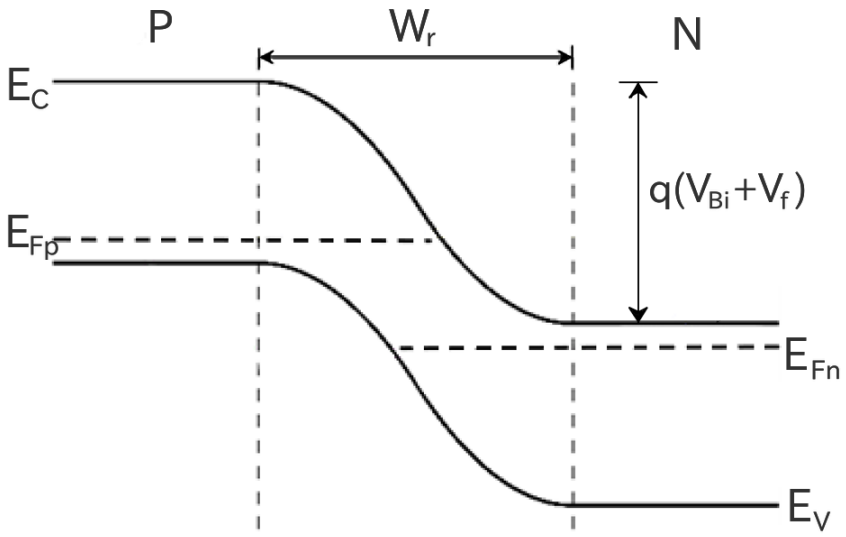


*Figure 9: Reverse biasing of the p-n junction. In the case of reverse biasing, the electrostatic potential across the depletion region is increased, effectively creating a bigger barrier for charge carrier diffusion across the depletion region.*

In the opposite case, where a positive terminal is connected to the p-side, and a negative terminal is connected to the n-side, there is forward bias. By forward biasing the p-n junction, a decrease in the depletion region is observed. Also here, the constant fermi level through the system is broken when there is an applied voltage. Opposite to the reverse bias, the applied external bias, V, will reduce the built-in potential from $qV_{bi}$to $q(V_{bi} - V_f)$. Correspondingly, the total band bending will also get reduced, resulting in an easier charge carrier diffusion across the junction, shown in Figure 10.

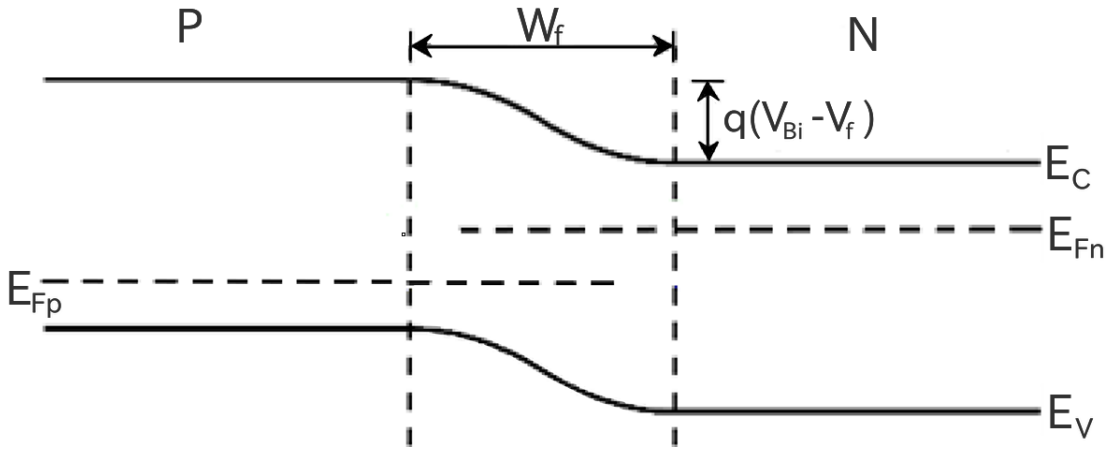


*Figure 10: p-n junction in forward bias. A forward bias will effectively reduce the depletion region, reducing the barrier for charge carrier diffusion across the depletion zone.*

### 2.4.2 Depletion width

In an effort to understand semiconductor electronics such as diodes and transistors, the depletion region is a key factor. The width of the depletion region can be calculated using approximations commonly known as the depletion approximation. The approximation defines the depletion region as drained of all free carriers and assumes an abrupt transition between this region and the neutral region, this assumption is justified by considering that the transition occurs within a small region compared to the depletion region width.

Using Poisson`s equation and the depletion approximation, the depletion width can be calculated. Starting with Poisson's equation that relates the second derivative of the electric potential to the charge density

$$\frac{d^2V}{dx^2} = \frac{dE}{dx} = \frac{p}{\varepsilon} = \frac{q}{\varepsilon}\left[p - n + N_D^+ - N_A^-\right] \tag{22}$$

, where V is the electric potential, $p$ is the charge density, ε is the dielectric constant, q is the charge of the carrier, p and n represents hole and electron concentration, respectively, and $N_D^+$and $N_A^-$ represents the ionized donor and acceptor concentrations, respectively. In this equation, the charge density is a function of the electron density, hole density, and acceptor and donor density.

Utilizing the depletion approximation, which states that the majority carrier concentration within well-defined edges of the depletion region is completely depleted, we approximate $p$ and $n$ to equal zero. Furthermore, with the assumption that all acceptors and donors are ionized, they are replaced with acceptor and donor concentrations, respectively.

$$p = qN_D\,, \quad for \quad 0 < x < x_n \tag{23}$$

$$p = -qN_a\,, \quad for \quad -x_p < x < 0 \tag{23}$$

, here, $x_n$ and $x_p$ is the depletion layer width in the n- and p-type regions, respectively.

Gauss`s law, $\nabla * (\varepsilon \boldsymbol{E}) = \rho$ gives

$$\frac{d}{dx}E(x) = \frac{qN_D}{\varepsilon_n}\,, \qquad for \quad 0 < x < x_n \tag{24}$$

$$\frac{d}{dx}E(x) = -\frac{qN_A}{\varepsilon_p}\,, \qquad for \quad -x_p < x < 0 \tag{24}$$

, where $\varepsilon_n$ and $\varepsilon_p$ are the permittivity in the n and p regions, respectively. Gauss law states that the electric field is given by the charge density over the permittivity, thus giving the electric field as a linear function for the two regions

$$E(x) = \frac{qN_D(x - x_n)}{\varepsilon_n}, \qquad for \;\; 0 < x < x_n \tag{25}$$

$$E(x) = -\frac{qN_A(x + x_p)}{\varepsilon_p}, \qquad for \;\; -x_p < x < 0 \tag{25}$$

Integrating equation 25 one can find the potential distribution across the depletion region

$$V_n = \left(\frac{qN_D}{2\varepsilon_n}\right) x_n^2 \tag{26}$$

$$V_p = \left(\frac{qN_A}{2\varepsilon_p}\right) x_p^2 \tag{26}$$

, with the built-in potential, $V_{Bi}$, being defined as $V_{Bi} = V_n + V_p$ , we get

$$V_{Bi} = V_n + V_p = \left(\frac{qN_D}{2\varepsilon_n}\right) x_n^2 + \left(\frac{qN_A}{2\varepsilon_p}\right) x_p^2 \tag{27}$$

Combining equation 27 with the charge neutrality equation that states $N_A x_p = N_D x_n$, we get the depletion widths of the $p$ and $n$ region

$$x_p = \left[\frac{2\varepsilon_n \varepsilon_p N_D V_{Bi}}{qN_A(\varepsilon_n N_A + \varepsilon_p N_A)}\right]^{\frac{1}{2}} \tag{28}$$

$$x_n = \left[\frac{2\varepsilon_n \varepsilon_p N_A V_{Bi}}{qN_D(\varepsilon_n N_A + \varepsilon_p N_A)}\right]^{\frac{1}{2}} \tag{28}$$

The total depletion width is given by adding the two

$$W = x_n + x_p = \left[\frac{2\varepsilon_n \varepsilon_p (N_A + N_D)^2 V_{Bi}}{qN_D N_A(\varepsilon_n N_A + \varepsilon_p N_A)}\right]^{\frac{1}{2}} \tag{29}$$

, where the width is an approximation of an unbiased p-n junction. When calculating the width with an applied bias, one simply has to replace the built-in voltage term, $V_{Bi}$, with $V_{Bi} - V$, where V is the applied bias

$$W = x_n + x_p = \left[\frac{2\varepsilon_n\varepsilon_p\,(N_A + N_D)^2\,(V_{Bi} - V)}{qN_DN_A\left(\varepsilon_nN_A + \varepsilon_pN_A\right)}\right]^{\frac{1}{2}} \tag{30}$$

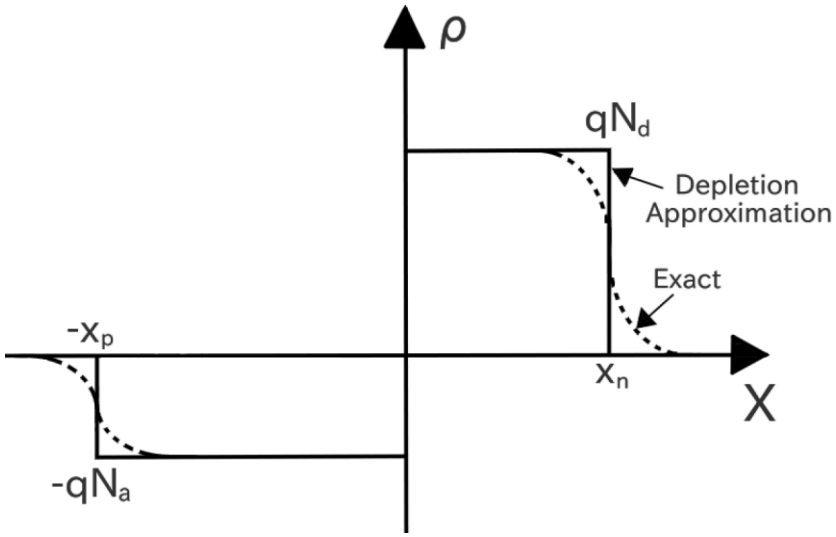


*Figure 11: Schematic representation of the charge density in a p-n junction, with the depletion approximation shown with a solid line, and the dotted line representing the real value.*

## 2.5 Bipolar junction transistor

The transistor is a semiconductor device that can regulate the flow of current, or voltage, and act as an amplifier or switch. Today's electronic devices rely heavily on transistors, as it's fundamental in the construction of modern-day electronics. There is a wide variety of transistors with different properties depending on the application use, mainly divided into bipolar junction transistors (BJT) and field-effect transistors (FET), where the later has overtaken the BJT as the most frequently applied transistor today. For this research, the simplicity and robustness of the BJT will be utilized to construct a NiO-ZnO transistor. Therefore, the theory of BJT ensues.

The bipolar junction transistor (BJT) is a three-terminal device consisting of two back to back p-n junctions, resulting in two possible combinations of either pnp or npn. The npn BJT is the most frequently used of the two, because of the higher mobility of electrons compared to holes. The three terminals are labeled emitter, base, and collector, with the base being the middle semiconductor squeezed between the emitter and collector, as illustrated in Figure 12. The emitter emits minority carriers into the base, and the collector collects the minority carriers that cross over the base, hence their names. The three regions are differently doped, with the emitter being heavily doped, base intermediately doped and the collector lightly doped. The emitter is highly doped so a large number of charge carriers can "flood" the base, which has a lower doping concentration to reduce recombination. The principle of the BJT is to control big output signals with the help of a small input signal.

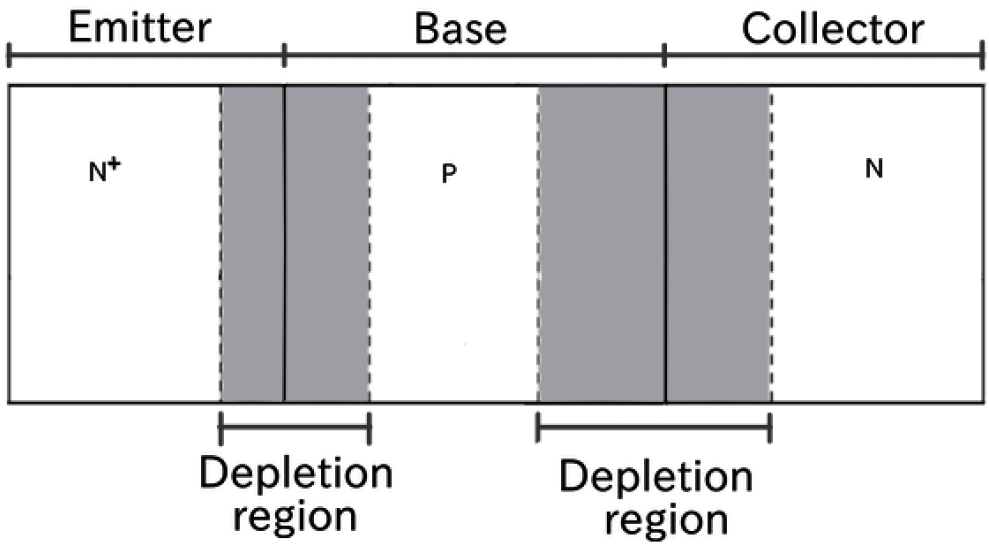


*Figure 12: Schematic illustration of an npn BJT. The difference in the depletion region into different areas of the BJT is due to different doping concentrations for the two n-sides. A higher doping concentration reduces the depletion depth in that region.*

### 2.5.1 Operation

The BJT has four modes of operation, depending on the bias of the two junctions, called forward active mode, reverse active mode, off mode, and on mode. In forward active mode, the emitter-base junction is forward biased while the collector-base is reverse biased. In the opposite situation, where the emitter-base junction is reverse biased, and the collector-base junction is forward biased there is reverse active mode. For on mode, also called saturation mode, both the junctions are forward biased, in opposition to the off mode where both junctions are reverse biased.

As an introduction to understanding the current flow in a BJT, an active mode n-p-n BJT is considered. Electrons are ejected from the emitter into the base by the forward bias of the emitter-base junction. This creates an excess concentration of minority carriers (electrons) in the base, further resulting in a large electron concentration gradient through the base, a sketch of the minority charge carrier concentration is given in Figure 13. The concentration gradient causes the diffusion of electrons over the base region towards the collector side. For electrons to cross the base region while avoiding recombination with holes, the base width needs to be lesser than the minority carrier diffusion length of the base material. A reduction in base width will also increase the minority carrier concentration, further increasing the diffusion current. When the electrons reach the collector-base depletion region, the electric field will sweep the electrons into the collector terminal.

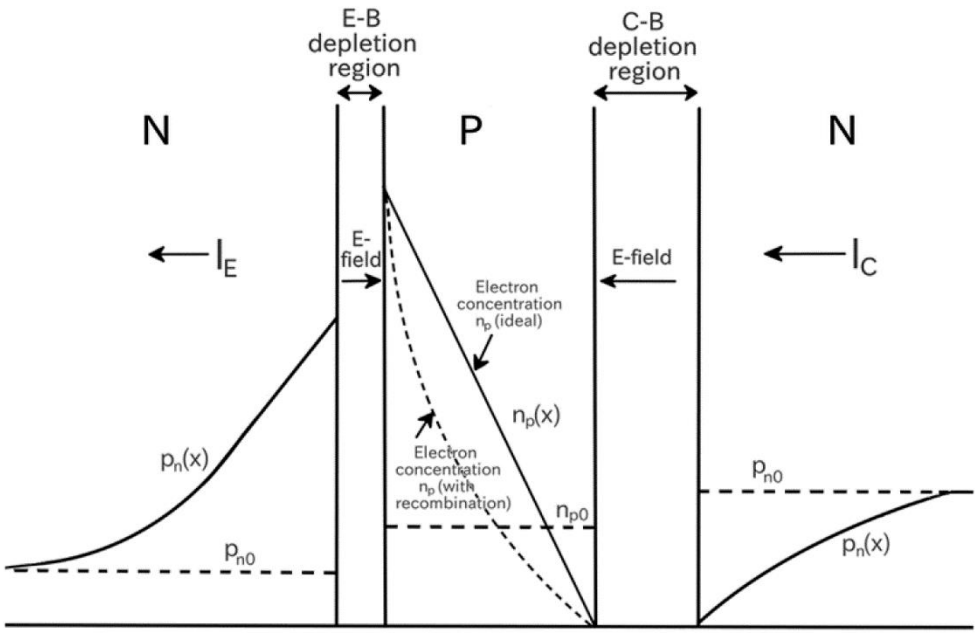


*Figure 13: Minority carrier concentration in an npn BJT. Hole and electron concentration is represented by $p_n$ and $n_p$, respectively. Thermal equilibrium of holes in the emitter and collector, and electrons in the base is termed $p_{n0}$, and $n_{p0}$, respectively. Recombination in the base alters the electron concentration from the ideal linear electron concentration.*

There are three main currents in the BJT called the emitter current, $I_E$, base current, $I_B$, and collector current, $I_C$, which are related by $I_E = I_B + I_C$. These are composed of different current-generating mechanisms throughout the transistor, all shown in Figure 14. The collector current is composed of the current generated from electrons injected from the emitter to the base, $I_{En}$, the current generated from holes injected from base to emitter, $I_{Ep}$, and the recombination current generated in the depletion region of the emitter-base junction, $I_{BEr}$. The base current is composed of the current generated when some of the electrons diffusing through the base recombine with holes, $I_{Br}$, the current generated from holes in the collector that are swept to the base, $I_{Cp}$, as well as $I_{Ep}$ and $I_{BEr}$. The collector current is composed of $I_{En}$, $I_{Br,}$ and $I_{Cp}$. In summary, the total currents of the emitter, base, and collector are given as

$$I_E = I_{En} + I_{Ep} + I_{BEr} \tag{31}$$

$$I_B = I_{Ep} + I_{Br} + I_{BEr} - I_{Cp} \tag{32}$$

$$I_C = I_{En} + I_{Cp} - I_{Br} \tag{33}$$

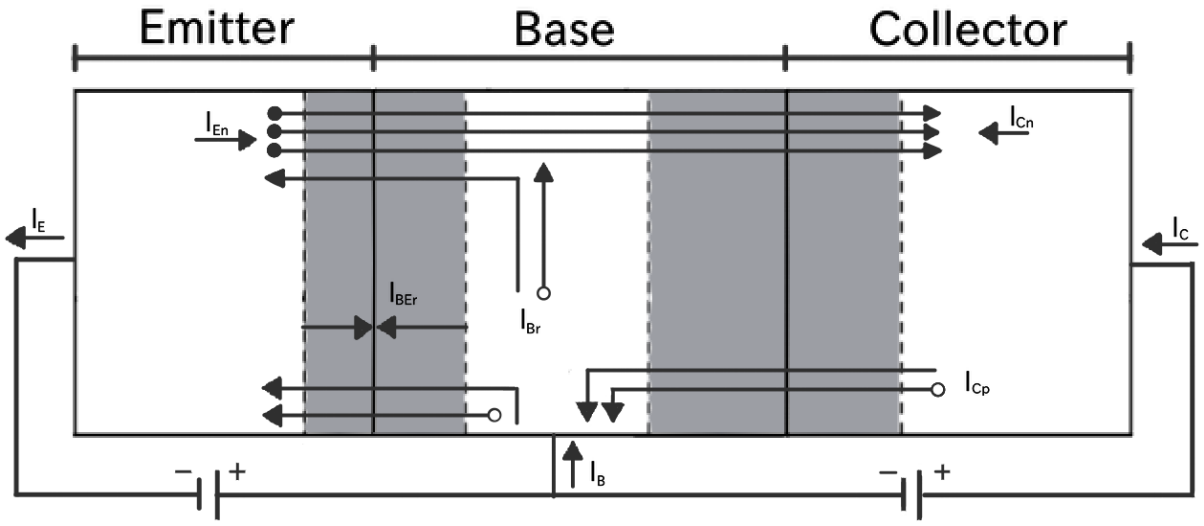


*Figure 14: Current flow in an npn transistor in forward active mode. The emitter-base junction is forward biased, while the committer-base junction is reverse biased.*

An important parameter of the BJT is the current gain, which can be divided into the common-base current gain, $\alpha$, and the common-emitter current gain, $\beta$. In common-base configuration, the base terminal of the transistor is common in both the input and output circuit, and $I_E$ is the input variable and $I_C$ is the output variable. The common-base current gain is approximately the current gain from emitter to collector. Ideally, this value is close to unity, only less because of recombination. The common-emitter current gain can be given as

$$\alpha = \frac{I_C}{I_E} \tag{34}$$

And for the common-emitter configuration, the emitter terminal is common in both input and output current. Here, $I_B$ is the input variable and $I_C$ is the output variable. The common-emitter current gain is approximately the ratio of the collector current to the base current. Combining the relation between the three-terminal currents and equation (alpha equation), we get

$$\beta = \frac{I_C}{I_B} = \frac{I_C}{I_C(1-\alpha)} = \frac{\alpha}{1-\alpha} \tag{35}$$

The common emitter mode is the most widely used circuit configuration, therefore, current gain is often referred to as the common-emitter current gain $\beta$.

# 3 Literature

In this section, a review of the literature relevant to this thesis will be presented. Starting with the literature on the two oxides of ZnO and NiO. Moving on, a review of the literature on the diffusion between the two materials is presented. Thereby, a review of the p-n junction of NiO-ZnO junction is presented, followed by a review of transistors constructed with the NiO-ZnO system. Finally, literature found on the deposition of ZnO and NiO is presented, as this is an important part of the making of semiconductor devices.

## 3.1 NiO and ZnO

### 3.1.1 ZnO

ZnO is classified as a semiconductor with a wide bandgap of 3.37 eV to 3.44 eV. High thermal and mechanical stability at room temperature, combined with high transmittance, has gained ZnO attention for its possibility within transparent electronic devices[2-6]. Because of unique physical and chemical properties, such as high chemical stability, low toxicity, hardness and rigidity, ZnO is a material also used in a wide area of applications, such as in ceramics, biomedicine, and cosmetics[7-10]. ZnO can form cubic zinc-blende, rock salt, or hexagonal wurtzite crystal structure, with the wurtzite structure being the most common and thermodynamically stable structure at ambient conditions. This structure is a space group $P6_3mc$ with lattice constants of a = 3.2496 Å and c = 5.2042 Å [11]. ZnO hexagonal wurtzite crystal structure consists of tetrahedral coordination of $O^{2-}$ and $Zn^{2+}$ ions stacked in individual planes along with the c-axis. Because of this tetrahedral coordination, ZnO has a non-central symmetric structure which causes piezoelectric and pyroelectric behavior [12]. Illustration of the hexagonal crystal structure is given in Figure 15.

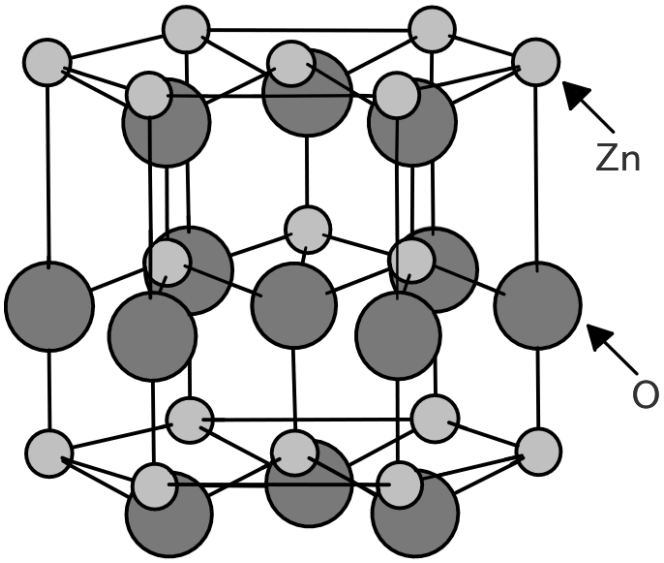


*Figure 15: Hexagonal wurtzite crystal structure of ZnO. The dark-gray spheres represent oxygen atoms and the light-gray spheres represent zink atoms.*

The ideal defect-free structure of ZnO acts as an insulator. However, obtaining insulating ZnO crystal structure has been proven difficult as small defect concentrations within the lattice will contribute to an n-type conductivity. Therefore, as-grown ZnO samples are usually unintentionally n-type [13]. Zn interstitials and oxygen vacancies are intrinsic defects in ZnO which have been invoked as sources for its n-type conductivity [13, 14]. However, the discussion on whether Zn interstitials or O vacancy is the dominant electron donor is not entirely agreed upon within literature. Zn interstitials are shallow donors with high formation energy, while oxygen vacancies display a deep donor level and low formation energy [15, 16]. The high formation energy of Zn interstitials argues they are not the major source for carrier electrons, while the shallow donor levels argue in favor of Zn interstitials being the major source. The same arguments go for oxygen interstitials, but in the opposite, favored for having low formation energy and discarded for having deep donor levels. Hydrogen has also been suggested as an unintentional defect causing n-type conductivity, as it can act as a shallow donor when substituted at the oxygen site [17, 18].

The n-type conductivity in ZnO can also be intentionally increased, by introducing donor impurities from group-III elements in the periodic table, such as boron, aluminum, gallium, and indium. These impurities act as shallow donors when substituted on the Zn site, therefore increasing the majority defect concentration [13]. Thin-film ZnO doped with aluminum has been shown to have an increase in electrical conductivity when compared to an un-doped ZnO film [19, 20]. Increasing the doping concentration of Al in ZnO ($Zn_{1-x}Al_xO$) show a monotonic increase in the electrical conductivity to the point of x = 0.02, reaching a conductivity of 1000 S/cm, further increase resulted in a slight decrease of conductivity [21]. Figure 16 shows the temperature dependency of ZnO with different doping concentrations, evidently showing conductivity values of doped ZnO that are over three orders of magnitude higher than un-doped ZnO at room temperature. Following equation 24, $Al^{3+}$ ions replace Zn in the crystal structure, hence introducing a free electron to increase the charge carrier concentration, consequently increasing the electric conductivity.

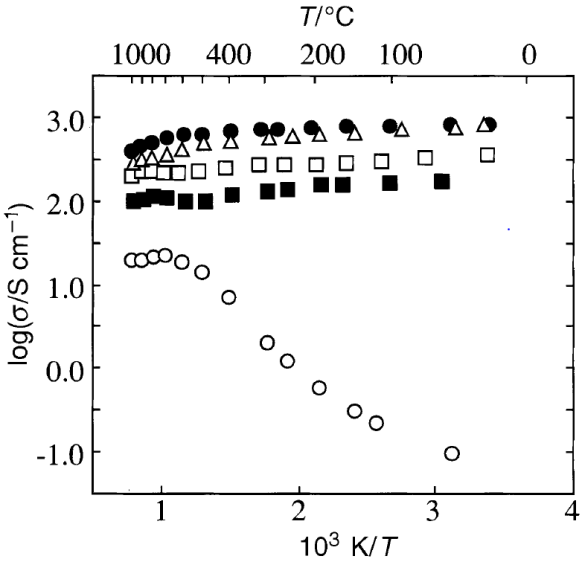


*Figure 16: Arrhenius plots for the electrical conductivities of $Zn_{1-x}Al_xO$ in ambient air for x=0 (○), 0.005 (■), 0.01 (□), 0.02 (●), 0.05 (Δ) [20].*

### 3.1.2 NiO

NiO is a p-type semiconductor with a wide bandgap of 3.6-4.0 eV. Because of its chemical stability and interesting optical, electrical, and magnetic properties, NiO is applicable for a wide range of applications [22-24]. In recent years, NiO's ability to be used as transparent conducting films have attained a lot of attention, as this paves the way for smart windows and transparent solar cells [25-27]. Bulk NiO exhibit antiferromagnetic behavior below the Neel temperature, however, nano-sized NiO is known to have different magnetic properties compared to bulk NiO [28]. NiO forms a simple rock salt structure with octahedral coordination of $Ni^{2+}$ and $O^{2-}$, where every ion is surrounded by six oppositely charged ions, as illustrated in Figure 17. This is a structure with space group Fm3m, and a structure parameter of a = 4.1769 Å at room temperature [29, 30].

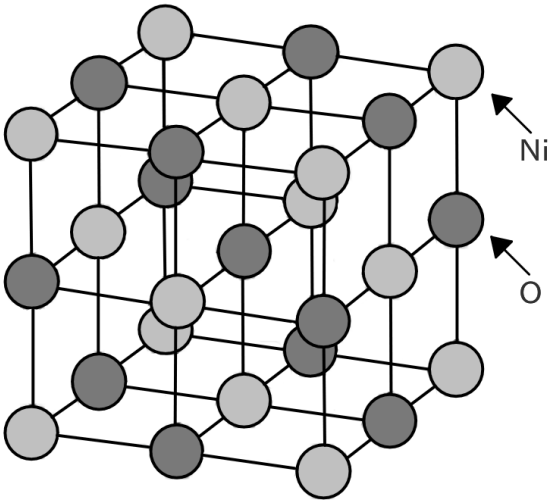


*Figure 17: Rock salt structure of NiO. The dark-gray spheres represent oxygen atoms and the light-gray spheres represent nickel atoms.*

As in the case for ZnO, NiO also behaves as an insulator when stoichiometric, however, the almost unavoidable presence of impurities or lattice defects effectively creates electric conductivity in NiO [31]. Metal deficiency in the form of charged nickel vacancies, $Ni^{2+}$ and $Ni^{+}$, compensated by electron holes within the lattice is assumed to be the dominating defects in NiO. Doubly charged nickel vacancies are assumed to be of higher concentration compared to singly charged nickel vacancies [32]. Oxygen interstitials have also been argued as a contributor to p-type conductivity [33, 34].

Acceptor doping of NiO, with group-I elements, such as lithium, sodium, and potassium is found to increase the conductivity [35]. Multiple studies conclude on the increase in electric conductivity by acceptor doping with lithium ions, which can be attributed to the substitutional sites being occupied by $Li^{+}$ ions, creating an increase in majority carrier concentration. Doping concentration resulting in maximum conductance varies, as it depends on the deposition method and parameters used under deposition. However, a doping concentration in the range of x = 0.02 to x = 0.09 seems to be an interval where the lowest resistivity is reached. A further increase in doping concentration results in decreased conductance [35-37]. Figure 18 shows the effect on resistivity by doping NiO with different concentrations. One can see that the doped samples reach a much lower resistivity compared to the un-doped NiO. All samples show a decrease in resistivity with the increase of temperature, this trend also seems to decrease as the doping levels increase.

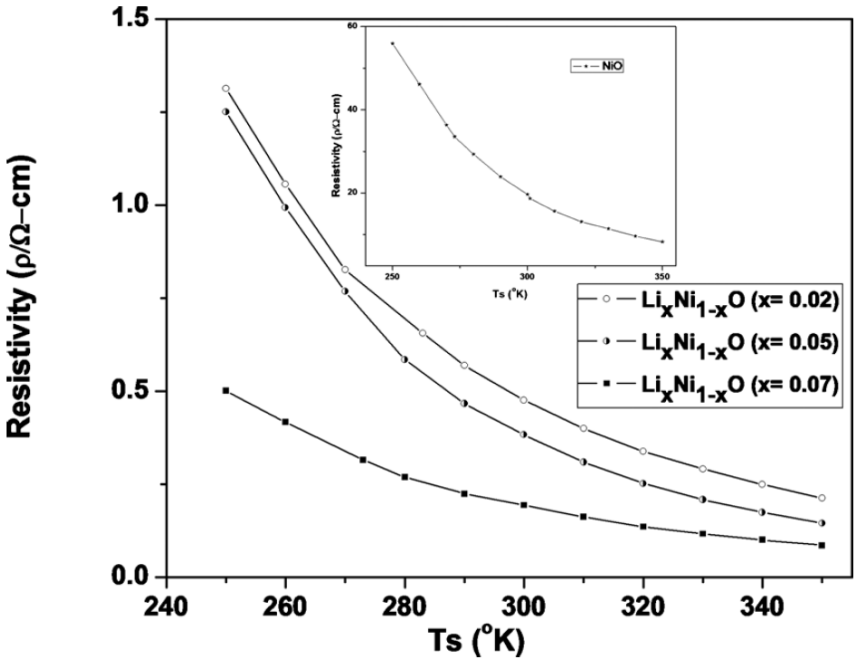


*Figure 18: Dependence of resistivity with respect to temperature in ambient air for different concentrations (x=0.02, x=0.05, and x=0.07) of $Li_xNi_{1-x}O$ thin films. The inset shows the resistivity behavior of un-doped NiO [37].*

## 3.3 Solid solubility and diffusion

Even though the NiO-ZnO system is well known and researched, investigations on the solubility and diffusion within the system are limited. ZnO and NiO have different crystal structures, hence limiting their solubility within each other. However, the radii of $Ni^{2+}$ and $Zn^{2+}$ ions are very much alike (0.69 Å and =.74 Å, respectively), hence interdiffusion of these might occur [38]. Some efforts in researching the solubility and interdiffusion of the NiO-ZnO system have been conducted. Kurokawa et al. developed a phase diagram of the NiO-ZnO system, showing a solubility of about 3% Ni in ZnO and 27% Zn in NiO, shown in Figure 19. These solubility limits are slightly dependent on temperature up to temperatures of about 1200 °C, where the solubility increases more rapidly for both. When conducting I-V measurements of equilibrated compounds of the NiO-ZnO junction, they concluded that the junction is stable at high temperatures over long periods [39]. These findings in solubility are in good agreement with phase diagram developed by Bates et al, however, Bates concluded in a slightly lesser solubility for both Ni in ZnO and Zn in NiO [40].

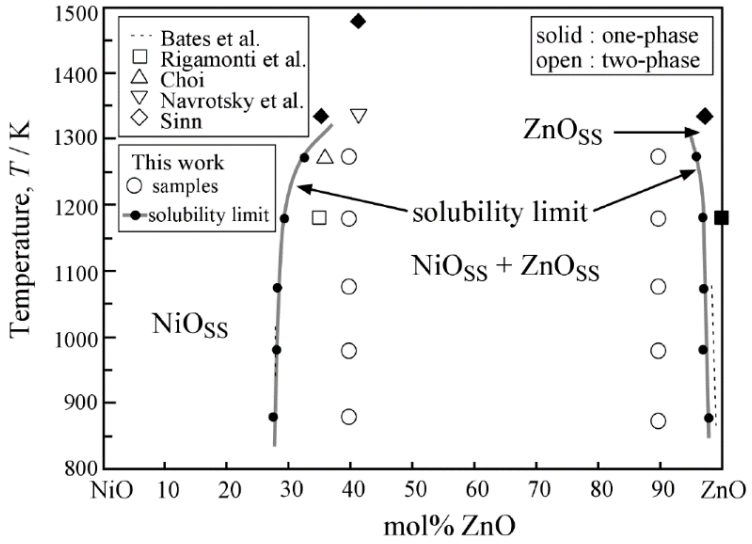


*Figure 19: Phase diagram of the NiO-ZnO system [51], showing approximately 30% solubility of Zn in NiO and 5% Ni in ZnO [39].*

Desissa et al. reported on the diffusion between ZnO:Al and NiO:Li [41]. It was found that $Zn^{2+}$ mainly diffuses into NiO:Li by bulk diffusion, whereas $Ni^{2+}$ diffuses into ZnO:Al by bulk and grain boundary diffusion, hence resulting in a larger diffusion length of $Ni^{2+}$ into ZnO:Al compared to that of $Zn^{2+}$ into NiO:Li. The diffusion length was calculated to be 200 µm for $Ni^{2+}$ into ZnO:Al at 900 °C over a period of five years, and 20 µm for $Zn^{2+}$ into NiO:Li under the same conditions, showing that the diffusion length is limited but must be considered for sensitive applications. Shown in Figure 20, is an interdiffusion profile for $Ni^{2+}$ and $Zn^{2+}$ in the NiO-ZnO system, obtained by Desissa. Here one can see the quantity of $Ni^{2+}$ in ZnO starts below 5 at. % and the quantity for $Zn^{2+}$ in NiO starts below 25 at. %. These results agree with the phase diagram of the NiO-ZnO system.

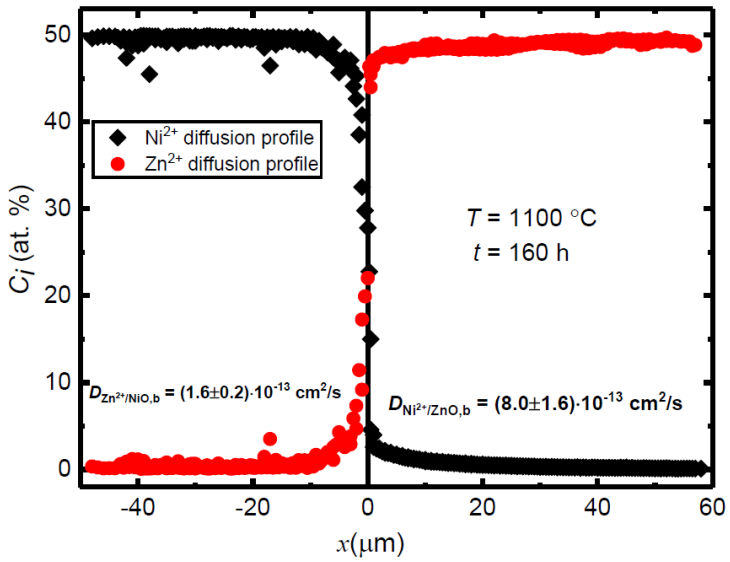


*Figure 20: Diffusion profile of cations in the diffusion couple of Ni0.98Li0.02O/Zn0.98Al0.02O annealed at 1100 °C for 160 h [41].*

## 3.4 NiO-ZnO junction

The valence band and conduction band offsets have been reported with significantly different values. Valence band offsets are reported in the ranges of 1.3 eV - 1.6 eV [42-45] and 2.6-2.9 at ambient temperatures [46-48]. The conduction band offset is reported in two common ranges of 1.80 eV - 2.0 eV [42-45] and 2.82 eV - 3.2 eV at ambient temperature [46-48]. Even though these values vary, there is a general agreement that the band alignment is a staggered gap alignment (type II-2). However, studies have also found the NiO-ZnO junction to have a broken bandgap alignment, shown in figure 21, with the most reported bandgap alignment for the NiO-ZnO system, type-II band alignment [49]. The work function of NiO, $\varphi_{NiO}$, and ZnO, $\varphi_{ZnO}$, is reported to be 5.4 eV and 4.6 eV, respectively [50, 51]. This corresponds to a built in potential of 0.8 eV.

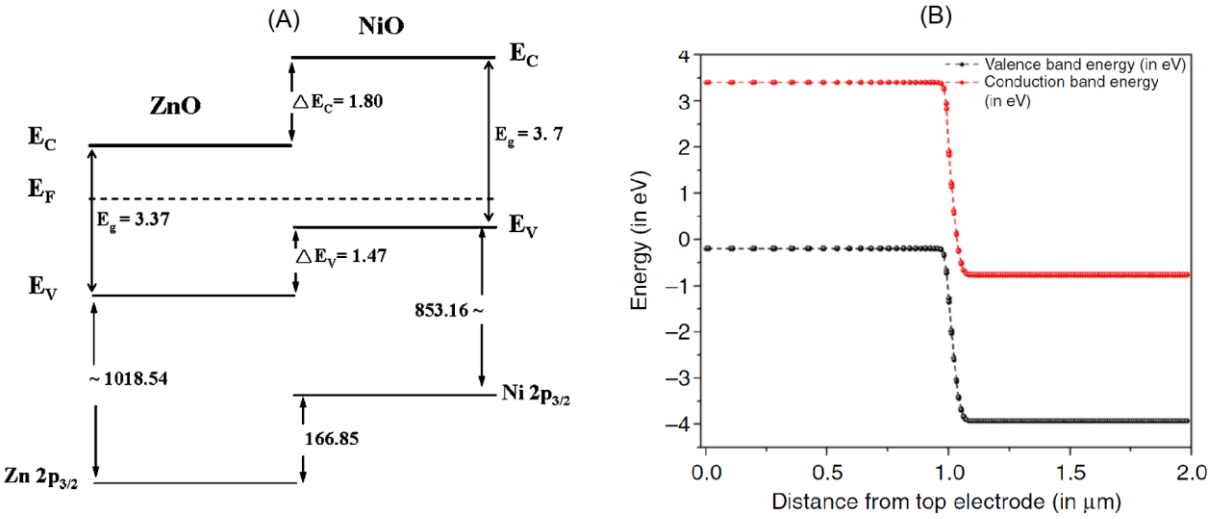


*Figure 21: (A) Schematic diagram of the type-II band alignment of p-NiO/n-ZnO heterojunction [43]. (B) band diagram of NiO/ZnO heterojunction sensor device showing broken type (type III) heterojunction formation [49].*

NiO-ZnO junctions have been studied for a wide variety of applications. Hasan and colleagues found that low-temperature fabrication of NiO-ZnO junctions exhibit excellent UV sensitivity and can be used as photodetectors [52]. Patel et al. fabricated an all transparent solar cell of NiO-ZnO, with a transparency of 69.6% and an efficiency of 6.0%, which is a relatively good transparent solar cell compared with other transparent solar cells [25, 53]. Imen et al. fabricated a NiO-ZnO diode using a spin coating method, resulting in a rectifying behavior of the junction, shown in figure 22 (B) [54]. Using the PLD-method to fabricate a NiO-ZnO diode, Gupta et al. also concluded in the rectifying behavior, shown in figure (A) [55]. Both Imen and Gupta proposed that the high ideality factor in these diodes is due to accelerated recombination of electrons and holes in the depletion region or by the presence of an interfacial layer. The rectifying I-V characteristics of the NiO-ZnO junction is reported by multiple studies [56, 57].

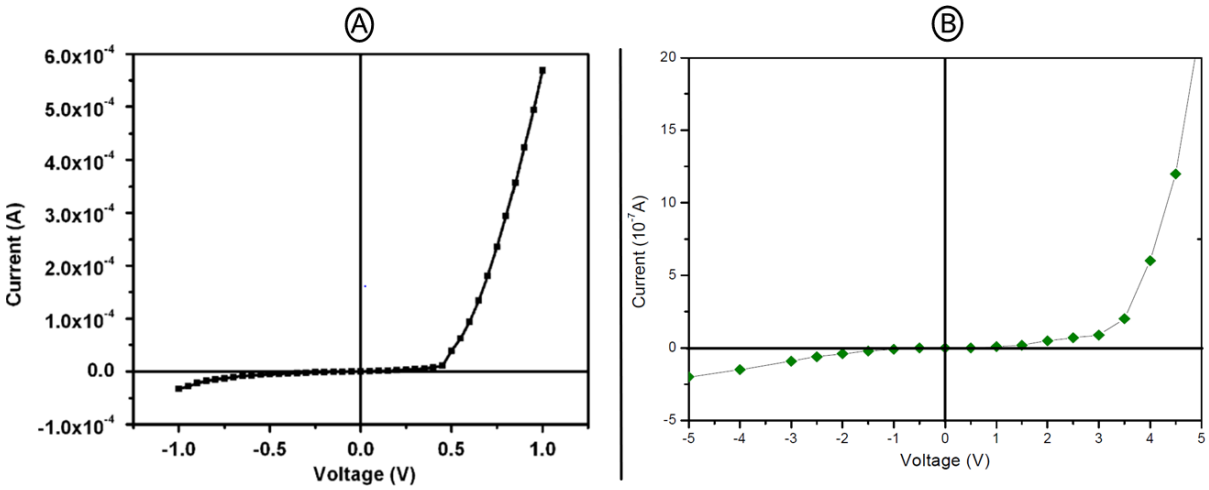


*Figure 22: (A) I-V characteristics of a NiO-ZnO p-n junction made with PLD method [55]. (B) I-V characteristics of a NiO-ZnO p-n junction made with sol-gel method [54].*

Desissa et al. investigated the properties of polycrystalline p-type $Ni_{0.98}Li_{0.02}O$ and n-type $Zn_{0.98}Al_{0.02}O$ p-n junction in a temperature range from 500 °C to 1000 °C []. The current density plotted against the applied voltage is shown in figure 23 (A). At 500 °C, there is rectifying behavior. However, the rectification is reduced by the increase in temperature. In addition, an investigation on the incorporation of a composite of the individual layers at the interface, forming a p-c-p junction, was demonstrated. The results showed a reduction of the interface resistance, *j*, by order of magnitude. Figure 23 presents the results of this composite interface layer compared to the p-n junction.

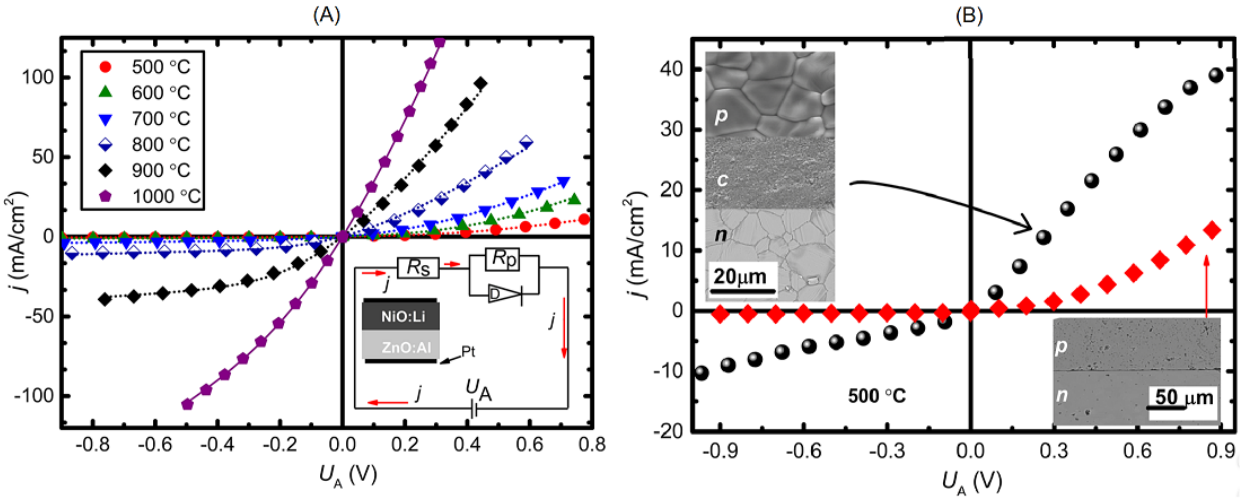


*Figure 23: (A) Current density–voltage (j–UA) characteristics of Ni0.98- Li0.02O-Zn0.98Al0.02O heterojunction at 500–1000C. The inset shows a schematic of an equivalent circuit of the p–n heterojunction. (B) j–UA curves of the Ni0.98Li0.02O-Zn0.98Al0.02O p–n junction at 500C of two junctions with different interface morphologies. The upper inset shows a micrograph of the materials forming the p–c–n junction (the scale bar is representing the three microstructures), while the lower inset exhibits a micrograph of the p–n junction sample.*

## 3.5 NiO-ZnO based transistor

Using the NiO-ZnO junction to construct a transistor has not been researched notably, however, some efforts have been made. A highly transparent junction field-effect transistor (JFET) was successfully fabricated by Karsthof and colleagues using the PLD as a deposition method [58]. The transistor was tested at temperatures up to 100 °C. The ON-voltage of the transistor shifted from -3.43 V at 10 C to -2.92 V at 100 C. This shift towards a more positive voltage was attributed to the acceptor-like trap states at the channel/gate interface (the NiO-ZnO interface). When going back to room temperature, the ON-voltage remained at slightly reduced voltages. The origin of this reduced ON-voltage was suggested to be an annealing effect on the defect states. Fabrication of a ZnO-NiO-Si thin-film BJT, also deposited with the PLD method has also been investigated [59]. The study found transistor behavior at higher base voltages, whereas at lower voltages the base-collector junction (NiO-ZnO junction) was not reverse biased resulting in a linear increase in collector current with the increase of output voltage. The effect of an applied magnetic field was also investigated with the interesting result of an increase in collector current with the applied magnetic field, shown in figure 24(A). This was attributed to the presence of ferromagnetism, created by nickel or oxygen vacancies in the NiO thin film. This magnetic sensitivity is highly interesting as it can be utilized for future spintronic applications. They also found the NiO-ZnO junction to have an ideality factor of 3.25, similar to the diodes of NiO-ZnO made by Imen and Gupta, previously mentioned in section 3.3.

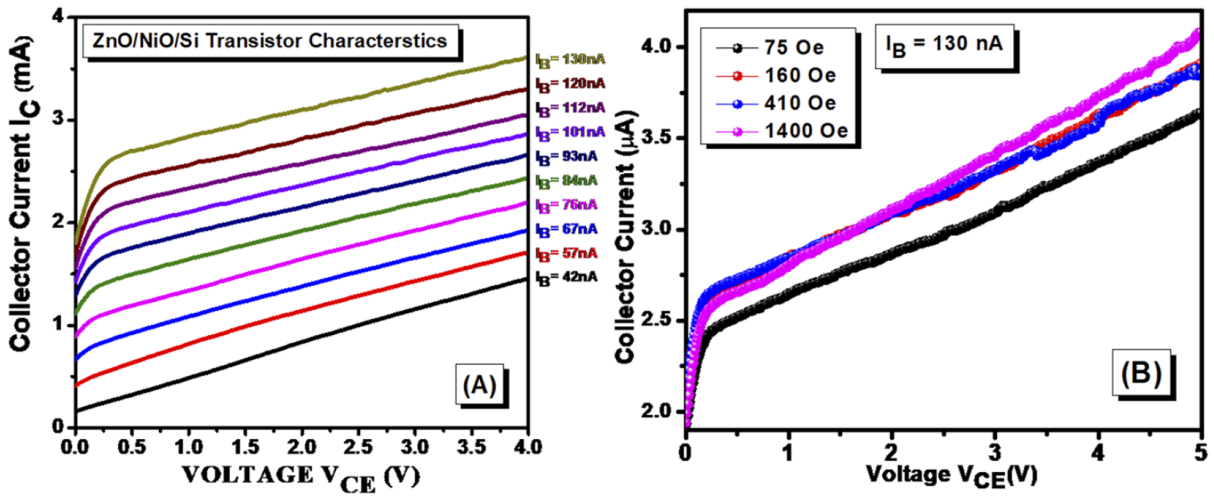


*Figure 24: Output characteristics of a PLD constructed ZnO-NiO-Si BJT, with (A) various applied base current, and (B) for various magnetic fields with a fixed base current of 130 nA [59].*

## 3.6 Pulsed laser deposition of ZnO and NiO

PLD is a is established as one of the simpler, cheaper, and more versatile methods of depositing high-quality thin films of a very diverse range of materials, such as oxides [60]. The attractiveness of the PLD is due to its simplicity and advantages such as the stoichiometric transfer of complex compositions from bulk target to substrate deposition and low crystalizing temperature [60, 61]. Even though this technique is simple, the quality of the deposited film is highly dependent parameters such as background pressure, laser wavelength and energy, and substrate temperature. Altering these parameters will affect the crystallinity and functional properties of the deposited thin film.

### 3.6.1 ZnO

Already in the early '80s, Sankur *et al.* found that the laser deposition technique was applicable for producing high-quality ZnO films, as they managed to deposit highly oriented, crystalline, and conducting films of ZnO [62]. Since then, PLD has been frequently reported as a method for ZnO film growth. One of the important parameters in film growth when using PLD is the substrate temperature. Research indicates that thin-film growth of ZnO at room temperature will result in an amorphous film, whereas thin-films grown at higher temperatures, between approximately 300 – 450 °C, show high crystallinity [63, 64]. Figure 25 shows the diffractogram of thin-film ZnO grown at different substrate temperatures. The diffractogram shows no preferred orientation at room temperature, whereas at higher temperatures there is one clear peak corresponding to (002) plane indicating the films are highly oriented and single crystal in nature. At even higher temperatures a second peak appears, indicating polycrystalline film. Ghosh et al. contributed the single-crystal nature of ZnO thin films grown at temperatures exceeding room temperature to the surface mobility of the impinging atoms being sufficient enough to allow atoms to occupy propper ZnO lattice sites, and that the polycrystalline nature of films grown at sufficiently high temperatures is due to the mobility now being high enough to knock atoms from their preferred lattice sites[63].

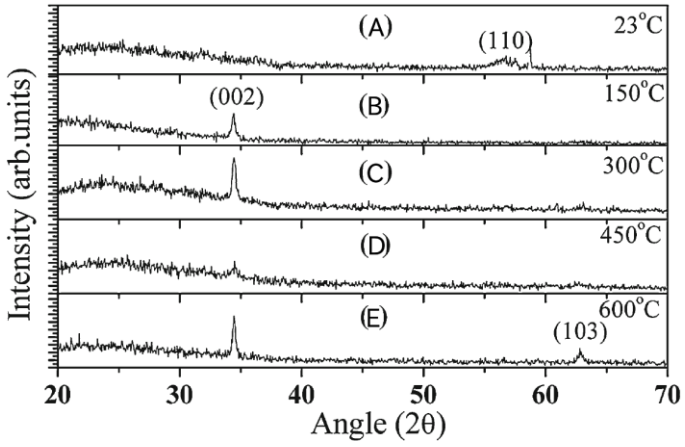


*Figure 25: Diffractograms of ZnO thin films deposited on Si substrate at 0.1 bar $O_2$ pressure at a temperature of RT (A), 150 °C (B), 300 °C (C), 450 °C (D), and 600 °C (E) [64].*

Another important parameter is the background gas. Films deposited with low oxygen pressure show an increase in conductivity, compared with films grown at higher oxygen pressures [62, 64]. This increase in conductivity can be explained by the native n-type conductivity of ZnO, where oxygen vacancies and zinc interstitials are compensated by electrons. A high background pressure of oxygen will decrease the oxygen vacancies, resulting in a reduced majority carrier concentration. However, higher oxygen pressures give a higher crystallinity of the deposited film [63]. Robin Scott and colleagues investigated using argon gas as a replacement for oxygen in the deposition of gallium doped ZnO [65]. They found that the deposited film was highly conductive and attributed this mainly to the incorporation of gallium on donor sites. They also discussed the possibility of argon gas improving conductivity by inhibiting the formation of $V_{Zn}$ acceptors and $O_2$ acceptors. This might also have the same effect for pure ZnO, or ZnO doped with other donor dopants, such as aluminum. As mentioned earlier, ZnO doped with aluminum will significantly increase the conductivity as aluminum introduces free electrons into the ZnO structure. However, resistivity reported for Al-doped ZnO deposited by PLD varies, some reports show relatively high resistivity of 10 Ωcm, whereas others accomplish lower values of 5.8 x $10^{-4}$ Ωcm [66, 67]. The many combinations of deposition parameters are responsible for the variety in resistivity and other material properties. Aluminum also affects the crystallinity of the film, as Al introduces compressive stress to the ZnO lattice which increases with increasing thickness [68]. The good optical transparency seen in ZnO seems to be obtained and show little influence by the Al donor dopant [67, 68].

### 2.6.2 NiO

As for ZnO, thin films of NiO have been deposited by PLD with numerous combinations of background gasses, substrate temperatures, and laser energies, creating films with different characteristics. A common result is that increasing the substrate temperature will increase the crystallinity of the thin film. However, an increase in crystallinity has also resulted in an increase of resistivity, as can be seen in Figure 26 [69, 70]. Fasaki *et al.* attributed the increase in resistivity to NiO`s conductivity being strongly related to the formation of microstructural defects such as $V_{Ni}$ and $O_i$, thus the reduction of these defects by the enhanced crystallinity when increasing substrate temperature will result in a higher resistivity [70]. Kakehi and colleagues successfully fabricated epitaxial films of NiO at room temperature and found a correlation between oxygen partial pressure and resistivity of the film [71]. It was found that resistivity increased with increasing oxygen pressure until oxygen pressure exceeded 1.3 x $10^{-1}$ Pa, where the resistivity decreased sharply. However, Oka *et al.* found that the resistivity keeps increasing with increasing oxygen pressure when growing the NiO film at 300 °C and found no turning point like that of Yoshiharus results [69].

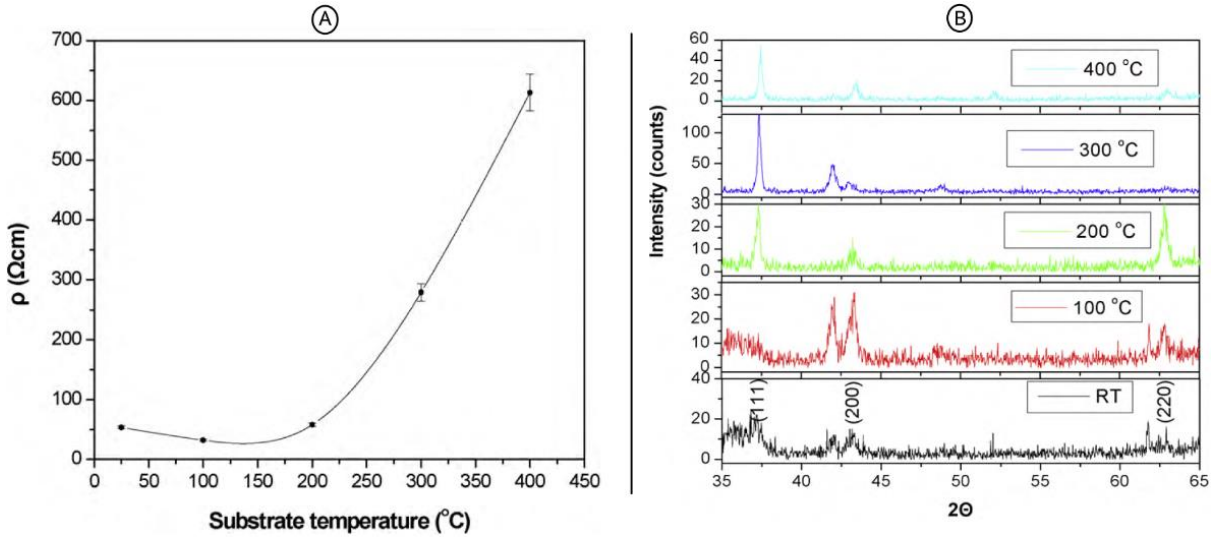


*Figure 26: (A) Resistivity as a function of a substrate temperature of NiO films deposited on a Si substrate using the PLD method. (B) Diffractogram of NiO thin film deposited on Si substrates at different temperatures. At temperatures equal to, or higher, than 200 °C, the main peak corresponds to the (111) plane [70].*

As mentioned earlier, doping NiO with an acceptor dopant will increase its electric conductivity. Lithium doped NiO thin films have been successfully fabricated using the PLD method. Huang and colleagues managed to reach a resistivity of 6.77 x $10^{-2}$ Ωcm in a Li doped NiO thin film [72]. They also found that the resistivity dropped monotonically with the increase of oxygen pressure, in contrast to that of un-doped NiO. This decrease in resistivity with the increase in oxygen pressure for Li doped NiO was also found by Dutta and colleagues [37].

A repetitive result in the articles mentioned above and others, is the non-crystalline growth of NiO together with ZnO, as its usually polycrystalline or amorphous under inspection [55]. However, Ohta et al reported that even though there is a large mismatch between the O-O spacing of ZnO and NiO at the interface, the atomic configurations at the interface are connected smoothly, confirming that hetero-epitaxial growth has been achieved [56]. Dutta et al raised the concern of the electrical properties' dependence on microstructure and crystalline quality of the thin film in solid-state devices, as grain boundaries and interface states in polycrystalline films can provide traps and recombination centers. They solved this by inserting a MgZnO layer between the ZnO and NiO:Li layer, resulting in improved I-V characteristics of the junction due to the reduced leakage current [55]. For ZnO, crystalline thin films are highly attainable, with few exceptions showing non-crystallinity [52]. Evidently, for both NiO and ZnO, doped and un-doped, the resulting characteristics of the deposited thin film heavily rely on the parameters used under deposition. Electric conductivity is for both materials heavily dependent on the microstructure and therefore affected by the deposition parameters.

# 4 Experimental

In this chapter, an overview of the experimental methods and the equipment used through this thesis is given. Firstly, sample preparation is presented, from pellet pressing to deposition of the materials through PLD. Secondly, sample characterization is presented, starting with XRD, SEM, and TEM before moving on to electrical measurements.

## 4.1 Sample preparation

In order to construct a BJT, two main procedures have ensured. Firstly, the construction of a target material to be used in the PLD was accomplished with the use of powdered materials, pellet pressing, and sintering. Secondly, these target materials were then used in the PLD to construct the final BJT on top of a substrate, with several separate deposition steps in the PLD.

### 4.1.1 Pellet manufacturing

Purchased powders Zinc oxide, (Sigma-Aldrich) aluminum-doped zinc oxide ($Zn_{0.98}Al_{0.02}O$), and lithium doped nickel oxide ($Ni_{0.98}Li_{0.02}O$) (Cerpotech) were used to make two separate pellets as target materials for the PLD. Two grams powder of both $Zn_{0.98}Al_{0.02}O$ and $Ni_{0.98}Li_{0.02}O$ were ground in separate mortars. For each gram of powder, 17 drops of binder (B60/B709, Mix with ethyl acetate) was added to both powders. The binder-powder mix was then added to a die with a diameter of 20 mm, in separate rounds, and pressed with approximately ten tons of pressure in the press (Atlas Manual Hydraulic Press 15T, Specac) for optimal results. Covered in sacrificial powder, the pressed pellets were placed in a furnace under an ambient atmosphere where they were heated to 1400 °C with a ramp rate of 2.3 °C/min. The pellets were then annealed at 1400 °C for 12 hours before cooling down with the same ramp rate as for the initial heating. The sintered pellets were then lightly polished with sandpaper with a roughness of 500, 800, 1200, to even out the surface for a better target in the PLD.

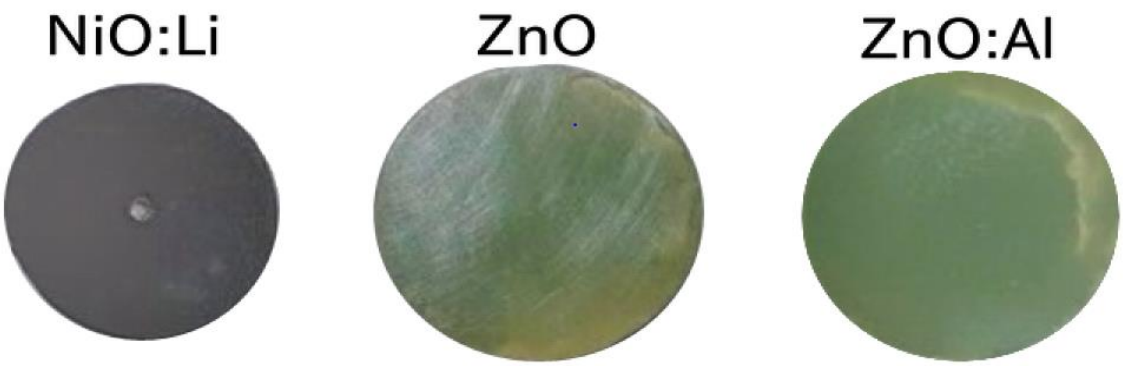


Figure 27: Pellets produced from powders, from the left is NiO:Li, ZnO, and ZnO:Al.

### 4.1.2 Pulsed laser deposition

Pulsed laser deposition (PLD) is a physical vapor deposition process (PVD) and is a technique to grow high-quality thin films. The technique uses a pulsed laser with enough energy laser density to vaporize or ablate a thin layer of the target material, creating a plasma plume of the evaporated target material. The plasma plume is directed toward a substrate material where the thin film growth is initiated. This process is carried out within a vacuum, or with the desired background gas. A schematic of the PLD process is shown in Figure 28. PLD is an attractive growth process because of its simplicity and ability for stoichiometric transfer from target material to the substrate. The technique can roughly be divided into three stages; laser ablation of the target material, dynamics of plasma plume, and the deposition and growth process on the substrate.

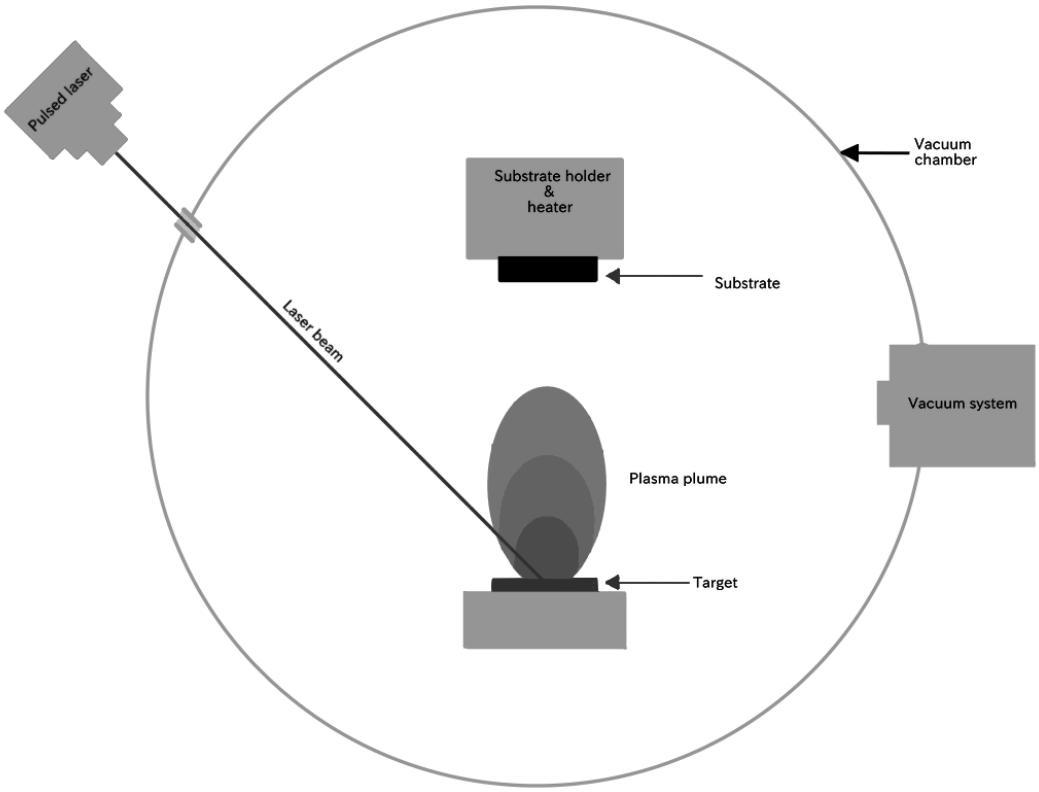


*Figure 28: Simplified schematic of a PLD vacuum chamber. A pulsed laser beam is focused towards the target material, placed directly under the substrate. The ablation of the material creates a plume that deposits the target material at the substrate.*

A pulsed laser is used to deliver high energy to a small area of the solid target material. With enough energy, right wavelength and angle relative to the target material, the target surface will be heated to the extent that there are evaporation and formation of a hot and partly ionized particle cloud. The pulsed laser creates a high heating rate at the target surface ($10^8$K/s), which leads to the nonequilibrium process of the ablation, which in turn leads to one of the main advantages of the PLD, the stoichiometric transfer from target material to the

substrate. The high heating rate also creates the ability for deposition of thin films at relatively low substrate temperatures, compared with other techniques such as molecular beam epitaxy.

The pulsed laser creates a partly ionized cloud from the target material, this partly ionized cloud will absorb energy from the laser pulses and become more and more ionized until a fully ionized plasma is achieved. The plasma is a mixture of ions, atoms, and free electrons from the evaporated target material. The shape and intensity of the plasma plume are dependent on the laser frequency, shooting angle, background gas, and the target material itself. The plasma plume, high in energy, expands rapidly away from the surface towards the substrate usually placed some centimeters away from, and normally, relative to the target.

If there is a sufficient plasma plume, and the substrate is placed within reach of the plume, condensation of the target material will appear at the substrate, and the initiation of thin-film growth will start. There are several different growth modes that can occur on the substrate, depending on how the atoms arrange themselves on the substrate, however, a detailed explanation of these modes is beyond the scope of this thesis.

To fabricate the BJT, the PLD was used to deposit thin-film layers of ZnO, NiO:Li, and ZnO:Al. Before deposition, substrates of $Al_2O_3$ were cleaned via sonication in ethanol for 10 minutes, then sonicated in water for 10 minutes before being dried in ambient air. The clean substrates were then attached to the PLD holder using a silver paste, the silver paste with the attached substrate was dried in a heating cabinet at 120 °C for 20 minutes. The target was placed underneath the substrate on a target holder, with a target to substrate distance of 5 cm. A “laser name” was used to deposit thin films. The laser energy, number of shots, substrate temperature, and background gas was set to appropriate values depending on the material being deposited, summarized in Table 3.1.

Table 3.1: Deposition parameters for the different materials deposited.

| **Target material** | **ZnO** | **NiO:Li** | **ZnO:Al** |
|---|---|---|---|
| Substrate temp (°C) | 400 | 200 | 200 |
| Background gas | Argon | Oxygen | Argon |
| Pressure (mbar) | $10^{-3}$ | $10^{-3}$ | $10^{-3}$ |
| # of shots | 40 000 | 10 000 | 20 000 |
| Energy (mJ) | 450 | 450 | 450 |

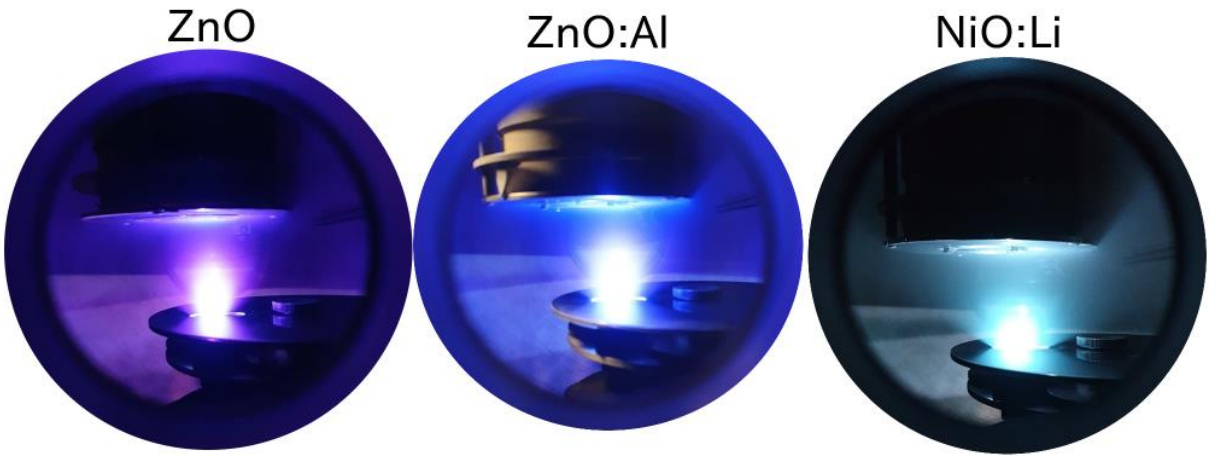


*Figure 29: From the left, the ejected plume of ZnO, ZnO:Al and NiO:Li is shown. The plume is ejected from the target material placed underneath the target cover, towards the substrate placed directly over the plume.*

In order to fabricate the BJT, a three-layered structure was layered using the PLD. The bottom layer, acting as the collector, was fabricated with the un-doped ZnO pellet as target material in the PLD. In order to create room for a terminal connection at the collector material, a mask was used to cover parts of the deposited ZnO. Ensuing the ZnO layer, NiO:Li was deposited as the base layer using the fabricate NiO:Li pellet as a target. This intermediate layer also had to be covered with a mask before the deposition of the final layer. With the base layer mask attached, the final ZnO:Al pellet was used to deposit the final emitter layer of the BJT, essentially completing the fabrication of a BJT. Alongside the manufacturing of the BJT, individual films of the materials were also fabricated.

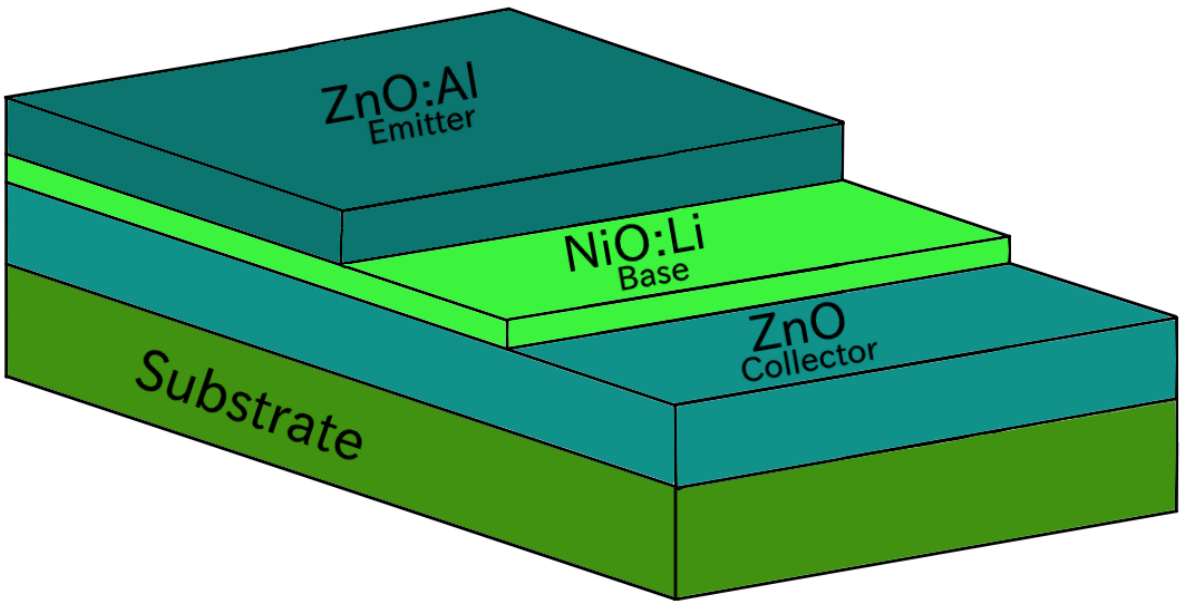


*Figure 30: Schematics representation of the constructed BJT. The BJT is constructed so all the layers have an open surface area, in order to have a connection area to the emitter, base, and collector.*

## 4.2 Sample characterization

### 4.2.1 X-Ray Diffraction

X-Ray Diffraction (XRD) uses X-rays aimed at a sample, that diffract in specific directions because of the sample crystal structure. These diffracted beams are then used to create a diffractogram, which can be analyzed by the angels and intensity of the peaks presented. This is a nondestructive technique to study structures, phases, preferred crystal orientation, and other structural parameters.

XRD was used to study the phase composition and crystal structure of deposited thin films, and the tree layered BJT, on a D8 Discover by Bruker with a $CuK_{\alpha,1}$ ($\lambda$ = 1.54060 Å) and $CuK_{\alpha,2}$ ($\lambda$ = 1.54439 Å) radiation. All samples were scanned in the range $10° \leq 2\Theta \geq 90°$ and step size of 5 °/s. In this work, the resulting diffractogram was managed using DIFFRAC.EVA by Bruker, and compared to the Crystallography Open Database.

### 4.2.2 Scanning Electron Microscopy

Scanning Electron Microscopy (SEM) uses a high-energy beam focused at a sample to study microstructure, surface morphology, and phase composition. The electrons accelerated into the sample results in interactions with the sample atoms and results in signals that are used to create an image. These signals include secondary electrons, backscattered electrons, visible light, and more.

All SEM images were taken on an FEI-SEM (FEI Quanta 200 FEG-ESEM), with a field emission gun containing three detectors. Secondary electrons were detected using an Everhart Thornley Detector (ETD), a Large Field Detector (LFD) is used for low vacuum and environmental SEM mode, and a Solid-State Detector (SSD) for high vacuum mode. The instrument was operated in high-vacuum mode ($10^{-5}$ Pa) mode with an acceleration voltage of 20Kv

### 4.2.3 Transmission Electron Microscopy

Transmission Electron Microscopy (TEM) can be employed to study materials in the nano- and micrometer range. By using a high-energy beam of electrons aimed at a thin sample, the interactions between the electrons from the beam and the atoms in the material can be analyzed to observe the crystal structure in the nano- and micro-scale, and perform chemical analysis. The main difference between the SEM and TEM is that TEM uses a transmitted electron to create an image, while SEM uses reflected electrons or knocked-off electrons.

In order to observe the p-n junction in TEM, there has to be a sample preparation. A small sample area of 3 x 6 mm is selected, and cut out of the sample with a micro-saw. This sample piece is cut in two, and the two pieces are, with the thin film layers facing each other, glued together in a "sandwiched". The glue used is a two-component glue and is cured for 10 minutes on a heat plate and left overnight. The following day, the sample is again cut in two, normal to the face to face layers. The sample is then glued onto a holder with Loctite before being thinned down to 500 µm, on one side perpendicular to the observed side. The sample is then thinned in an angle, and towards the end of the thinning process, a wedge was introduced in order to make the sample thinner than 50 µm. On top of the thinnest part of the sample, the center of a copper glued on, and the sample area around the ring is cut off. The procedure is illustrated in Figure 31. The sample is left overnight and mounted in a PIPS II system (Precision Ion Polishing System II, Gatan Inc) for further thinning.

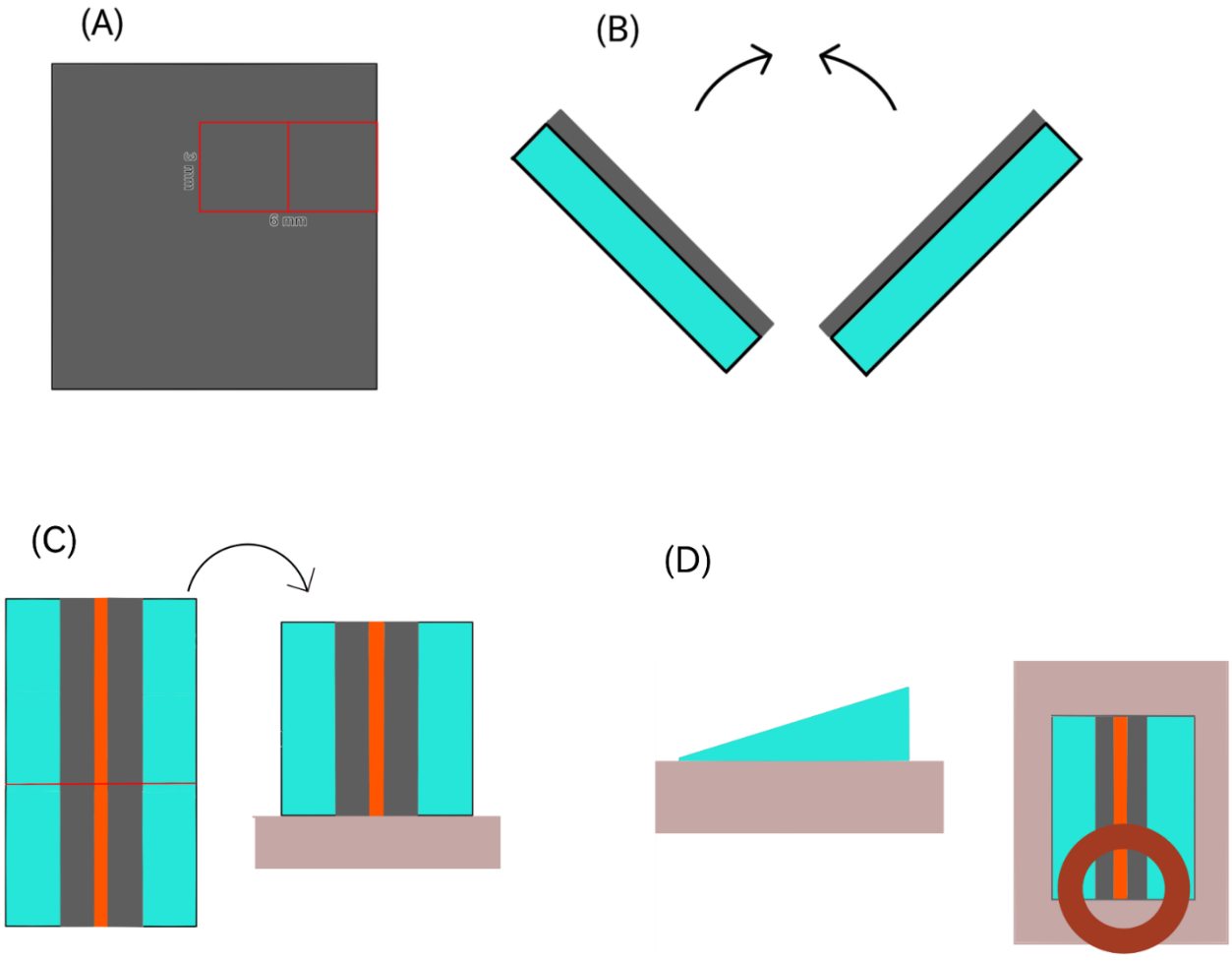


*Figure 31: The preparation of the TEM sample. (A) Observed sample, with an outline of area cut of. (B) The two pieces are added together with the deposited film directed towards each other, connected with glue. (D) the sample is cut in half, and one half is placed at a sample holder, were it thinned at an angle. (D) Thinned sample shown, the dark orange ring is the copper ring where the outside parts are cut off in a manner so that there is only the ring with the sample left. The sample is then thinned further using PIPS.*

## 4.3 Electrical measurements

Electrical measurements were conducted on thin films of the three materials used, ZnO, ZnO:Al and NiO:Li, in order to find the resistivity of the individual films. Electrical measurements were also conducted on the constructed BJT, to investigate in I-V characteristics of the junctions and the BJT.

### 4.3.1 Thin film resistivity

In order to measure the resistivity of the thin films, a van der Pauw 4-point Assembly setup was used by the help of a ProboStat™. A sketch of the ProboStat™ is given in Figure 34. The van der Pauw method uses 4 contact points on the sample to calculate an average resistivity of the sample. Two of the contacts are used to carry current between them, while the other two contacts measure the voltage drop in the sample, as shown in Figure 32. This is a two-step measurement, where the second step has altered which contacts the current and voltage is measured between. For example, the current goes between 2 and 3, and the voltage drop is measured between 1 and 4 in the first step (as in Figure 32), and in the second step the current travels between 1 and 2, and the voltage drop is measured between 3 and 4. This is done so the resistivity is measured in both the X- and Y-axis, to get a resistivity average of the sample.

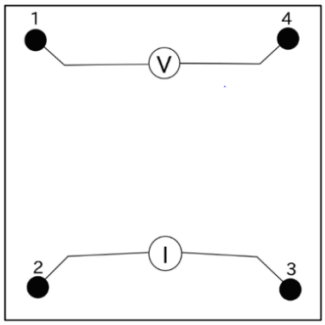


*Figure 32: Schematics of the electrode setup for a Van der Pauw 4-point measurement.*

In order to obtain the resistances, R, Ohms law is utilized,

$$R_1 = R_{12,34} = \frac{V_{34}}{I_{12}} \tag{36}$$

$$R_2 = R_{14,23} = \frac{V_{23}}{I_{14}} \tag{37}$$

Where V is the voltage and I is the current. However, this is only valid when the contacts are equally distanced from each other. In practice, it can be difficult to correctly place each contact. Therefore, the van der Pauw equation is introduced

$$exp\left(\frac{\pi dR_1}{\rho}\right) + exp\left(\frac{\pi dR_2}{\rho}\right) = 1 \quad (38)$$

, where *d* is the thickness of the sample and $\rho$ is the specific resistivity of the sample. If one knows the sample thickness one can obtain the specific resistivity. Further, one can find the conductivity as this is the inverse of the resistivity.

This method is good for samples of any shape, as long as the contact points are placed at the edges of the sample. The sample should also be dense and homogeneous, with a large surface to thickness ratio. The contact area of the electrodes on the sample should be as small as possible. An attached sample is shown in Figure 33.

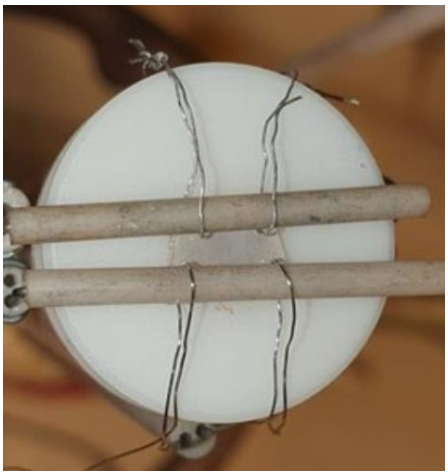

*Figure 33: Sample attached to the van der Pauw setup. The sample is a transparent film of ZnO, on top of a white alumina plate. The Pt electrodes are attached at the perimeter of the sample, with the help of spring loads of the ProboStat™.*

Samples were placed at the upper part of the ProboStat™. Four Pt electrodes were pressed in contact with the samples using spring loads, as seen from above in Figure 33. When the sample is assembled with the electrodes, the outer tube is placed over the sample in the ProboStat™ and is placed in an oven. Resistivity measurements can now be conducted with temperature variations.

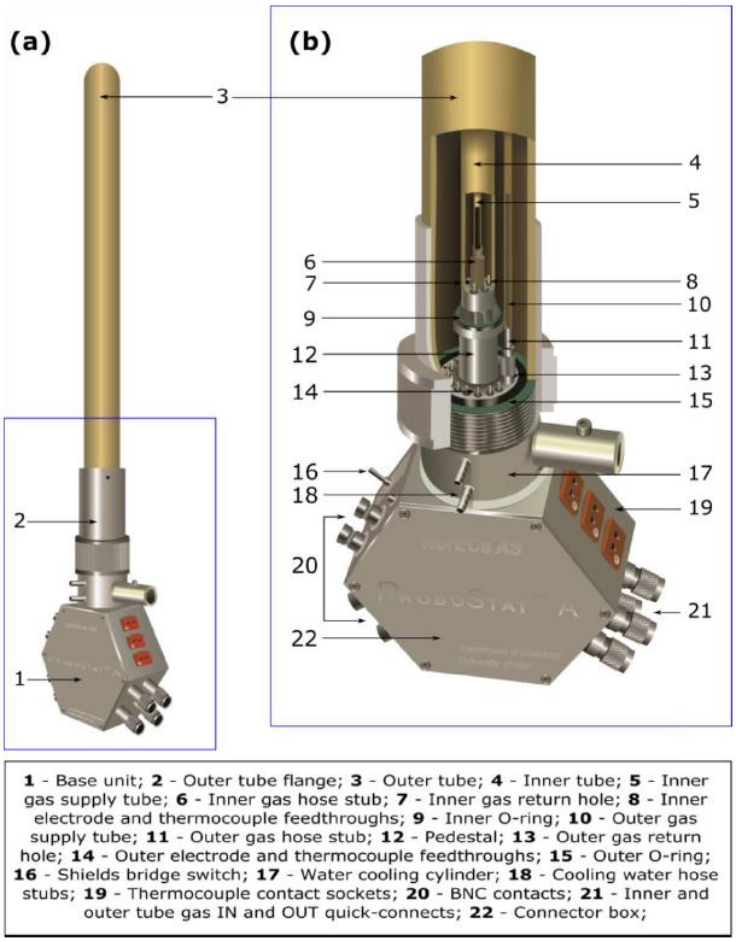


*Figure 34: (a) ProboStat™ measurement cell. (b) Inside view of the measurement cell, with an inner view of the cell. All main components are numbered in the Figure and listed under.*

### 4.3.2 BJT measurements

Because the BJT, and all other transistors, is built up of two back-to-back diodes, testing these diodes will give insight in the workings of the transistor. In order to see I-V characteristics of the two junctions in the BJT, the junctions of the BJT were connected into a circuit as shown in Figure 35. The diode symbol represents one p-n junction of the BJT. KEYSIGHT E3642A power supply was used as a power source, and an Agilent 34401A digital multimeter was used to read the voltage over the junctions while an amperemeter was used to read the current. In order to connect the BJT sample to the circuit, a LINKAM HFS600E-PB4 probe system was used. The Linkam system uses gold pins to connect with the base, emitter, and collector, as seen in Figure 36. However, as a gold contact would provide an unwanted Schottky contact with the NiO:Li base, Platina foil was wrapped around the gold pin in order to create an Ohmic contact with the base. I-V characteristics were produced by increasing the power-supply voltage and measuring the circuit current and the voltage over the junction.

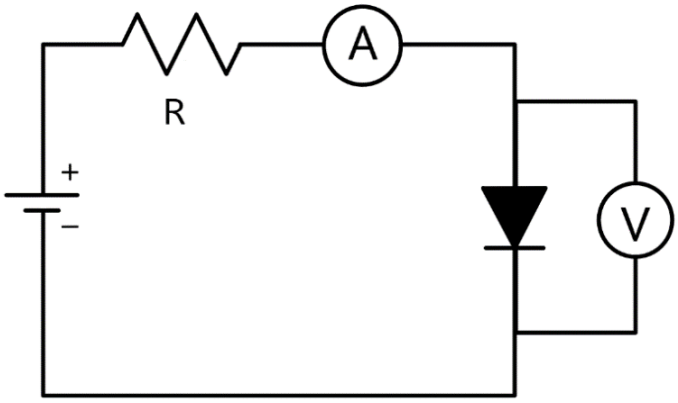


*Figure 35: Circuit for testing the p-n junctions in the BJT. R is a resistor inserted to protect the sample, V and A represents a voltmeter and ammeter, respectively.*

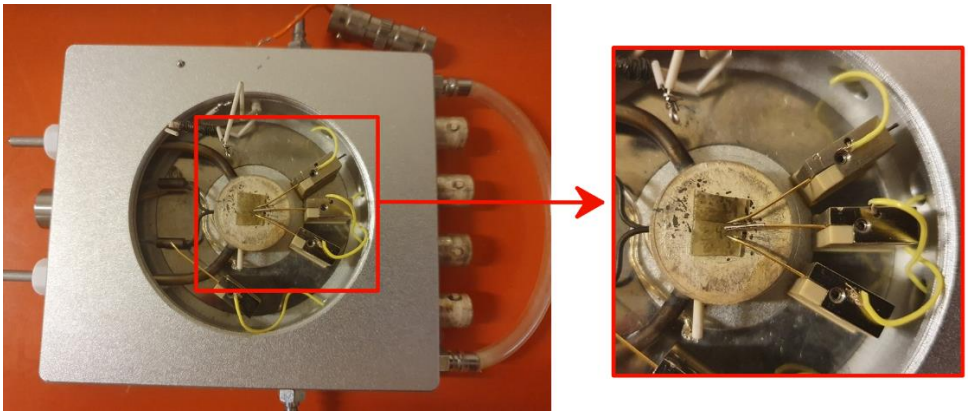

*Figure 36: Linkam probe system with an attached BJT sample. The gold pins of the LINKAM probe system is carefully connected to the contacts of the BJT. The gold pin connected to the base is wrapped tightly with Pt-foil in order to create a Schottky contact.*

In order to get output transistor characteristics of the constructed BJT, the BJT was integrated into a forward active mode circuit with common emitter configuration, a sketch is given in Figure 37. In order to provide constant base currents, $I_B$, a Gmary Reference 3000$^{TM}$ was used as a power source. A KEYSIGHT E3642A power supply was used to vary the supply voltage, Vcc. Output currents and voltages were measured with an Agilent 34401A multimeter. The BJT was connected to the circuit using the same Linkam system used when conducting junction measurements.

The variation of collector current, $I_c$, with the collector-emitter voltage, $V_{CE,}$ gives output characteristics for a fixed value of the base current, $I_B$. This measurement is repeated for several values of $I_B$.

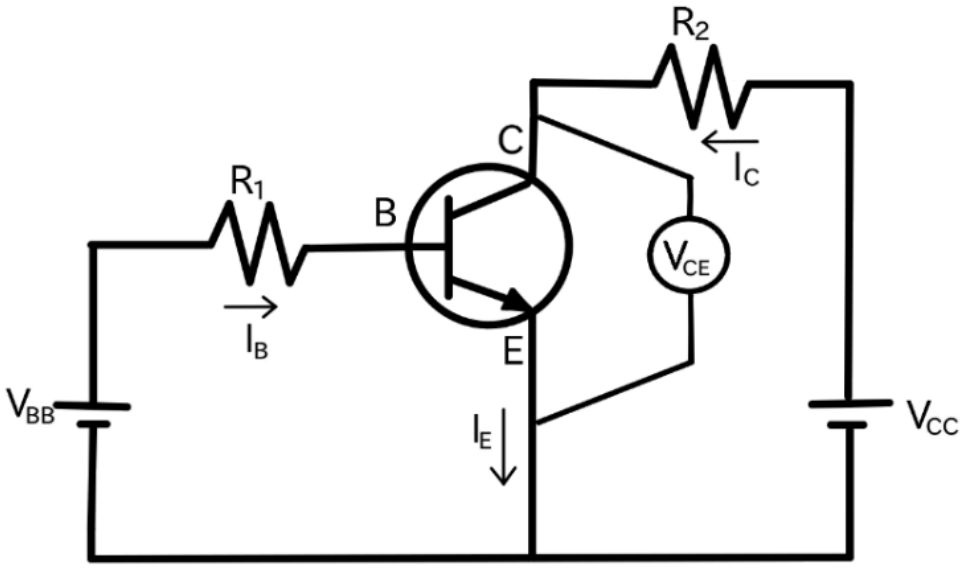


*Figure 37: Forward active mode circuit with common emitter configuration. The circuit shows the current flow direction. The resistances is there to protect the BJT*

## 4.4 Source of error and uncertainty

In the experimental methods presented and during the sample preparations presented here, there are numerous sources of error and uncertainties, and addressing them all is unrealistic. However, an effort in identifying as many as possible is essential to the understanding of the results that are to be presented. The common characterization methods of XRD and SEM also possess some sources of error and uncertainty that are well known, and will therefore not be discussed.

When preparing the target materials from powder to pellets, there is expected to be some unwanted impurities introduced during pellet preparation, which might have an effect on the final material properties.

As the PLD delivers material in the form of a plume, the intensity of the plume is expected to vary across the plume. This might affect the continuity of the final sample thickness, which might affect the material properties throughout the sample. However, the samples are relatively small, and one can, therefore, expect the sample thickness to be relatively similar throughout the sample.

When measuring the resistivity of the deposited films, and ZnO pellet, the Van der Pauw method desires a sample of constant thickness and for the electrodes to be equally distanced, with the contact point being much smaller than the sample surface area. The sample thickness was measured, but there is a possibility this thickness is not the exact thickness throughout the sample, as explained in the previous section. However, the deviation is expected to be small. Equally distancing the electrodes is executed to the best effort and considered well within reasonable expectations.

# 5 Results

Firstly, material composition is presented through the XRD results. In order to study the junctions of the transistor, cross-section pictures captured using SEM and TEM will be presented. Finally, electrical resistivity measurements conducted on the individual films, and I-V characteristics of the BJT is presented.

## 5.1 Sample characterization

### 5.1.1 XRD

In Figure 38, one can see the diffractogram of the PLD grown ZnO film. The XRD results suggest that the ZnO thin film was deposited with crystalline growth. The film is crystallized with a hexagonal structure with space group P63mc and a strong preferred orientation along the (002) plane, corresponding to the high-intensity peak which is located at 2θ = 34.71°. In addition, as can be seen in the inset of Figure 38, there is a low-intensity peak corresponding to the (004) plane, located at 2θ = 72.80. The strong peak located at 2θ = 41.79°, is the $Al_2O_3$ substrate. The high-intensity peak is quite narrow, and the full-width half maximum (FWHM) is found to be 0.089 with a crystallite size of 109 nm, hence exhibiting good crystallinity. These findings, including the small additional peak, match with other studies [73, 74]. It is to be noted, that for this particular deposition, the PLD plume was not great, which will have an influence on the thickness and structure of the film.

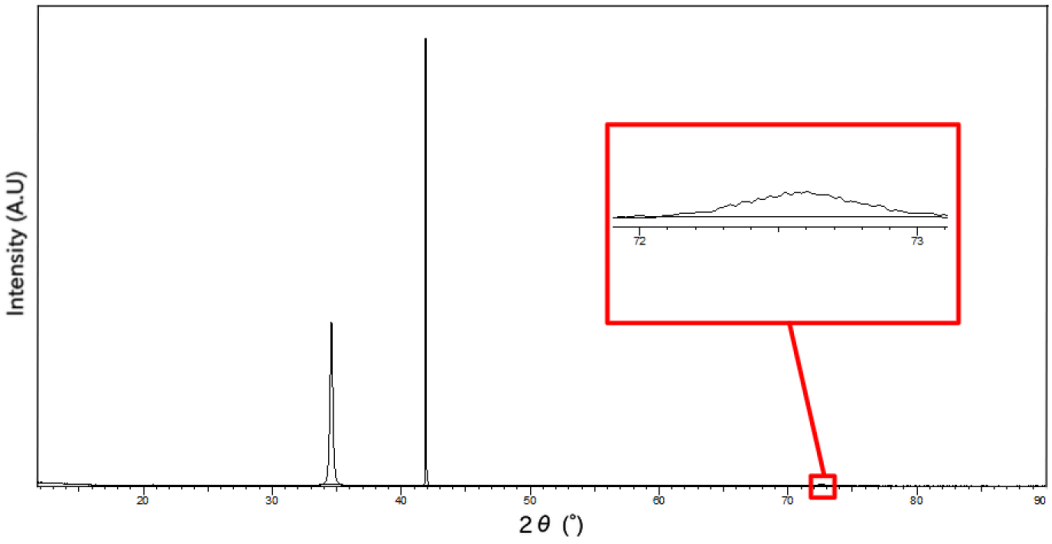


*Figure 38: Diffractogram of un-doped ZnO. A high-intensity peak is observed at 2ϑ = 34.71° and corresponds to the (002) plane. The inset shows a low-intensity peak at 2ϑ = 72.80, corresponding to the (004) plane.*

Diffractogram of a single layer of NiO:Li deposited by PLD on an $Al_2O_3$ substrate is presented in Figure 39. The NiO:Li film was found to have cubic crystal symmetry with space groups of *Fm-3m*. The intense peak located at 2θ = 36.67° corresponds to a strong preferred orientation

along the (111) crystal direction. The peak appears quite sharp, with some degree of broadening. The FWHM was found to be 0.363 and the crystallite size was 23 nm. Sources of peak broadening can be dislocations, micro-stresses, grain boundaries, and more, in this respect, it can be determined that the film is not flawless and contains some degree of unknown defects. In addition, a low-intensity peak is located at 2θ = 78.37°, corresponding to the (004) plane, seen in the inset to the right of Figure 39. These results of growth in the (111) plane resemble what other studies have also found [37].

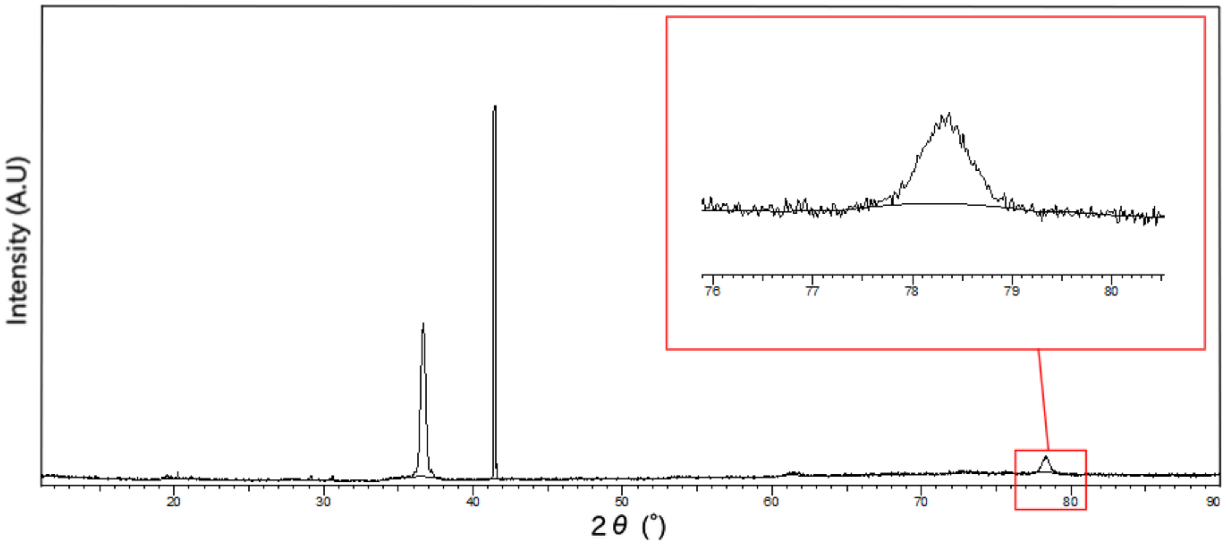


*Figure 39: Diffractogram of NiO:Li. The inset shows the peak at 2θ =36.67 and a low-intensity peak at 2θ = 78.37. The diffractogram shows the NiO:Li grows with a highly preferred direction along the (111) plane.*

Figure 40 shows the diffractogram of ZnO:Al. The diffractogram is, as expected, quite similar to the un-doped ZnO and forms a hexagonal structure with space group P63mc. The FWHM is found to be 0.193 and the crystallite size is 44 nm, suggesting that this film has good crystalline growth, but slightly degraded compared to the un-doped ZnO. The observed peak in this sample is more intense than the one observed in ZnO. The probable cause of this is the film thickness, as this film is thicker than the ZnO (because of the sub-optimal plume in the deposition of ZnO). The structure has the preferred direction (002) located at 2θ = 34.75°, this peak location is slightly shifted in comparison to the un-doped ZnO film. Taabouche et al. also finds this shift towards a higher 2θ angle, and attributed this to the decrease of the c lattice parameter [75]. As in the diffractogram of ZnO, there is a small, and broad, peak located at 2θ = 72.91°, seen in the inset of Figure 40. However, this peak corresponding to the (004) plane is more prominent in this aluminum-doped ZnO sample, which again can be explained by the increased thickness of this film.

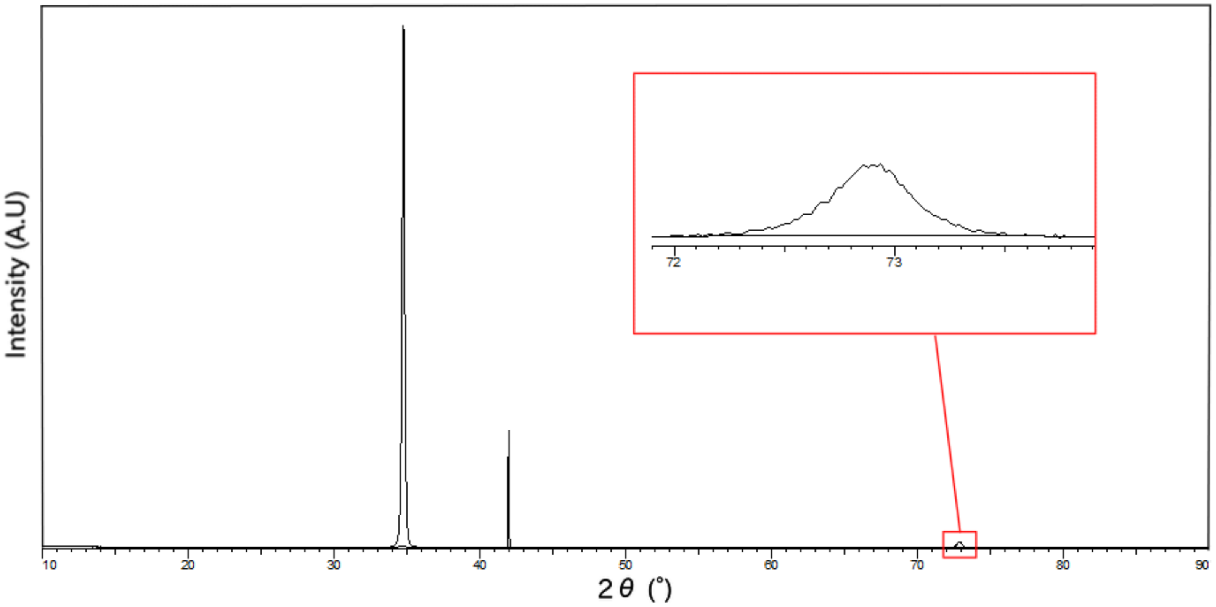


*Figure 40: Diffractogram of ZnO:Al, with a high-intensity peak located at 2ϑ = 34.75°. The inset shows a low-intensity peak at 2ϑ = 72.91. The peak indicates good crystal growth with the preferred direction along the (002) plane.*

The Diffractogram of the three-layered BJT is shown in Figure 41. One can see the most intense peak at 2θ = 34.40°, and one less intense peak at 34.65, which is quite similar to the peaks seen in the diffractogram for ZnO and ZnO:Al, which corresponds to the preferred (002) orientation. The HWFM and the crystallite sizes are approximated to be 0.184 and 0.212, and 46.5 nm and 39.9 nm for ZnO and ZnO:Al, respectively. Suggesting a relatively good crystallinity, but the multi-layering has seemed to degrade the quality to some extent. Some structural defects are expected in the layers, as there is some degree of broadening. Next to these two high-intensity peaks is a lower intensity peak located at 2θ = 36.36°, this peak resembles the peak seen at the diffractogram of NiO:Li, but with a small shift in position. The approximated FWHM is 0.39 and the crystallite size is found to be 21 nm. This suggests that the NiO:Li film is grown on ZnO, has the growth of crystallites with strong preferred orientation along the (111) plane, as there is no indication of growth in other planes. The not so crystalline or amorphous growth of NiO on ZnO is a common result in studies on this system [58, 76]. In addition to these peaks, there is another peak at 2θ = 72.3°, which is also seen in the diffractograms of ZnO and ZnO:Al, and corresponds to the (004) orientation. The additional peak observed for NiO:Li in Figure 39 is not found in this sample. It is observed that the peak broadening occurs with the decrease of crystallite size, which can be explained by the increased grain boundaries in the film, resulting in an increased scattering of the detected x-rays, hence creating a broader peak.

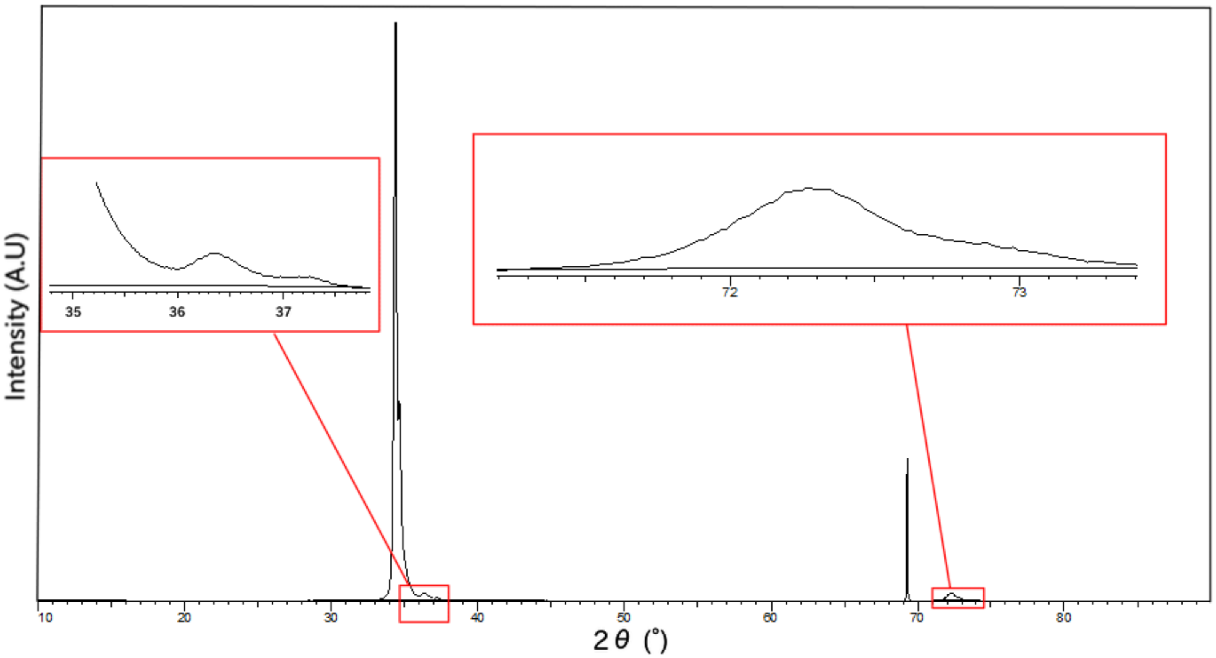


*Figure 41: Diffractogram of the three-layered BJT structure. There is seen two high-intensity peaks located 2ϑ = 34.40 and 2ϑ = 34.65, representing ZnO and ZnO:Al, respectively. Insets show a low-intensity peak at 2ϑ = 36.36, representing the NiO:Li layer, and another low-intensity peak at 72.3. ZnO and ZnO:Al show some broadening of the peaks compared to that of the single film layer growth. NiO:Li is grown on ZnO with low degree crystallinity, towards amorphous.*

### 5.1.2 Morphology and Microstructure

In order to see the cross-section of the BJT, the sample was cut vertically and mounted to an aluminum holder before being placed into the SEM. Three spots on the sample were investigated in order to look at the three deposited layers and their interface. Figure 42(A) shows the first layer of un-doped ZnO on top of the substrate. One can see that there are lines stretching up from the substrate, which suggests strongly oriented epitaxial film growth. The occurrence of epitaxial growth seems to be quite constant throughout the film. The film seems to be quite dense and uniform throughout the film, with a relatively smooth and flat surface. Figure 42(B) shows the surface of the film. There is an obvious crack formation on the surface, appearing quite frequently throughout the sample. The cracks don't seem to follow any pattern and appear with random orientation throughout the film surface. When looking at the cross-section (A), there are no signs of crack-formation from the surface down into the sample, indicating that these crack-formations at the surface might not penetrate far into the film. Similar crack-formation have been reported by Xu et al., which suggested these cracks appear over time after high-temperature deposition, because of exposure to ambient air [77]. They also found that crack-formation increases with higher temperatures. Despite the cracks, the surface (B) shows dense and continuous hilly grain formation throughout the film surface. However, some deviation of this uniformity is spotted, as seen in the lower left part of Figure 42(B).

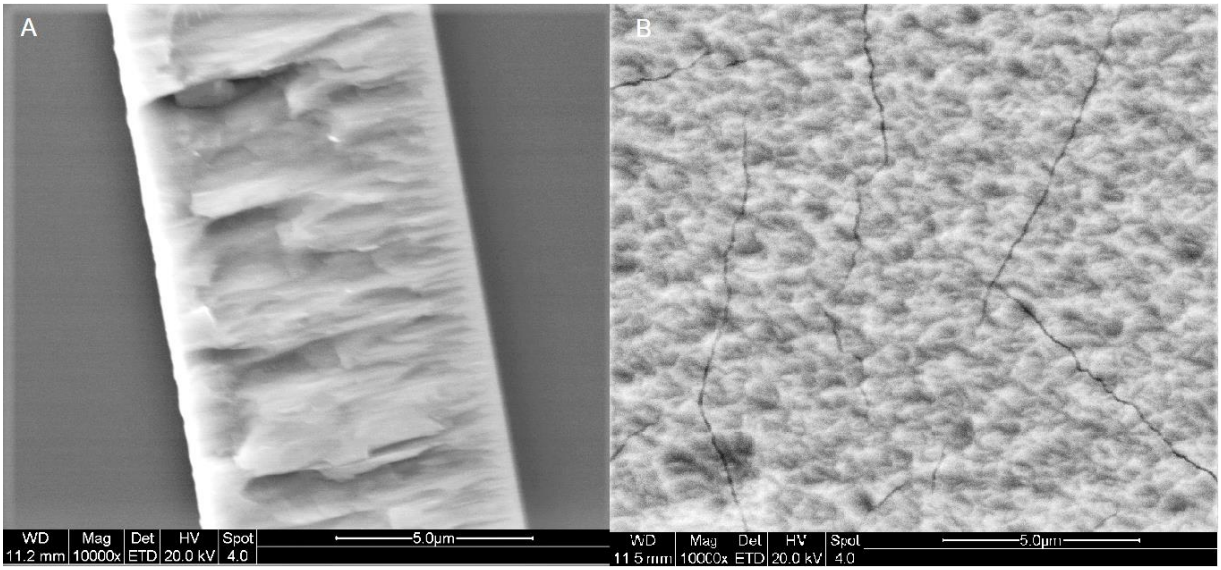


*Figure 42: (A) cross-section ZnO grown with PLD at a substrate temperature of 400 °C, showing good columnar growth perpendicular to the substrate. (B) The surface of the same sample, showing cracks along the surface with random orientation.*

In Figure 43, the second layer of NiO:Li, grown on top of the first layer of ZnO, is shown. It is obvious that there has been deposited a second layer on top of ZnO, with a thickness of about 1 µm. NiO:Li seems to have grown a dense and uniform film with a relatively smooth surface. The interface between the ZnO and NiO:Li looks relatively sharp, with good adhesion between the layers. Along the cross-section surface, there is seen some degree of surface roughness. Also, some spots along the interface seem to have broken the smooth interface. At these spots, it can look like the NiO:Li penetrates into the previously grown ZnO. However, these can be a result of the cross-sectional cut creating grooves along with the film layers, and these grooves create lines between the layers forming an illusion of NiO:Li penetrating into ZnO. A surface SEM-picture is shown in Figure 43(B), the surface shows homogeneously distributed grains of NiO:Li. There are no clear indications of cracks on this surface. However, this surface shows a rougher surface compared to that of ZnO. Fasaki et al. found that with an increase of the substrate temperature, the surface roughness will increase[70]. This was attributed to the tendency of the atoms at lower substrate temperatures to crystallize at planes with the lower energy, creating the rough surface.

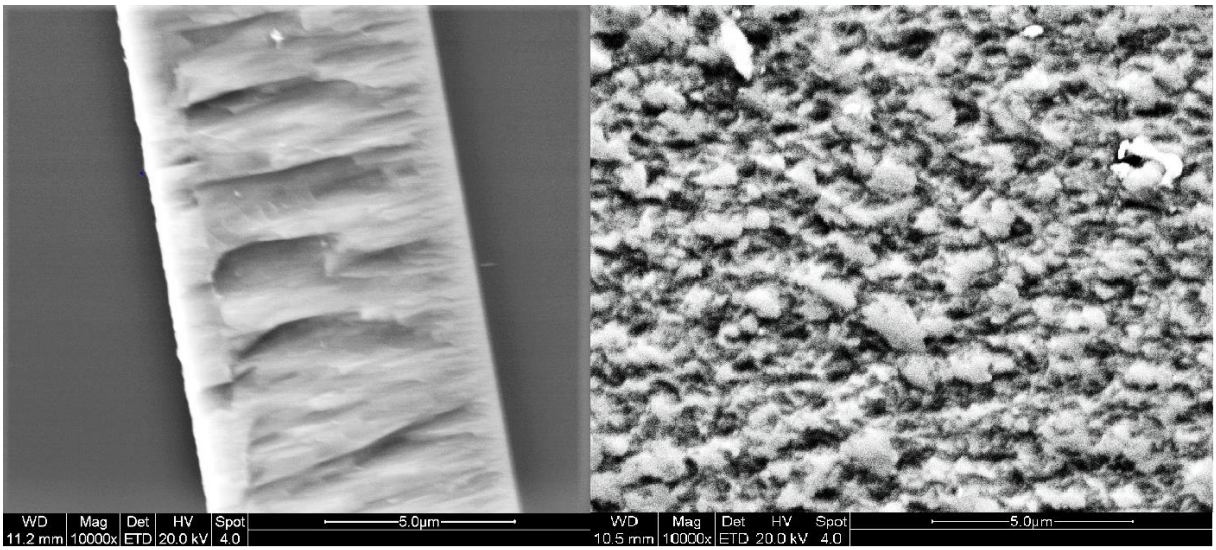


*Figure 43: SEM picture of NiO:Li grown on top of ZnO. The interface is sharp with good adhesion. However, the surface shows a relatively high degree of surface roughness.*

Figure 44 shows the final layer of ZnO:Al on top of NiO:Li and ZnO, from the left in the Figure, respectively. This ZnO:Al layer completes the bipolar junction transistor, and one can clearly see three distinct layers throughout the sample. This last layer, like the others, seems to have grown dense and uniformly throughout the film, ending with a thickness of about 1.5 µm and a relatively smooth surface. Also in this interface between ZnO:Al and NiO:Li, as in the interface between NiO:Li and ZnO, there seems to be a relatively sharp interface without any forms of pores or cracks. Looking closely at the lines along with the films, one can see columnar growth of all the layers, perpendicular to the substrate. In Figure 44 (B), the surface of the final ZnO:Al layer of the BJT is shown. The surface appears rougher than the ZnO surface. Zhao et al. found that the change in surface roughness with substrate growth temperature is quite small up to a temperature of 400 ℃, and increasing hereafter. The rough surface, in contrast to the ZnO surface, might be initiated by the rougher underlying layer surface of NiO:Li. There is no cracking formation, like that of ZnO, seen on this surface. Nevertheless, the surface showed a continuous layering throughout the surface, without the surface cracking seen in ZnO.

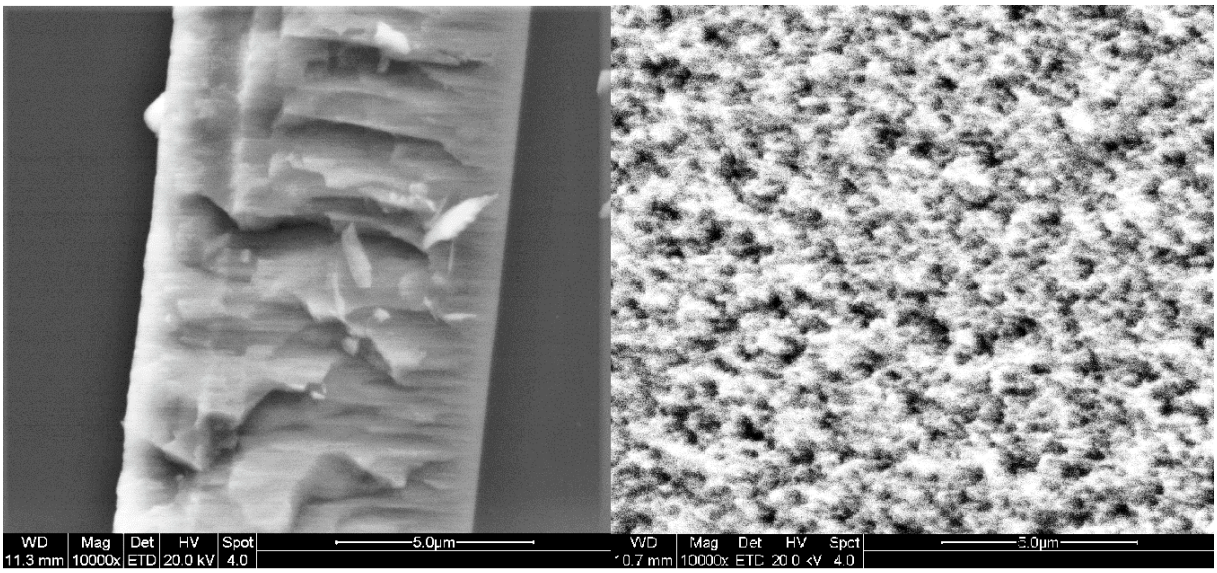


*Figure 44: SEM cross-section picture of three-layered BJT grown with PLD. Layered from the right; ZnO, NiO:Li and ZnO:Al. The construction of a three-layered structure has succeded. The surface roughness of ZnO:Al is somewhat higher than that of ZnO.*

Upon further investigation of the three-layered structure in the SEM, the presence of areas with indications of inconsistent layering is evident. Figure 45 (A), which is captured about 20 um from Figure 44 (A), shows the inconsistency of the layering. There seem to be some areas where the layers penetrate each other. These spots of interface penetration seem to be most prominent for NiO:Li into the ZnO layer. However, as mentioned, these can be a result of the cross-sectional cut creating grooves along with the film layers, forming the illusion of this layer piercing. In Figure 45 (B), (C), and (D), surface images of holes in the films of ZnO, NiO:Li and ZnO:Al, respectively, captured in the BJT sample is shown. More of these holes were found throughout the surface of the sample. Also to be noted, when handling the samples in general, the observation of the films being fragile has been made. In an effort to polish the samples for a better cross-section view, without groves, resulting in flaking of the layers in the sample.

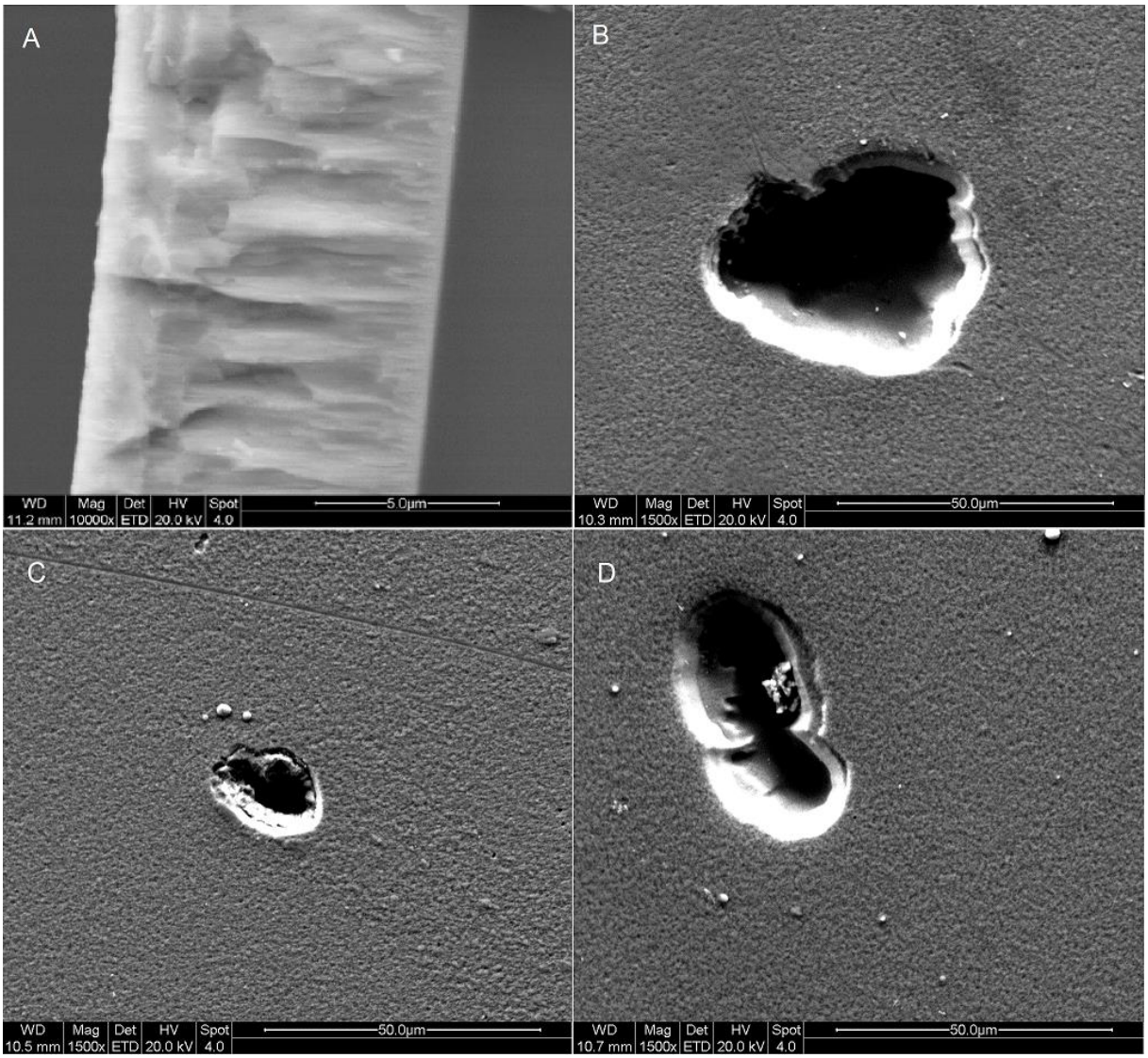


*Figure 45: SEM cross-section picture of three-layered BJT grown with PLD. Spots of interface "breaking" are seen along with the interfaces. Surface holes in all the layers are appearing throughout the surface.*

In an effort to investigate the junction between the ZnO:Al and NiO:Li, transmission electron microscopy (TEM) was utilized. The sample observed is a PLD deposited layered structure of ZnO:Al (bottom) and NiO:Li (top) deposited on an $Al_2O_3$ substrate. It is to be noted, when this sample was made, the PLD experienced trouble in delivering laser energy, which resulted in a much thinner sample than that of the BJT. Figure 46 (a) shows an overview of the observed area. Figure 46 (b) shows the substrate at the thinnest part of the sample. The small white spots in the image are the locational sites for where EDX measurements were captured, which confirmed the presence of Al and O. Figure 46 (c) shows, to the lower right side, the deposited films (black line) on top of the substrate. The upper left part of the image depicts the glue, with a gap between the deposited thin film and the sample preparation glue. The large black particle seen in the upper right side of the image, also seen along the glue line in the overview image of figure 46 (a), has been determined to be a copper deposition. This copper particle is deposited on the sample during the TEM sample procedure, caused by the precision ion

polishing system (PIPS) partially hitting the copper ring. Figure 46 (d) shows a close up of the layered structure, with the substrate covering the lower right side of the image. An enlarged figure of this is seen in Figure 47.

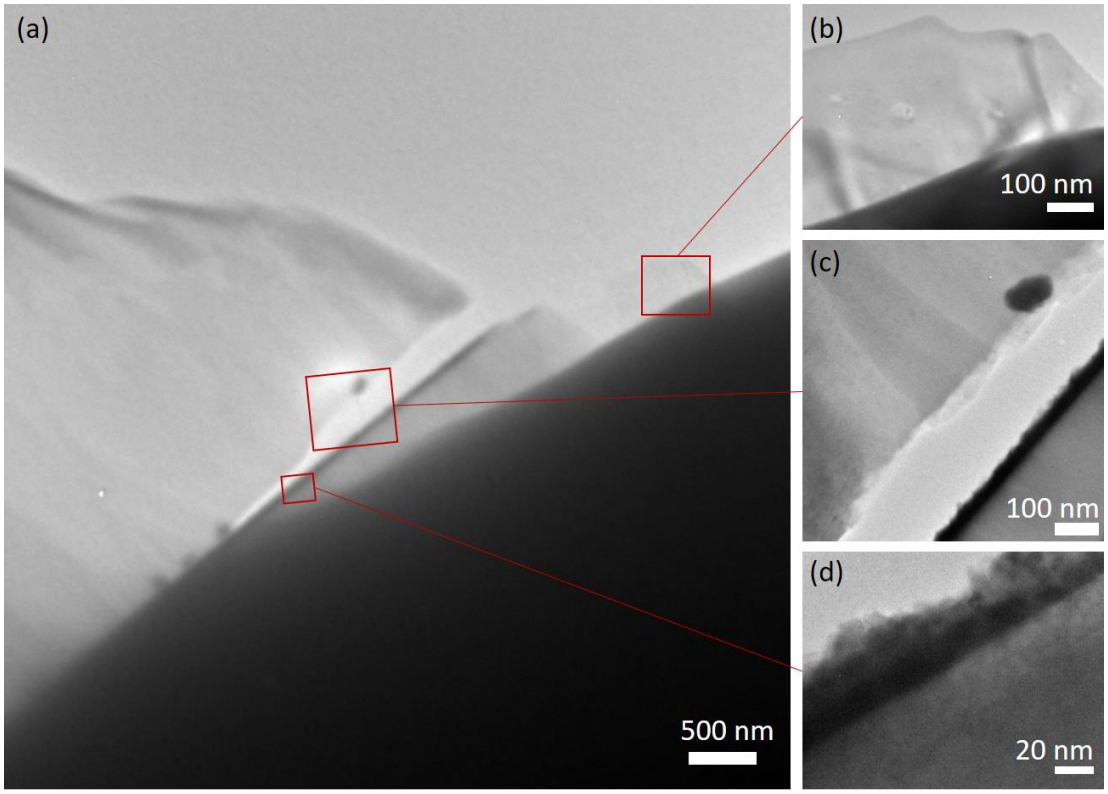


*Figure 46: (a) The bright-field image shows an overview of the observed area. The substrate is located in the lower right corner with a thin film on top, followed by glue. (b)The substrate at the thinnest part of the sample. Multiple EDX measurements (white spots) confirmed the presence of Al and O. (c) The lower right side shows the substrate with thin films on top. The upper left corner depicts the glue, with a gap between the thin film and glue. The large black particle has been determined to be a copper deposition caused by the precision ion polishing system (PIPS) partially hitting the copper ring. (d) Close-up of the layered structure, EDX confirms the presence of Zn, Ni, O, and Al, Li is not detected. Although the glue line is eradicated, observations confirm that areas covered with glue suffer the same uneven thin film.*

In Figure 47, an enlarged version of Figure 46 (d) TEM image is shown. It is hard to tell a distinct boundary between the layers, with the exception of the substrate and the first layer. However, the bottom part of the film appears darker than the upper part, which is an indication that the image is in fact showing two films deposited. This is also supported by the fact that Zn is a slightly heavier element than Ni, and would, therefore, appear darker in TEM-imaging, as the ejected beam more easily can transmit through lighter areas of the sample. In that respect, NiO:Li and the overlaying ZnO:Al is lacking continuity of the film layer thickness. However, in areas where the underlying ZnO:Al layer seems to have been deposited evenly, the interface between the two layers is shown to be sharp. Also, Due to no presence of glue on top of the sample in this section, there is no guarantee that the sample is without damage (most likely some edges are off). However, sections, where the glue was present, looked the same, with the only difference being that this is a thinner section, hence allowing more details in the picture.

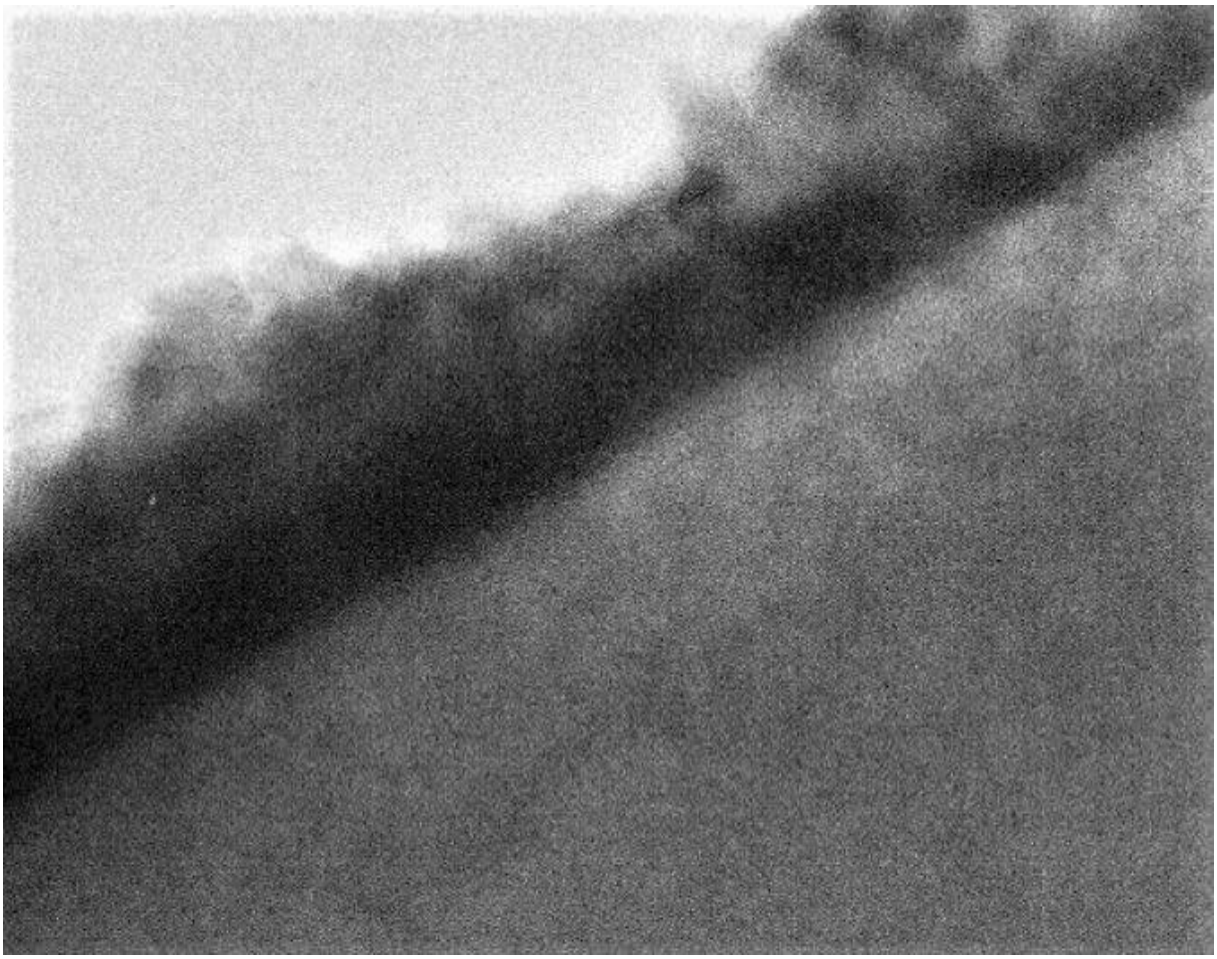

*Figure 47: A close-up of Figure 46 (d), showing the deposited films of ZnO:Al (bottom) and NiO:Li (top). The interface between the layers seem to be very sharp.*

In order to distinguish which elements are present in the sample, and in the layers, EDS-imaging was utilized. Figure 48 shows (A) cross-sectional SEM image of the area in the BJT sample where EDS mapping was employed. Figure 48 (B) shows the mapping of Zn in the sample. Evidently, Zn is detected in the sample and is detected throughout the sample. In the upper part of the image, there can be seen a line of lesser Zn density, which is matching with the Ni mapping seen in Figure 48 (C). Clearly, there are distinct areas where the elements are detected, confirming the deposition of a three-layered structure. In Figure 48 (D) the mapping of Al is shown. The mapping shows Al detected throughout the sample, and further out of the sample. This is because of the sample holder, which is made of aluminum. Therefore, one can not rely on the mapping of Al here. From these images, it can look like both Zn and Ni are spread throughout the cross-section of the sample, as if they have diffused into each other. However, the EDS accuracy at this scale is debatable.

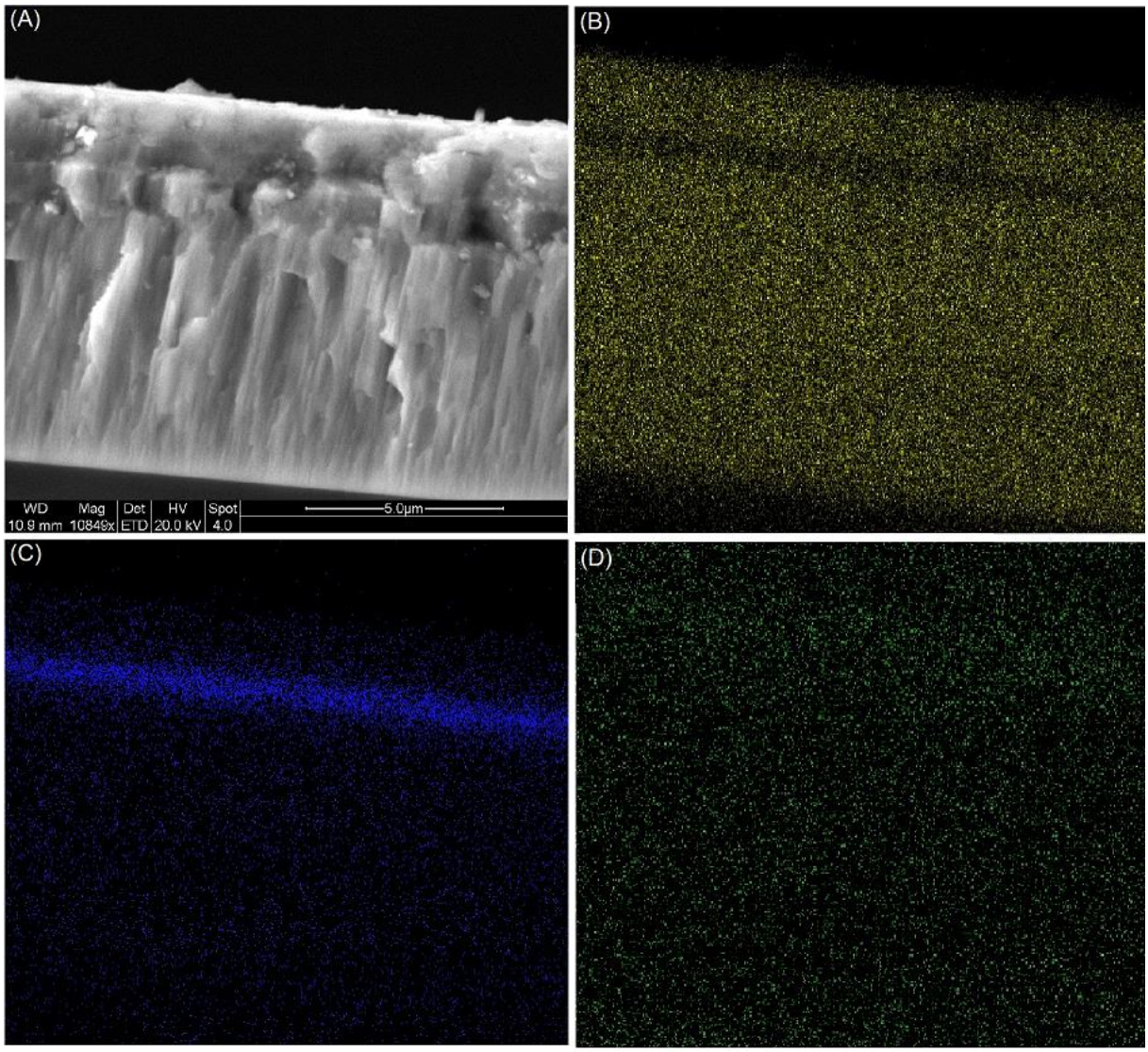


*Figure 48: (A) SEM image of the area mapped with EDS, a cross section of the BJT sample. (B) Zn mapping of the area, showing Zn all over, with a lesser density along the line of Ni. (C) Mapping of Ni in the sample, showing a strong density line. (D) Mapping of Al in the sample, this is not reliable as the sample holder is made of Al.*

## 5.2 Electrical measurements

### 5.2.1 Resistivity of thin films

The electrical resistivity of thin films made from ZnO, ZnO:Al and NiO:Li was measured as a function of temperature, in the range of 25 C to 600 °C, with a Van der Pauw 4-point setup in ambient air. In Figure 49, one can see how NiO:Al react to the temperature change from room temperature to 600 C°. Initially, the resistivity increases up to a point of 300 °C with over three orders of magnitude, then the resistivity decreases again. When going back down in temperature, the resistivity follows the same path as when the temperature increases. In literature, this type of resistivity dependence on temperature is not reported. The resistivity of NiO is reported to gradually decrease as a function of temperature [78, 79].

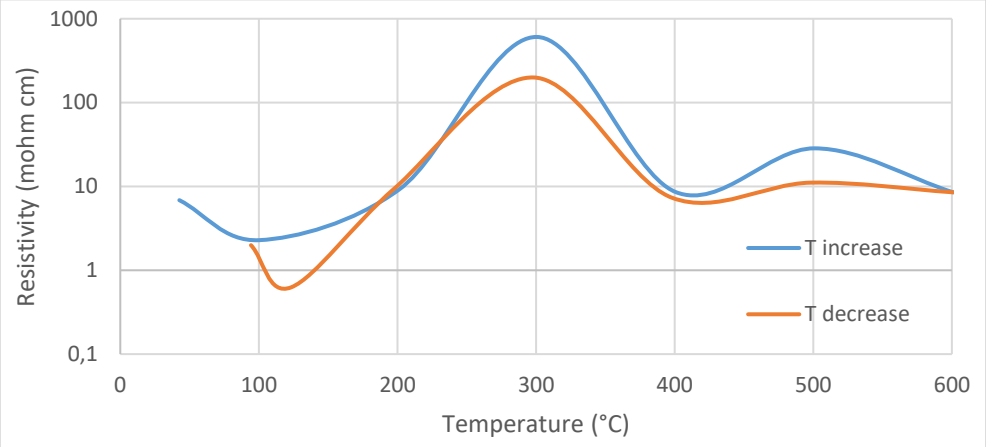


*Figure 49: Electrical resistivity of NiO:Li as a function of temperature. This temperature dependency of the resistivity is not found elsewhere in the literature.*

In Figure 50 one can see resistivity measurement of ZnO:Al in the range of room temperature to 600 °C. From room temperature to about 300 °C, the resistivity remains quite constant with a resistivity of about 7 to 8 mohm cm. After 300 °C, there is a spike in resistivity up to 600 °C. When decreasing the temperature, the resistivity follows the same pattern as to when increasing, but with higher resistivity. This resistivity dependence on temperature is not in agreement with other studies, which finds that the resistivity decreases with the increase of temperature [80, 81].

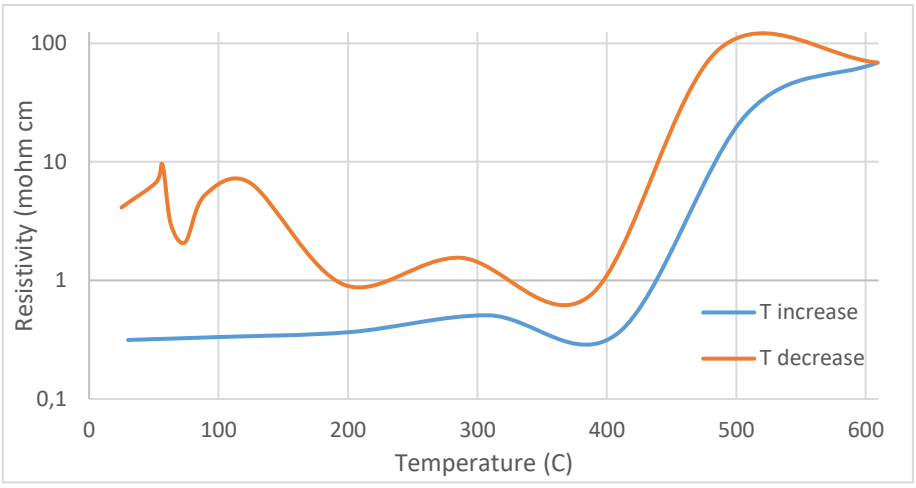


*Figure 50: Plot of resistivity with respect to temperature for ZnO:Al. Showing strange characteristics not common for sa emiconducting material.*

Figure 51 shows the temperature dependency of resistivity for un-doped ZnO. Also here, the tendency is an increase of resistivity with temperature. The resistivity of semiconductors is expected to decrease with the increase of temperature, as explained in section 2.2.3. This is because when the temperature rises in a semiconductor, the electrons within the valance band gain enough energy to escape the valance band and act as free electrons, hence increasing the electrical conductivity. Also, following eq. 5 and 13, it is expected that the concentration of electron holes and electrons, respectively, will increase, hence also increasing the conductivity of the sample. When temperature increases in a conductor, the increased vibration of the ions in the lattice causes an increase of collisions between free electrons and other electrons, depleting them for energy and thus increasing electrical resistivity with temperature. A study by Amit et al. shows how ZnO goes from a semiconducting behavior towards a metallic behavior with the increased doping concentration of aluminum [80]. They found that films with a doping concentration of $x > 0.5$ in $Zn_{1-x}Al_xO$ will show metallic behavior.

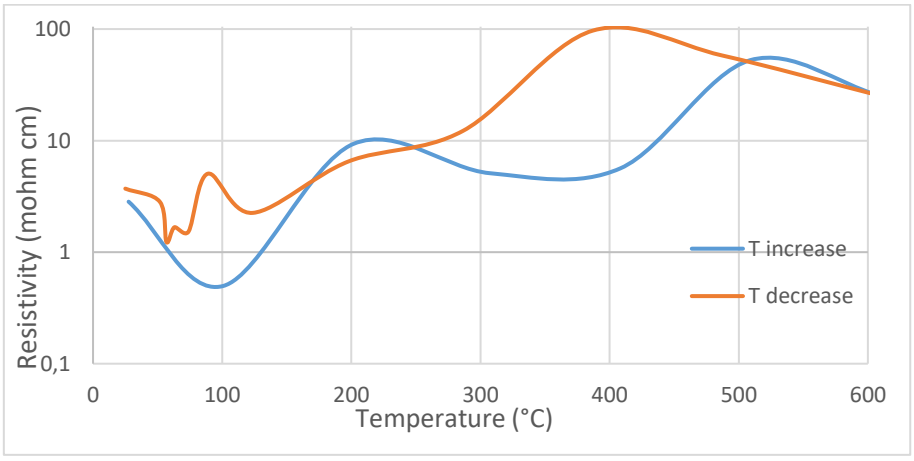


*Figure 51: Electrical resistivity of ZnO as a function of temperature. Showing an increase in resistivity by the increase of temperature. In deviation from literature and theory*

The deviation from the literature and theory of these resistivity measurements creates an uncertainty of the reliability of the results. Setup flaws or mistakes might have caused instability of the measurement, consequently creating inaccurate results.

### 5.2.2 BJT

The BJT sample was incorporated into a circuit as illustrated in Figure 37. With a constant current delivered to the base, the collector current, $I_C$, and voltage from emitter to collector, $V_{CE}$, was measured when applying input voltage, $V_{cc}$, of 0 – 3 V. The ensuing results are given in Figure 52. From the I-V curve one can see that the $I_C$ grows proportionately with the increase in $V_{CE}$, equally for all the constant currents up to a voltage of about 1.0 V. From this point on the lines spread out in the graph, with $I_B$ = 1000 $\mu$A gaining the most current, closely followed by $I_B$ = 100 $\mu$A, $I_B$ = 10 $\mu$A, and $I_B$ = 0.1 $\mu$A, respectively. All gaining current was relatively proportional to the increase of $V_{CE}$. This does not resemble the normal output characteristics of a transistor, evidently showing that the construction of a functional BJT has not succeeded. However, the initial similarities in the output characteristics of the different $I_B$ currents are of interest, as they follow the same initial curve until splitting at approximately the same applied voltage.

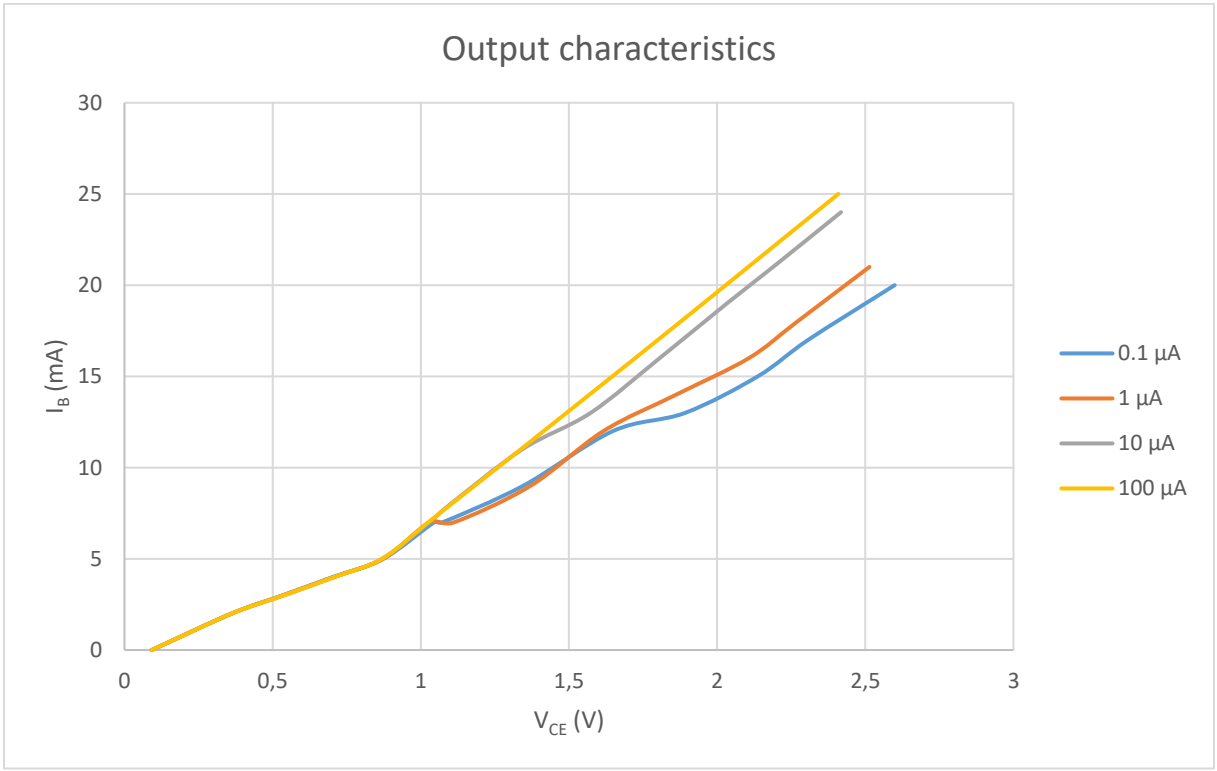


*Figure 52: I-V characteristics of the BJT at different input current of; 0.1 $\mu A$, 1 $\mu A$, 10 $\mu A$ and 100 $\mu A$. The BJT is not showing a resemblance to what one would expect from a functioning transistor.*

In an effort to identify the underlying reason for the non-transistor-like behavior, electrical measurements were conducted on the two junctions of the BJT, the base-emitter junction (NiO:Li-ZnO:Al) and the base-collector junction (NiO:Li-ZnO). The junctions were set up in the circuit explained in section 4.3.2, In order to look for diode behavior.

In Figure 53, I-V characteristics of the NiO:Li-ZnO:Al junction is presented. The graph shows an almost linear relationship between the applied voltage and the current measured, hence resembling Ohmic behavior. This is not wanted, as the junction should act like a diode and show rectifying behavior. The current is passing through the junction freely, without needing to overcome any form of barrier. Evidently, this shows that the fabrication has not reached the desired characteristics of the p-n junction between the NiO:Li and ZnO:Al, hence also giving an answer to why the BJT did not show characteristic transistor behavior.

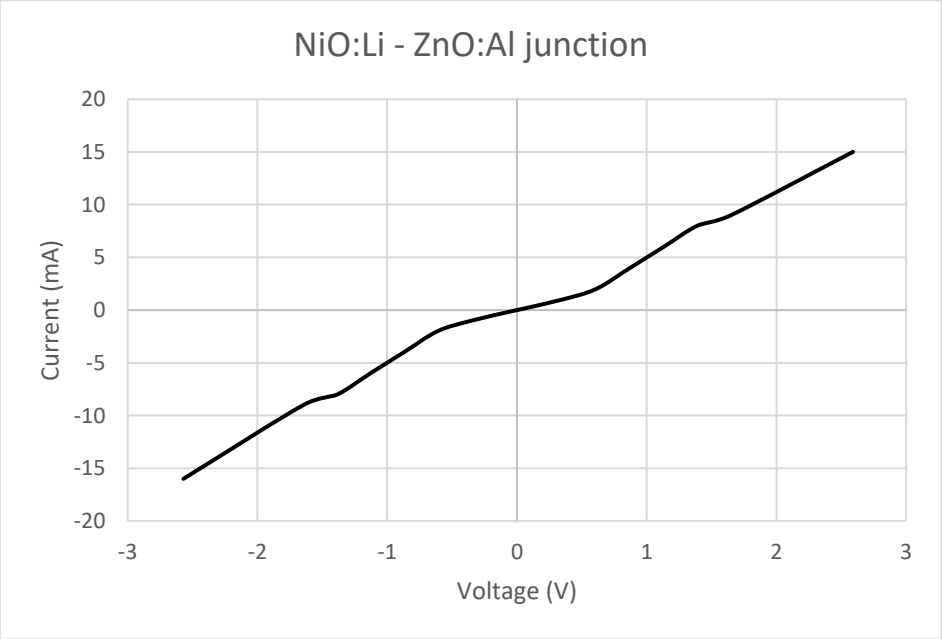


*Figure 53: I-V characteristics of the NiO:Li-ZnO:Al junction (BE). Showing ohmic behavior, not resembling a diode.*

In Figure 54, I-V characteristics of the NiO:Li-ZnO:Al junction is presented. The junction showing I-V characteristics of rectifying behavior, in contrast to the NiO:Li-ZnO:Al junction. This rectifying behavior confirms that there has been a successful fabrication of a p-n junction, as this resembles a working diode. One can see that the forward voltage exceeds the junctions internal barrier voltage at an applied voltage of about 1.8 V and that the breakdown voltage starts at -0.84 V. The forward biased characteristics seen in this p-n junction, is also reported in other studies on the NiO-ZnO system [37, 82]. The relatively low value of the breakdown voltage is also reported in the literature [55, 83]. however, not in combination After the barrier voltage has been breached, there is a linear increase in current, in contrast to most diodes experiencing an exponential current gain after this point. However, this is also seen elsewhere in the literature[84].

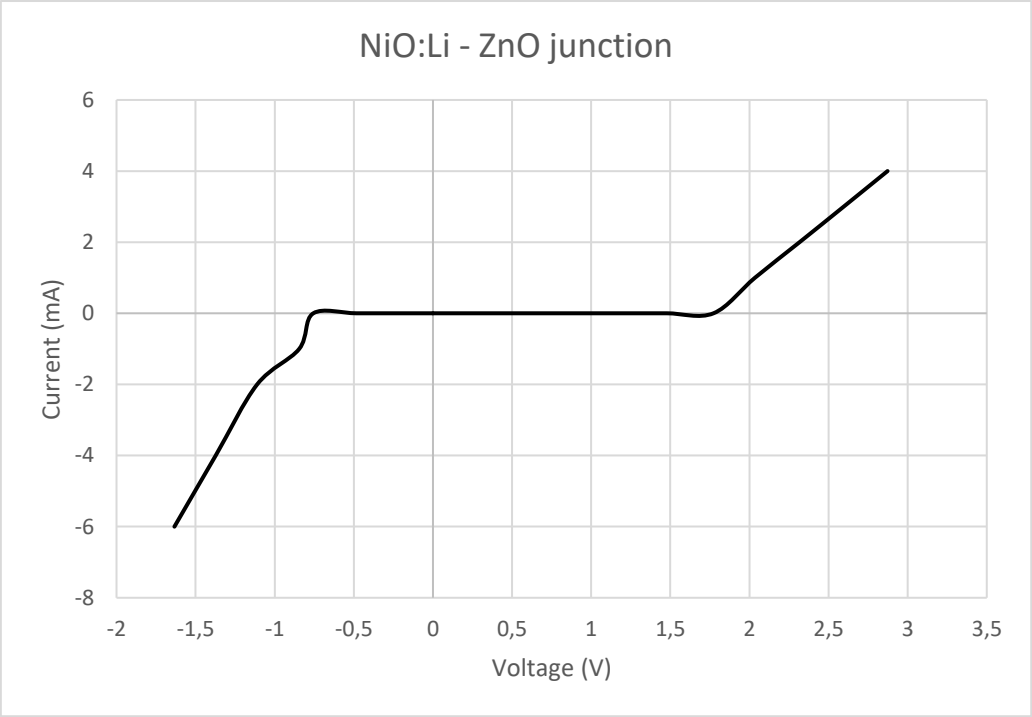


*Figure 54: I-V characteristics of the NiO:Li-ZnO junction (CB). This curve shows there is diode behavior in the NiO:Li-ZnO junction.*

It is to be noticed that these measurements where conducted on diodes as a part of the BJT, the extra third (e.g. ZnO in the case of NiO:Li-ZnO:Al measurement) component might have an influence on the measurements conducted. However, these influences are expected not to have a great impact. In an effort to test the p-n junctions at higher temperatures on another test day, the resulting diode characteristics of the junction had disappeared. It seems like the junctions somehow had lost their rectifying behavior. If this is caused by mishandling of the sample or some form of structural decay in the days in-between is unknown. Xu et al. (surface cracks) suggested that the exposure of ZnO to ambient air after high-temperature deposition will cause defects in the film surface over time, and in order to avoid this one should cover the surface[77]. However, no explanation as to what is happening to the film, or further investigation was made.

# 6 Discussion

In this chapter, the findings of this thesis are interpreted and discussed, in order to support statements made and the final conclusion. Firstly, the results from chapter 5 are further discussed and related to literature. Then, these discussions are then to be summarized and discussed in its entirety.

**Fabrication and characterization**

Firstly, the XRD results from chapter 4 confirm we can grow thin films of the materials. Figure 41 strongly suggests the growth of ZnO, NiO:Li and ZnO:Al, respectively, with their preferred plane orientations. For both ZnO and ZnO:Al, there are high-intensity peaks indicating crystalline film growth with strong preferred orientation in the (111) plane, which is in agreement with other studies [60][61]. For both ZnO and ZnO:Al, there are also some indications of growth in the (004) plane, with a more intense peak for ZnO:Al, compared to ZnO. A probable cause for the higher intensity peak in the ZnO:Al film, is simply that the thicker film of ZnO:Al reflects more x-rays than the ZnO film. The low-intensity peak at 2θ = 72.80°, alongside the high-intensity peak at 2θ = 34.71° for ZnO and ZnO:Al is also observed by Taabouche and colleagues[75]. They also observed that increasing the Al doping concentration will cause a decrease in (002) peak intensity, which is found in other studies as well [75, 85]. The diffractogram of NiO:Li shows a high-intensity peak at 2θ = 36.67°, which corresponds to the (111) plane. Compared to the diffractograms of ZnO and ZnO:Li, this peak is much broader, indicating less crystalline growth. In addition, as for ZnO and ZnO:Al, a second peak indicating growth in another plane direction is observed. This is a low-intensity peak located at 2θ = 78.37° and corresponds to the (004) plane. This peak is also seen in other studies, but as the intensity of this peak is rather low, the peak is generally neglected [37, 86]. This can also be said for the additional peaks seen for ZnO and ZnO:Al, the peaks are of relatively low intensity compared to the preferred orientation peak, that they can be neglected to have a significant impact on the overall material behavior. In respect of these findings, PLD is shown to be a good method for the fabrication of these materials.

The diffractogram of the three-layered BJT shows all the peaks found in the diffractograms of ZnO, ZnO:Al and NiO:Li, with the exception of the additional peak, found for NiO:Li, sown in the inset of Figure 39. The most high-intensity peak is located at 2θ = 34.36°. Another high-intensity peak is located with a slightly higher angle located at 2θ = 34.65°. It is hard to exactly determine which peak correspond to what layer, but knowing from Figure 44 that the film thickness of ZnO and ZnO:Al are approximately 7 µm and 2 µm, respectively, one can expect that the most high-intensity peak located at 2θ = 34.36° represents the ZnO layer and the peak located at 2θ = 34.65° represents ZnO:Al, as film thickness effect peak intensity. Nakrela et al. found in their study that an increase in aluminum doping of ZnO would shift the peak towards a higher value of 2θ, which would further support the higher 2θ peak representing ZnO:Al and the lover value 2θ peak representing ZnO [85]. The two sharp peaks are of high-intensity, suggesting crystalline growth for both doped and un-doped ZnO, strongly oriented along the (002) plane. With the FWHM values of 0.184 and 0.212 and the corresponding crystallite sizes

of 36.5 nm and 39.9 nm for ZnO and ZnO:Al, respectively, there is expected to be some degree of broadening of the peak, since the small crystallites increase the grain boundaries in the sample. Next to these high-intensity peaks, is a broader low-intensity peak which corresponds to the NiO:Li film growing in the (111) plane. This peak being of low-intensity and broader compared to the two peaks of ZnO and ZnO:Al is expected, as high crystallographic growth of NiO on ZnO has been proven difficult through other studies, as mentioned in chapter 3.6.2 [55]. However, the peak confirms the growth of NiO:Li with preferred orientation along the (111) plane The FWHM of this peak is 0.39 with the corresponding crystallite size of 21 nm. The additional peak observed in ZnO and ZnO:Al is also present in this sample, located at $2\theta = 69.34°$. However, The additional peak found for NiO:Li in the inset of figure 39, is not found in this sample.

From the cross-sectional SEM images, it is evident that the pulsed laser deposition of a three-layered BJT is successful. One can clearly see lines in the ZnO layer stretching perpendicularly from the substrate, indicating columnar growth normal to the substrate. This is a common growth process for ZnO and observed in other studies [42, 86]. The NiO:Li layer seems to have been deposited with good adhesion to the ZnO film and without any clear indications of crack or pore formation. However, the surface of the NiO:Li layer shows a rougher surface compared to the surface of ZnO. A rougher surface is less convenient in the construction of a sharp p-n junction, and this might lead to degraded adhesion between the layers and result in unwanted interface defects effectively reducing the interface are between NiO:Li and added ZnO:Al layer. However, as mentioned, there is not seen any pores or cracks confirming this. The top ZnO:Al layer in the BJT also show a dense film without notable signs of pores and cracks. The surface of ZnO:Al is also rougher compared to that of ZnO, but not to the extent seen in the NiO:Li surface. However, for ZnO:Al and NiO:Li there are no signs of surface cracking, as can be seen in the ZnO surface. Surface cracks for ZnO have been reported in the literature. These cracks in the ZnO surface might be caused by the difference in thermal expansion coefficient between the substrate and ZnO. Grain growth can also contribute to increased surface roughness and larger microcracks [87].

From Figure 45, holes on the surface were detected for all the layers. The cause of these holes is unknown. However, the formation of these holes by PLD layering seems unlikely, as this is unseen in literature. There are multiple plausible causes for this during manufacturing, such as unclean substrates or general mishandling of the sample. If these holes were apparent before deposition of layer two or three, it might have caused the next layer to penetrate into the previous film, which again might cause current to freely pass through.

TEM imaging was employed to get a closer look at the interface between NiO:Li-ZnO:Al. Because of sub-optimal deposition, the layered structure was much thinner than expected. Nevertheless, the film could be to some degree be analyzed. Overall, the film deposition was uneven, for both layers. However, this could be because of the suboptimal PLD deposition (the PLD could not deliver high energy). At areas where the first layer of had been deposited evenly, the overlaying NiO:Li seemed to create a sharp interface with ZnO:Al, which is ideal for a p-n

junction. Using the PLD method, Ishida et al. fabricated a thin NiO:Li-ZnO junction and found it to create an atomically flat surface and interface between the layers [48].

The EDS imaging further empowers the evidence for the individual layering of the films. There is clearly shown a dense mapping of Ni in-between the Zn-based layers. Unfortunately, neither the Al donor dopants nor Li acceptor dopant mapping can indicate if they are present in the sample, because of the Al sample holder creating a mapping of Al all over, and because Li is such a light element, making it hard to detect. The EDS images show Zn and Ni with high densities in their respective layers, however, they also show small densities of Zn and Ni throughout the cross-section, which might indicate interdiffusion between the layers. However, Desissa et al. have investigated the diffusion of ZnO:Al and NiO:Li [41]. Figure 20 in section 3.3 shows an interdiffusion profile for $Ni^{2+}$ and $Zn^{2+}$ in the NiO-ZnO system. It was calculated that the diffusion length for $Ni^{2+}$ into ZnO:Al and $Zn^{2+}$ into NiO:Li over a 5 year period at a temperature of 900 ℃, is 200 μm and 20 μm, respectively. This indicates that interdiffusion can occur, but it is unlikely that Ni and Zn have interdiffused in the sample to the extent given by the EDS mapping, given the elapsed time and low temperature of the deposition process. In addition, the reliability of the EDS at this magnification is not optimal, especially when looking at the thin intermediate layer of NiO:Li. Desissa et al. also found that that $Ni^{2+}$ diffused into ZnO by bulk and enhanced grain diffusion, whereas $Zn^{2+}$ diffused into NiO by bulk diffusion. The crystallite size is quite small for ZnO and ZnO:Al in the BJT sample, hence increasing the number of grain boundaries in the structure, might, with Desissas results in mind, cause an increase in the diffusion of $Ni^{2+}$ into the ZnO layers. Therefore, an increase in crystallite sizes to reduce the grain boundary diffusion might terminate diffusion by some degree [41].

The characterization of the BJT indicates there is deposited high-quality films with good interfaces, hence suggesting that employing the PLD method to deposit films of these oxides is an appropriate approach. The PLD method is used to deposit these films with varying results throughout literature. One challenge is the layering of NiO, as it seems to often be deposited with a rather low degree of crystallinity [55, 76]. However, even though this is often described as a problem, studies have found that the increase in crystallinity of NiO will decrease the conductivity [69, 70]. Oka et al. discussed in the possibility that the increased grain boundaries of a degraded film would increase the conductivity. However, upon further investigation, they dismissed this theory as there was an absence of grain boundaries. Knowing this, they contributed this increase in conductivity to the electrical conduction of NiO thin films strongly correlates with tailing the band edge via the degradation of the entire film crystallinity rather than the grain boundaries[69]. As the PLD possesses the ability to deposit materials at low temperatures, this suits the deposition of NiO well. Karsthof et al. fabricated a functioning junction-field effect transistor of a NiO-ZnO heterojunction using the PLD method. They deposited films with a gate thickness of 50 nm, hence confirming the PLD method to be a good fabrication method, also at atomic ranges. Also here, the NiO was not found to be crystalline, rather amorphous. However, they contributed to this low structural quality to be the cause of low channel mobility in the thinnest film of 10 nm [58]. It is of high importance to find the

appropriate parameters to achieve the desired material properties of the deposited material. However, as some aspects of the film is improved by a specific setting, others might deteriorate, e.g. the desire of a smooth surface for the NiO:Li layer can be improved by the increase in substrate temperature during deposition [70], however, we have already established that the increase in substrate temperature will also increase film resistivity for NiO:Li. Hence, some aspects of the PLD might be hard to overcome.

**Electrical measurements**

Resistivity measurements on the fabricated films of ZnO, ZnO:Al and NiO:Li show behavior in contrast to what is found by other studies and in contrast to what is expected from the theory. If one is to interpret the resistivity of these films in relation to temperature, one could say they are behaving as if they are on the borderline between metallic and semiconducting. However, the resistivity itself implies they have, at room temperature, a conductivity of $3.5x10^4$ $(\Omega m)^{-1}$, $3.3x10^5$ $(\Omega m)^{-1}$, and $1.4x10^4$ $(\Omega m)^{-1}$ for ZnO, ZnO:Al and NiO:Li, respectively, which puts them in the semiconducting region. hence showing that the resistivity curves presented in section 5.2.1, strongly deviate from what is expected in theory, and what is found in the literature. If one looks at figure 18, with NiO containing a resistivity similar to that of the findings in this study, one can see that the resistivity gets reduced gradually, which is supported by theory. This then puts the results in a state un unreliability. The strange behavior might be caused by flaws made in the initial setup of the van der Pauw 4-point measurement procedure.

Electrical measurements on the constructed BJT did not succeed in finding the characteristic transistor behavior. The measured I-V characteristics of the BJT sample, presented in Figure 52, shows characteristics far from the intended output of a functioning transistor, or in resemblance to the few studied transistors made from the NiO-ZnO system, mentioned in section 3.5 [58, 59]. However, the initial continuity of the different $I_B$ currents, seen in figure 52, showed behavior to be noticed and further investigated. As the NiO:Li-ZnO:Al junction showed an Ohmic behavior, it is expected that the BJT would not be functional. However, there was constructed a successful NiO:Li-ZnO junction, showing rectifying behavior, with some resemblance to what is found in other studies on the NiO-ZnO p-n junction [37, 55, 82, 83].

Multiple factors can have caused the Ohmic behavior in the BE junction. As the junction shows Ohmic behavior, one can presume that there is no depletion zone fabricated, as current freely cross the junction, or that the zone is very narrow because of high doping. From equation 32, it is evident that the increase in doping concentration will cause a decrease in depletion width. If the depletion width is too small, tunneling across the potential step can cause the Ohmic behavior. One might also speculate in the formation of an interfacial layer, composed of a composite of the ZnO and NiO, creating a p-c-n junction. Desissa et al. found that by introducing a composite layer of 50/50 mole % $Ni_{0.98}Li_{0.02}O$ and $Zn_{0.98}Al_{0.02}O$ at the interface between $Ni_{0.98}Li_{0.02}O$ and $Zn_{0.98}Al_{0.02}O$, the interface resistance of the p-c-n junction was only 14% of the p-n junction. Both the p-c-n and p-n samples showed rectifying behavior, but at a

given voltage the current through the p-c-n junction was much higher compared to the p-n junction. A possible cause of this increased ohmic behavior was attributed to the numerous local p-n junctions of the composite, which will contribute to the increase of the overall large interface area, increasing the area-specific series resistance[88]. Figure 23 (B) show a comparison between the p-n and p-c-n sample, showing the p-c-n sample having a curve moving towards ohmic behavior compared to the p-n sample. As this was possibly contributed to the increased ohmic behavior, one might argue that the rough surface of the deposited NiO:Li sample, shown in figure 43 (B), will effectively contribute to an increased interface are, or act in resemblance of the composite. However, the interfaces shown in the TEM and in the SEM don't have indications of interface defects such as pores.

In the rectifying I-V curve of the NiO:Li-ZnO junction, one can see that the reverse bias has a breakdown voltage value lesser than the value of the forward bias threshold voltage, which is not common diode behavior. In Figure 9, and from eq. 32, one can see that the built-in potential increases with a reverse bias applied, hence reducing the possibility of current flow. However, Zener diodes have low threshold voltage, and current can flow both ways with sufficiently applied bias. These diodes are heavily doped, and this is the reason for their unique characteristics. Shown from eq. 32, an increase in doping concentration effectively reduces the depletion width. The increase will also cause the depletion region to have a large number of immobile ions, creating a strong built-in electric field. When a reverse bias is applied, an electric field is added in addition to the built-in electric field, hence creating a strong electric field within the depletion region. When a sufficient amount of bias is applied, the electric field will have enough energy to knock-off electrons and holes bounded via covalent bonds, hence generating a large number of charge carriers. And because of the narrow depletion width, the charge carriers can tunnel through it. The tunneling process allows electrons in the valence band to tunnel into the conduction band and vice versa. Electrons tunneling through the diode do not have to go over the barrier and as a result, the diode reverse current can increase dramatically. This is known as Zener breakdown. In literature, no Zener diodes based on the NiO-ZnO system is found. However, recently, successful fabrication of Zener diodes with ZnO has been made [89, 90].

Obviously, the fabrication of a functioning NiO-ZnO based transistor is possible, as it has been shown in studies [karsthof ][ishida]. And the plenty of articles on the NiO-ZnO based diodes, also indicate this. The electrical properties of the materials and junctions vary widely throughout these studies, as one would expect from the many fabrication processes being used. This also makes the system applicable for many uses within different types of electronics, e.g. the possibility proposed by Kaur et al., that the magnetic properties of the NiO could be utilized for future spintronic devices. However, some disadvantages have also been raised. The junction field-effect transistor made by Karsthoff et al. showed that temperature impacts the performance of the transistor [58]. This is however not surprising, given the earlier discussions on the temperature effect on the electrical performance of semiconductors. However, the irreversible effect on electric behavior is less ideal for electrical

devices, and as the transistor was deposited at much higher temperatures, one would expect the transistor to handle these temperature changes from 10 ℃ to 100 ℃.

**Outlook**

Fabrication of a functioning transistor did not succeed. However, one of the junctions in the transistor had success in achieving diode behavior, showing interesting Zener diode behavior. Transistors based on the NiO-ZnO system should be further investigated, as their potential within electronic devices is not yet fully known. As one suggested reason for the ohmic behavior of the NiO:Li-ZnO:Al diode was the possibility of an increased interface surface area, one should optimize the fabrication method to decrease the surface roughness of the NiO:Li before depositing a second layer. Also, one should investigate the doping effect on the depletion region for the system, as this strongly affects the junction behavior. Further, the effect of temperature creating irreversible changes to the electrical properties should be further investigated. This should be done in cycles and over longer time periods, in order to have an idea as to if these devices can be applied for such circumstances.

# 7 Conclusion

The fabrication of a three-layered structure using the PLD method has been successful. The growth of the layers seems to be dense and of good quality, with NiO:Li layer showing lesser crystalline growth compared to that of the ZnO layers, which is also a common occurrence in other studies. The interfaces appear sharp and without any notable interface defects. This shows the PLD method to be a good fabrication method for these materials. And for further optimization, fine-tuning of the parameters used in the PLD is advised.

The fabrication, however, did not succeed in creating a functioning BJT. It was found that the NiO:Li-ZnO:Al junction showed ohmic behavior, explaining the non-functioning BJT. It was proposed that an interface composite layer, or the rough surface of NiO:Li, might have caused the ohmic behavior of this junction, because of an increased interface area effectively reducing the junction resistance. However, nor the occurrence of an interface composite or defects is detected along with the interfaces, hence diminishing this theory. There was a successful fabrication of the NiO:Li-ZnO p-n junction, however. This junction showed Zener diode like behavior, which is not found for the NiO-ZnO system elsewhere. Also here, a shallow depletion region is a probable cause for this behavior, as tunneling can occur because of the narrow depletion region.

The materials used in this project are highly affected by the fabrication route. NiO desires a less crystalline structure for optimal conductivity, and this is achieved with relatively low-temperature deposition. However, this creates the issue with the high-temperature operation, as this might further crystallize the material, hence decrease the conductivity. And is in opposition to the ZnO higher temperature deposition for high conductivity. Therefore, In order to fabricate an optimal device, the perfect in-between needs to be found for the fabrication process.

These materials have enormous potential in the future development of electronic devices. This project might not have fabricated a functioning BJT, however, this might lie in the fact that the fabrication route has not been optimal for the sensor device of a transistor, as the lab is probably contaminated to some degree, and the relatively rough handling of the device for measurements and characterization, compared to clean labs making optimal transistors. This, however, should not undermine the possibilities of these materials creating new possibilities within e.g. transparent electronics. As they do show applicability in the fabrication process and with an outcome of, at least one, functioning diode. The further investigation in the NiO-ZnO heterojunctions should ensue, and as progress is made within fabrication and understanding, maybe they will become highly applicable for future transistors, or Zener diodes.

# Bibliography


1. Stojcev, M., *The limits of semiconductor technology and oncoming challenges in computer microarchitectures and architectures.* 2005.
2. Wang, J., et al., *Synthesis and characterization of multipod, flower-like, and shuttle-like ZnO frameworks in ionic liquids.* Materials letters, 2005. **59**(11): p. 1405-1408.
3. Wang, Z.L., *Splendid One-Dimensional Nanostructures of Zinc Oxide: A New Nanomaterial Family for Nanotechnology.* ACS Nano, 2008. **2**(10): p. 1987-1992.
4. Bacaksiz, E., et al., *The effects of zinc nitrate, zinc acetate and zinc chloride precursors on investigation of structural and optical properties of ZnO thin films.* Journal of alloys and compounds, 2008. **466**(1-2): p. 447-450.
5. Shim, E.S., et al., *Effect of the variation of film thickness on the structural and optical properties of ZnO thin films deposited on sapphire substrate using PLD.* Applied Surface Science, 2002. **186**(1): p. 474-476.
6. Lee, J.-H., K.-H. Ko, and B.-O. Park, *Electrical and optical properties of ZnO transparent conducting films by the sol–gel method.* Journal of crystal growth, 2003. **247**(1-2): p. 119-125.
7. Babeer, A.M., *Optical and Structural Characteristics of Nanocrystalline ZnO:Cd Ceramics.* SILICON, 2017. **9**(6): p. 847-853.
8. Wang, Z.L., *Piezoelectric Nanogenerators Based on Zinc Oxide Nanowire Arrays.* Science, 2006. **312**(5771): p. 242-246.
9. Subramaniam, V.D., et al., *Health hazards of nanoparticles: understanding the toxicity mechanism of nanosized ZnO in cosmetic products.* Drug Chem Toxicol, 2018. **42**(1): p. 84-93.
10. Bhattacharyya, S. and A. Gedanken, *A template-free, sonochemical route to porous ZnO nano-disks.* Microporous and Mesoporous Materials, 2008. **110**(2): p. 553-559.
11. Özgür, Ü., et al., *A comprehensive review of ZnO materials and devices.* Journal of applied physics, 2005. **98**(4): p. 041301-041301-103.
12. Wang, Z.L., *Zinc oxide nanostructures: growth, properties and applications.* Journal of physics. Condensed matter, 2004. **16**(25): p. R829-R858.
13. Janotti, A. and C.G. Van de Walle, *Fundamentals of zinc oxide as a semiconductor.* Reports on progress in physics, 2009. **72**(12): p. 126501.
14. Reynolds, D.C., et al., *High-quality, melt-grown ZnO single crystals.* Journal of applied physics, 2004. **95**(9): p. 4802-4805.
15. Bjørheim, T.S. and E. Kotomin, *Ab Initio Thermodynamics of Oxygen Vacancies and Zinc Interstitials in ZnO.* J. Phys. Chem. Lett, 2014. **5**(24): p. 4238-4242.
16. Oba, F., et al., *Point defects in ZnO: an approach from first principles.* Sci Technol Adv Mater, 2016. **12**(3): p. 034302.
17. Cox, S.F.J., et al., *Experimental Confirmation of the Predicted Shallow Donor Hydrogen State in Zinc Oxide.* Phys Rev Lett, 2001. **86**(12): p. 2601-2604.
18. Van de Walle, C.G., *Hydrogen as a Cause of Doping in Zinc Oxide.* Phys Rev Lett, 2000. **85**(5): p. 1012-1015.
19. Zhai, C.-H., et al., *Effects of Al Doping on the Properties of ZnO Thin Films Deposited by Atomic Layer Deposition.* Nanoscale Res Lett, 2016. **11**(1): p. 1-8.
20. Ajili, M., et al., *Effect of Al-doped on physical properties of ZnO Thin films grown by spray pyrolysis on SnO2: F/glass.* EPJ Web of conferences, 2012. **29**: p. 2.
21. Tsubota, T., et al., *Thermoelectric properties of Al-doped ZnO as a promising oxide material for high-temperature thermoelectric conversion.* Journal of materials chemistry, 1997. **7**(1): p. 85-90.
22. Yang, H., et al., *Solid-state synthesis and electrochemical property of SnO 2/NiO nanomaterials.* Journal of Alloys and Compounds, 2008. **459**(1): p. 98-102.
23. Jiang, D.Y., et al., *Optical properties of NiO thin films fabricated by electron beam evaporation.* Vacuum, 2012. **86**(8): p. 1083-1086.

24. Tadic, M., et al., *Magnetic properties of NiO (nickel oxide) nanoparticles: Blocking temperature and Neel temperature.* Journal of alloys and compounds, 2015. **647**: p. 1061-1068.
25. Patel, M., et al., *Excitonic metal oxide heterojunction (NiO/ZnO) solar cells for all-transparent module integration.* Solar energy materials and solar cells, 2017. **170**: p. 246-253.
26. Azens, A. and C. Granqvist, *Electrochromic smart windows: energy efficiency and device aspects.* Journal of solid state electrochemistry, 2003. **7**(2): p. 64-68.
27. Zhang, et al., *P-type transparent conducting oxides.* PubMed.gov, 2016.
28. Srinivasan, G. and M.S. Seehra, *Magnetic susceptibilities, their temperature variation, and exchange constants of NiO.* Physical review. B, Condensed matter, 1984. **29**(11): p. 6295-6298.
29. Fiévet, F., et al., *Lattice parameter, microstrains and non-stoichiometry in NiO. Comparison between mosaic microcrystals and quasi-perfect single microcrystals.* Journal of Applied Crystallography, 1979. **12**(4): p. 387-394.
30. Balagurov, A.M., et al., *Neutron scattering study of structural and magnetic size effects in NiO.* IOP conference series. Materials Science and Engineering, 2013. **49**: p. 12021.
31. Adler, D. and J. Feinleib, *Electrical and Optical Properties of Narrow-Band Materials.* Physical review. B, Solid state, 1970. **2**(8): p. 3112-3134.
32. Stokłosa, A., *Point defect diagrams for pure and doped nickel oxide $$ {\hbox{N}}{{\hbox{i}}_{{1} - \delta }}{\hbox{O}} $$ in the temperature range of 1,173–1,673 K (II).* Ionics, 2011. **17**(3): p. 271-285.
33. Park, C., et al., *Electronic, Optical and Electrical Properties of Nickel Oxide Thin Films Grown by RF Magnetron Sputtering.* Applied Science and Convergence Technology, 2015. **24**(3): p. 72-76.
34. Eror, N.G. and J.B. Wagner, *Electrical Conductivity of Single Crystalline Nickel Oxide.* physica status solidi (b), 1969. **35**(2): p. 641-651.
35. J, A. and T. Sahoo, *Effect of Li doping on conductivity and band gap of nickel oxide thin film deposited by spin coating technique.* Materials Research Express, 2019. **7**(1): p. 016405.
36. Jang, W.-L., et al., *Electrical properties of Li-doped NiO films.* Journal of the European Ceramic Society, 2010. **30**(2): p. 503-508.
37. Dutta, T., et al., *Effect of Li doping in NiO thin films on its transparent and conducting properties and its application in heteroepitaxial p-n junctions.* Journal of applied physics, 2010. **108**(8): p. 083715-083715-7.
38. Rubio-Marcos, F., et al., *Mechanism of Ni1–x Zn x O Formation by Thermal Treatments on NiO Nanoparticles Dispersed over ZnO.* J. Phys. Chem. C, 2011. **115**(28): p. 13577-13583.
39. Kurokawa, H., et al., *Stability and electrical properties of high temperature p-n junction of NiO-ZnO system.* Electrochemical Society Inc, 2001.
40. Bates, C.H., W.B. White, and R. Roy, *The solubility of transition metal oxides in zinc oxide and the reflectance spectra of Mn 2+ and Fe 2+ in tetrahedral fields.* Journal of Inorganic and Nuclear Chemistry, 1966. **28**(2): p. 397-405.
41. Desissa, T.D., et al., *Inter-diffusion across a direct p-n heterojunction of Li-doped NiO and Al-doped ZnO.* Solid state ionics, 2018. **320**: p. 215-220.
42. Ma, M.J., et al., *Orientation dependent band alignment for p-NiO/n-ZnO heterojunctions.* Journal of applied physics, 2013. **113**(16): p. 163704.
43. Yang, Z.-G., et al., *Valence-band offset of p-NiO/n-ZnO heterojunction measured by X-ray photoelectron spectroscopy.* Physics Letters A, 2011. **375**(16): p. 1760-1763.
44. Echresh, A., et al., *UV photo-detector based on p-NiO thin film/n-ZnO nanorods heterojunction prepared by a simple process.* Journal of alloys and compounds, 2015. **632**: p. 165-171.
45. Kawade, D., S.F. Chichibu, and M. Sugiyama, *Experimental determination of band offsets of NiO-based thin film heterojunctions.* Journal of applied physics, 2014. **116**(16): p. 163108.

46. Deng, R., et al., *X-ray photoelectron spectroscopy measurement of n-ZnO/p-NiO heterostructure valence-band offset.* Applied physics letters, 2009. **94**(2): p. 022108-022108-3.
47. Sultan, M., et al., *Band alignment and optical response of facile grown NiO/ZnO nano-heterojunctions.* Superlattices and Microstructures, 2017. **112**: p. 210-217.
48. Ishida, Y., et al., *Potential profiling of the nanometer-scale charge-depletion layer in n-ZnO/p-NiO junction using photoemission spectroscopy.* Applied physics letters, 2006. **89**(15): p. 153502.
49. Dey, S., et al., *Voltage-controlled NiO/ZnO p–n heterojunction diode: a new approach towards selective VOC sensing.* Microsystems & nanoengineering, 2020. **6**(1): p. 1-9.
50. Moormann, H., D. Kohl, and G. Heiland, *Work function and band bending on clean cleaved zinc oxide surfaces.* Surface Science, 1979. **80**: p. 261-264.
51. Kwon, U., et al., *Solution-Processible Crystalline NiO Nanoparticles for High-Performance Planar Perovskite Photovoltaic Cells.* Sci Rep, 2016. **6**(1): p. 30759.
52. Hasan, M.R., et al., *Self-powered p-NiO/n-ZnO heterojunction ultraviolet photodetectors fabricated on plastic substrates.* APL Mater, 2015. **3**(10): p. 106101-106101-7.
53. Husain, A.A.F., et al., *A review of transparent solar photovoltaic technologies.* Renewable & sustainable energy reviews, 2018. **94**: p. 779-791.
54. Sta, I., et al., *Fabrication and characterization of NiO/ZnO p-n junctions by sol-gel spin coating technique*. 2012, IEEE. p. 113-115.
55. Gupta, R.K., K. Ghosh, and P.K. Kahol, *Fabrication and characterization of NiO/ZnO p–n junctions by pulsed laser deposition.* Physica E: Low-dimensional Systems and Nanostructures, 2009. **41**(4): p. 617-620.
56. Ohta, H., et al., *UV-detector based on pn-heterojunction diode composed of transparent oxide semiconductors, p-NiO/n-ZnO.* Thin Solid Films, 2003. **445**(2): p. 317-321.
57. Grundmann, M., R. Karsthof, and H. von Wenckstern, *Interface Recombination Current in Type II Heterostructure Bipolar Diodes.* ACS Appl. Mater. Interfaces, 2014. **6**(17): p. 14785-14789.
58. Karsthof, R., H. von Wenckstern, and M. Grundmann, *Transparent JFETs Based on p -NiO/ n -ZnO Heterojunctions.* IEEE Transactions on Electron Devices, 2015. **62**(12): p. 3999-4003.
59. Kaur, H., et al., *Magnetic bipolar transistor based on ZnO/NiO/Si heterostructure using pulsed laser deposition.* AIP advances, 2020. **10**(1): p. 015119-015119-5.
60. Ashfold, M.N.R., et al., *Pulsed laser ablation and deposition of thin films.* Chem Soc Rev, 2004. **33**(1): p. 23.
61. Broduceanu, D., et al., *Pulsed laser deposition of oxide thin films.* 2004.
62. Sankur, H. and J.T. Cheung, *Highly oriented ZnO films grown by laser evaporation.* Journal of Vacuum Science & Technology A: Vacuum, Surfaces, and Films, 1983. **1**(4): p. 1806-1809.
63. Ghosh, P. and A.K. Sharma, *Growth and optical characterization of diamond-shaped zinc oxide nanostructures deposited by pulsed laser ablation.* Applied physics. A, Materials science & processing, 2013. **115**(1): p. 235-244.
64. Craciun, V., et al., *Characteristics of high quality ZnO thin films deposited by pulsed laser deposition.* Applied physics letters, 1994. **65**(23): p. 2963-2965.
65. Scott, R.C., et al., *Highly conductive ZnO grown by pulsed laser deposition in pure Ar.* Applied Physics Letters, 2010. **97**(7): p. 072113-072113-3.
66. Venkatachalam, S., Y. Iida, and Y. Kanno, *Preparation and characterization of Al doped ZnO thin films by PLD.* Superlattices and Microstructures, 2008. **44**(1): p. 127-135.
67. Park, S.-M., T. Ikegami, and K. Ebihara, *Investigation of Transparent Conductive Oxide Al-Doped ZnO Films Produced by Pulsed Laser Deposition.* Japanese Journal of Applied Physics, 2005. **44**(11): p. 8027-8031.
68. Gurpreet Kaur Anirban Mitra, K.L.Y., *Pulsed laser deposited Al-doped ZnO thin films for optical applications.* 自然科学进展-国际材料(英文版), 2015. **25**(1): p. 12-21.

69. Oka, K., et al., *Growth atmosphere dependence of transport properties of NiO epitaxial thin films.* Journal of Applied Physics, 2008. **104**(1): p. 013711-013711-4.
70. Fasaki, I., et al., *Structural, electrical and mechanical properties of NiO thin films grown by pulsed laser deposition.* Applied surface science, 2010. **257**(2): p. 429-433.
71. Kakehi, Y., et al., *Influence of initial layers on crystallinity of NiO(1 1 1) epitaxial film grown at room temperature by pulsed laser deposition.* Sensors and Materials, 2002. **14**: p. 281-291.
72. Huang, Y., et al., *Transparent conductive p-type lithium-doped nickel oxide thin films deposited by pulsed plasma deposition.* Applied Surface Science, 2012. **258**(19): p. 7435-7439.
73. Prasad, S.V., S.D. Walck, and J.S. Zabinski, *Microstructural evolution in lubricious ZnO films grown by pulsed laser deposition.* Thin Solid Films, 2000. **360**(1): p. 107-117.
74. Shan, F.K., et al., *Substrate effects of ZnO thin films prepared by PLD technique.* Journal of the European Ceramic Society, 2004. **24**(6): p. 1015-1018.
75. Taabouche, A., et al., *Preparation and characterization of Al-doped ZnO piezoelectric thin films grown by pulsed laser deposition.* Ceramics international, 2016. **42**(6): p. 6701-6706.
76. Sandana, V., et al., *Structural, optical, electrical and morphological study of transparent p-NiO/n-ZnO heterojunctions grown by PLD*. SPIE OPTO. Vol. 9364. 2015: SPIE.
77. Xu, T., et al., *Processing compatibility of ZnO piezoelectric film with MEMS device*. International Symposium on Microelectronics and MEMS. Vol. 4592. 2001: SPIE.
78. Hassan, A.J., *Study of Optical and Electrical Properties of Nickel Oxide (NiO) Thin Films Deposited by Using a Spray Pyrolysis Technique.* Journal of modern physics, 2014. **5**(18): p. 2184-2191.
79. Hakim, A., J. Hossain, and K.A. Khan, *Temperature effect on the electrical properties of undoped NiO thin films.* Renewable Energy, 2009. **34**(12): p. 2625-2629.
80. Das, A.K., et al., *Studies on temperature dependent semiconductor to metal transitions in ZnO thin films sparsely doped with Al.* Journal of applied physics, 2012. **112**(10): p. 103706.
81. Roy, T.K., et al., *Temperature dependent resistivity study on zinc oxide and the role of defects.* Materials Science in Semiconductor Processing, 2013. **16**(2): p. 332-336.
82. Merih Akyuzlu, A., et al., *Electrical characterization of ZnO/NiO p-n junction prepared by the sol-gel method.* European physical journal plus, 2017. **132**(4).
83. Sato, H., et al., *Transparent conducting p-type NiO thin films prepared by magnetron sputtering.* Thin solid films, 1993. **236**(1-2): p. 27-31.
84. Xi, Y.Y., et al., *NiO/ZnO light emitting diodes by solution-based growth.* Applied physics letters, 2008. **92**(11): p. 113505.
85. Nakrela, A., et al., *Site location of Al-dopant in ZnO lattice by exploiting the structural and optical characterisation of ZnO:Al thin films.* Results in physics, 2016. **6**: p. 133-138.
86. Wang, L.-M., et al., *Characteristics of low-resistivity aluminum-doped zinc oxide films deposited at room temperature by off-axis radio-frequency sputtering on flexible plastic substrates.* Applied Physics A, 2016. **122**(8): p. 1-11.
87. Sendi, R.K. and S. Mahmud, *Effects of high-oxygen thermal annealing on structural, electrical and optical properties of undoped ZnO discs made from 40-nm ZnO nanoparticles.* Indian journal of physics, 2013. **87**(6): p. 523-531.
88. Desissa, T.D., M. Schrade, and T. Norby, *Electrical Properties of a p–n Heterojunction of Li-Doped NiO and Al-Doped ZnO for Thermoelectrics.* Journal of electronic materials, 2018. **47**(9): p. 5296-5301.
89. Jamal, R.K., et al., *Designing A Zener Diode Using Ag2O(1-X)Zno(X)/Psi Structures Deposited by Laser Induced Plasma Technique.* Iraqi journal of science, 2020: p. 1032-1039.
90. Jamal, R.K. and S.K. Mustafa, *Manufacturing Zener diode using ZnO-CuO-ZnO/PSi structures deposited laser-induced plasma technique* ReasearchGate, 2019.